MODELLING AND DESIGN OF ELECTRIC MACHINES AND ASSOCIATED COMPONENTS FOR MORE ELECTRIC VEHICLES

MODELLING AND DESIGN OF ELECTRIC MACHINES AND ASSOCIATED COMPONENTS FOR MORE ELECTRIC VEHICLES

BY

NAN ZHAO, M.Sc., B.Sc.

A Thesis Submitted to the School of Graduate Studies in Partial Fulfilment of the Requirements for the Degree of Doctor of Philosophy

McMaster University

April 2017

McMaster University DOCTOR OF PHILOSOPHY (Electrical Engineering) Hamilton, Ontario, 2017.

TITLE:	Modelling and Design of Power-train Components for Electrified Transportation
AUTHOR:	Nan Zhao B.Sc. (Taiyuan University of Technology) M.Sc. (The University of Manchester)
SUPERVISOR:	Dr. Nigel Schofield
NUMBER OF PAGES:	201

Abstract

Concerns with emissions, CO_2 in particular, and energy resource associated with conventional internal combustion engine (ICE) vehicles is motivating a shift towards more electrified power-trains for road transportation, as well as other transportation applications. The modelling, characterization and design of electrified power-trains, including energy storage technologies, traction machine technologies and their associated power electronics, are discussed in this thesis.

Port cranes are a special case of land transportation encompassing many of the power-train objectives found common with road based hybrid electric vehicles; here a port crane system is studied. The power flow for a typical crane loading cycle is analyzed and the value of the energy consumption and saving potential is calculated. Then alternative energy storage applications are considered for hybrid power-train configurations employing diesel engine generators, battery packs, supercapacitors (SCs), and flywheels. A hybrid rubber tyred gantry crane (RTGC) power-train model with power management is developed and the battery-SC hybrid energy storage systems are designed for both short- and long-period operation.

The Induction machine (IM) is a popular technology for traction applications. Although many publications discuss IM design to realize a traction torque-speed characteristic, the IM model is studied to determine the main parameters impacting on the machine performance capability at constant torque and extended speed. Based on the model analysis, an IM design procedure for traction applications is proposed which improves machine performance capability. The machine design parameters are normalized in per unit form and hence the proposed design procedure is applicable across different ratings.

In the specification and definition of vehicle power-trains, it is common (in industry) to quote data at specific operating conditions, for example, full or fixed battery terminal voltage and system temperature. The interactive influence between energy storage devices and the vehicle system is investigated. Using the all-electric Nissan Leaf power-train as a reference example, the Nissan Leaf traction system is evaluated and performance assessed by considering DC-link voltage variation from battery full state of charge (SoC) to zero

SoC and temperature variations typical of an automotive application, showing that the system stated performance is reduced as battery SoC decreases. An alternative traction machine design is proposed to satisfy the vehicle target performance requirements over the complete variation of SoC. The vehicle power-train is then modified with the inclusion of a DC/DC converter between the vehicle battery and DC-link to maintain the traction system DC-link voltage near constant. A supercapacitor system is also considered for improved system voltage management. The trade-offs between the actual Nissan Leaf power-train and the redesigned systems are discussed in terms of electronic and machine packaging, and mitigation of faulted operation at high speeds.

Using the Nissan Leaf interior permanent magnet (IPM) machine as the benchmark machine, an example surface permanent magnet (SPM) machine, with same design constraints, is designed and compared with the benchmark IPM machine. The phase voltage distortion of IPM and SPM machines are compared and the mechanisms are revealed. An alternative machine topology with pole shoe rotor is proposed for reduction of machine peak current rating and voltage distortion. The pole shoe topology is common in industrial variable speed drives employing constant torque regimes, but not for traction. Here, the machine with pole shoe rotor is designed to achieve traction performance. The pole shoe concept for vehicle traction is significantly different from existing practice in the electric and hybrid electric automotive industry and thus departure in standard design is a contribution of this thesis.

.

Acknowledgments

First and foremost, I would like to thank my supervisor, Dr. N. Schofield for his invaluable encouragement, support and guidance. Without his help, this thesis would have been even more difficult to say the least and I wish every him luck in his future life.

I would also like to thank staff and faculty members at the Department of Electrical and Computer Engineering, McMaster University for their support. I would like to thank my friends and colleagues from McMaster University, in particular Drs Rong Yang and Ran Gu for their collaboration on the Nissan Leaf machine and Lithium-ion battery modelling.

I would also like to acknowledge Dr Wangqiang Niu of Shanghai Maritime University, P R China for his support with the port crane studies and Mr Scott McCrindle of Georgian College, Ontario, Canada for road data from Nissan Leaf vehicles.

Over the course of my Ph.D. studies I have received two McMaster International Excellence Awards, and Graduate Scholarships. I would like to acknowledge McMaster University and the Natural Sciences and Engineering Research Council of Canada (NSERC) for provision of a NSERC Ph.D. Scholarship for my studies.

Finally, I would like to thank my wife and my parents in particular. Their love and support has been much appreciated.

Contents

List of Figures

List of Tables

Declaration of Academic Achievement

No portion of the work referred to in this thesis has been submitted in support of an application for another degree or qualification of this or any other place of learning.

Chapter 1

Introduction

1.1 EV Development Status

The development of industrialized economies is closely linked to energy consumption. Hence, the rapid growth of the global economy raises concerns about energy security and climate change. In 2014, the total greenhouse gas (GHG) emissions in Canada contained 732 Mega-tonnes (Mt) of carbon dioxide (CO_2) equivalent emissions. The transportation sector in Canada is a significant emitter of GHGs, accounting for 171 Mt CO_2 equivalent (23% of total emissions) [1]. The GHG emissions by the transportation sector in Canada between 1990 and 2014 are illustrated in Fig. 1.1, which shows a 32% (42 Mt CO_2 equivalent) increase over this 25 year period. From a global perspective, transportation contributes to nearly one-fifth of global energy use and one quarter of energy-related carbon dioxide emissions [2]. Further, with the rapid rise in personal vehicle ownership, the number of passenger cars is expected to increase by a factor of three from 2010 to 2050 given current market trends [3].

Electric vehicles (EVs) are a technology that has the potential to make a significant contribution to increase energy security, reduced carbon dioxide emissions and improved air quality in the foreseeable future [4, 5]. In recent years, the world has witnessed spectacular EV development, as discussed in a report presented by the International Energy Agency and Electric Vehicles Initiative of Clean Energy Ministerial [6], which provides an update on recent EV developments. In 2015, the total stock of hybrid electric vehicle (HEV) and battery electric vehicle (BEV) reached 1.26 million, 100 times more than in

2010, as illustrated in Fig. 1.2. BEVs, contributing zero emission, shared 59 % of the total EV stock. To achieve larger electric range of commercially available EVs, the estimated battery energy density has increased from 60 Wh/L in 2008 to 295 Wh/L in 2015, improving by almost 400% (US DOE, 2016) [6]. On the other hand, estimated battery cost has fallen from about 1000 $US/kWh in 2008 to 268 $US/kWh in 2015, which represents a 73% reduction in seven years (US DOE, 2016) [6]. Substantial new implementation of electric vehicle supply equipment was also observed in the past few years, on par with the growth of the global electric car stock. For example, the growth of slow and fast charger stock from 2010 to 2015 is illustrated in Fig. 1.3. It can be noticed that, for almost every year, there has been a doubling in the number of reported slow and fast charging infrastructures.

As society moves from conventional internal combustion engine (ICE) propulsion system towards more electric technologies for on-road transportation, the application of electrified power-trains is also expanding in the of naval, port, railroad, and aerospace transportation sectors. Underpinning the move to more electric systems is a need to design electrified power-trains and components that can meet the transportation application requirements. This design process needs to inter-link the performance characteristics of a number of different components, each of which interacts with the other, while also accounting for external ambient variations. The thesis investigates these component interactions by way of a number of case study examples and detailed component design.

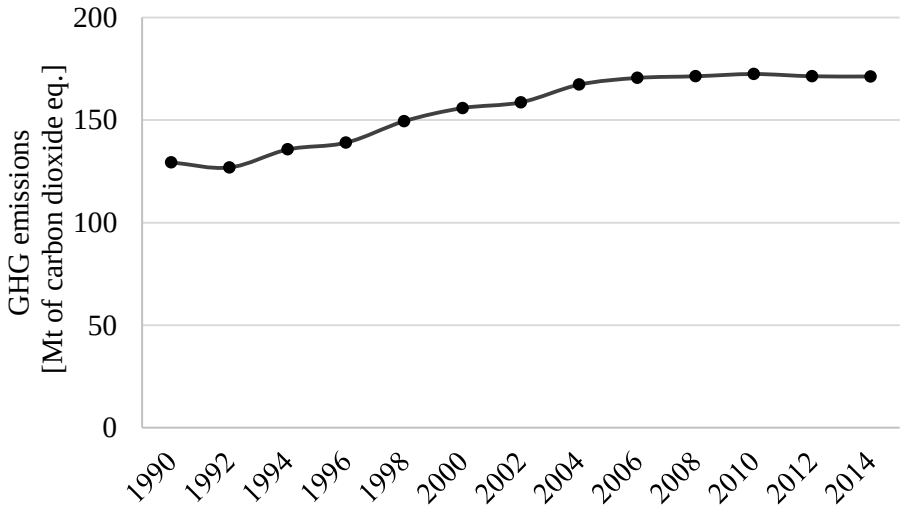

Fig. 1.1. GHG emissions by transportation sector in Canada [1].

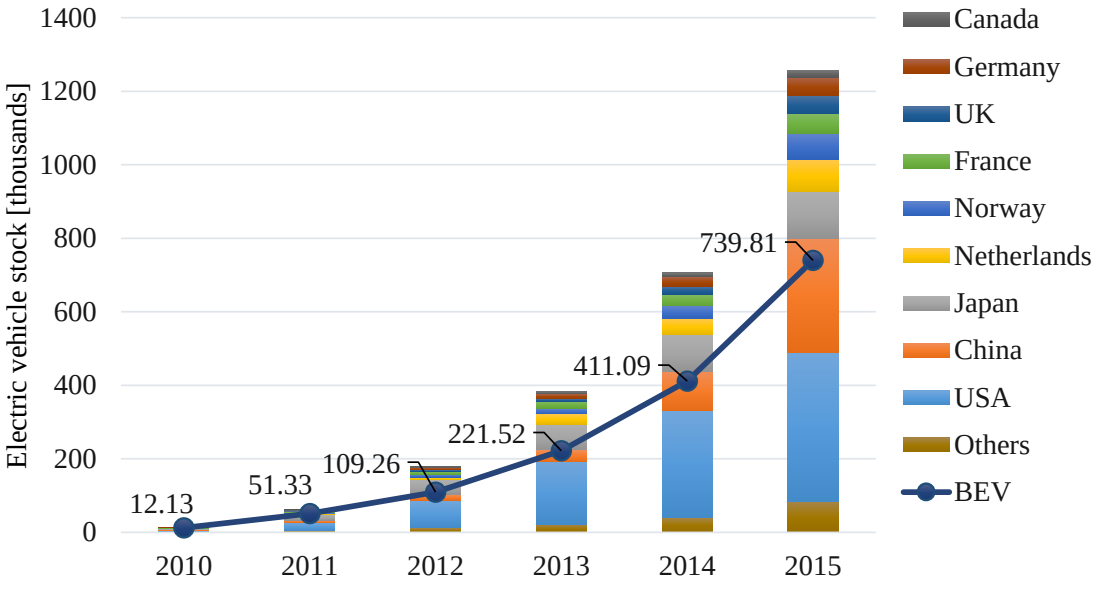

Fig. 1.2. Evolution of the global electrified vehicle stock [6].

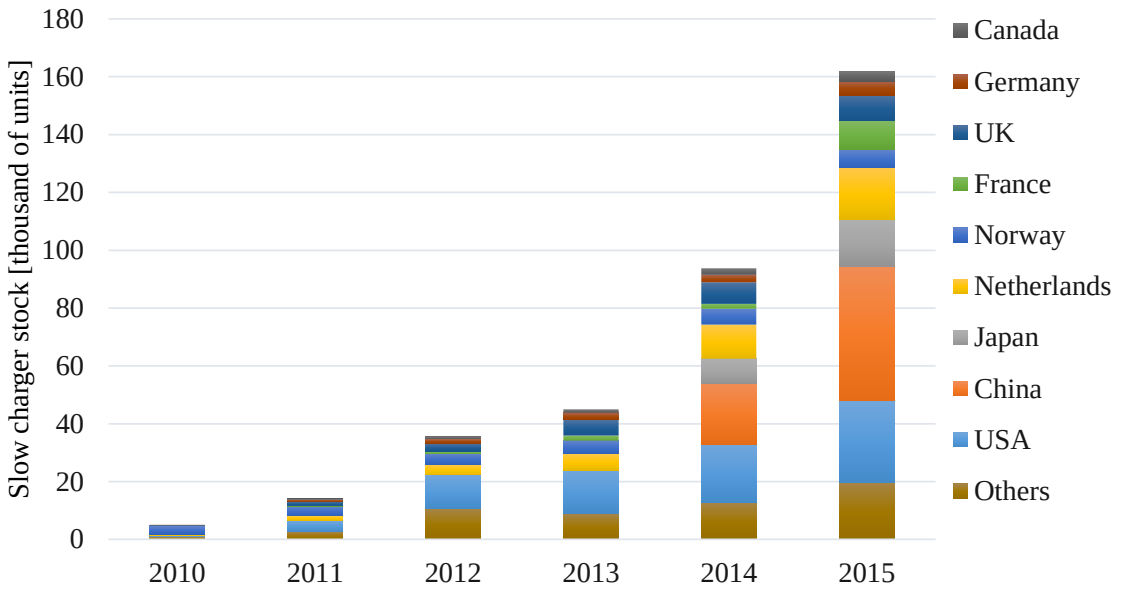

(a) Slow charger stock

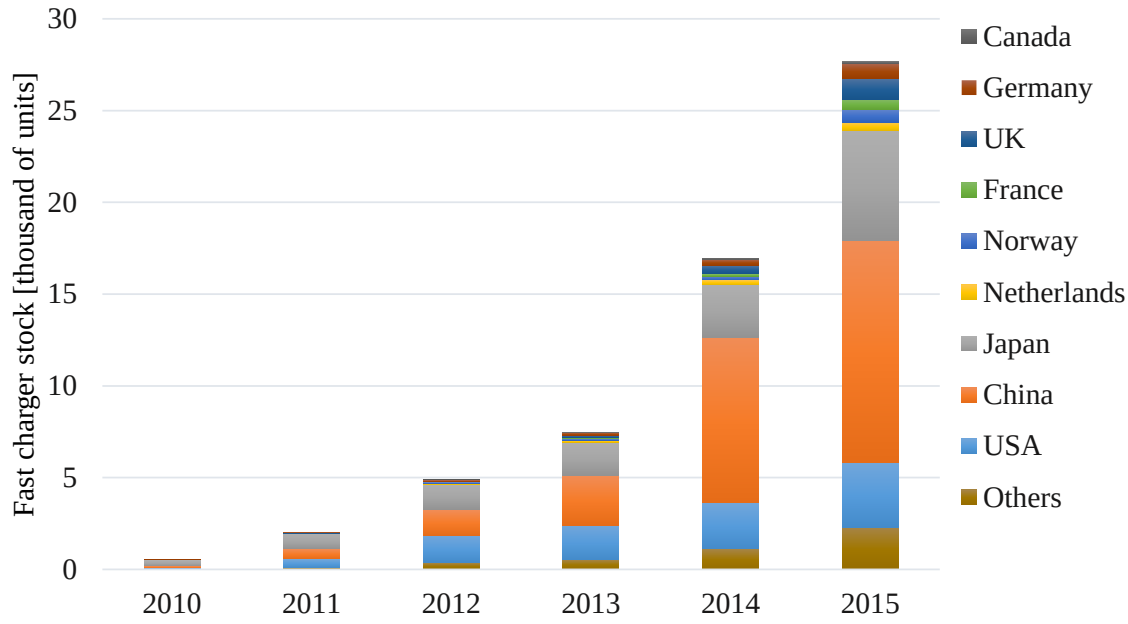

(b) Fast charger stock

Fig. 1.3. Publicly accessible slow and fast charger stock [6].

1.2 Electrified power-train

Conceptual layouts of electric vehicle (EV) and hybrid electric vehicle (HEV) power-train systems, with the options of different energy sources and their associated interconnection, is shown in Fig. 1.4 [7]. Generally, the EV energy sources are divided into primary energy source options and peak power buffer options. The energy management philosophy is that the primary energy sources always have high energy density, such as ICE-generator, electro-chemical battery and fuel cells. On the other hand, peak power buffer options, such as supercapacitors, flywheels and sometime batteries, are always required to have high power density. As will be discussed in later chapters, there is always a wide disparity between vehicle average and peak power requirements for urban driving. Hence, the peak power buffer could be used to supply peak power and constrain the voltage variation of the DC link. In order to control the power flow, it is necessary to install a power electronic converter in series with the energy sources or the peak power buffers or both.

HEVs employ both ICE and electric machines in the powertrains. The way these two energy converters are combined to propel the vehicle determines the three basic powertrain architectures:

(i) series hybrid,

(ii) parallel hybrid and

(iii) series-parallel hybrid [7].

For example, if the ICE-generator and battery are selected and combined for the energy source, the configuration in Fig. 1.4 (a) will become a typical series HEV power-train. In series HEVs the vehicle wheels are only driven by the electric machine which also operates as generator during breaking. With the implementation of power electronic converters, the ICE-generator is ideally always being operated at minimum fuel consumption (or maximum efficiency) and emissions and is used to charge the battery and supply energy to the electric machine. Fig. 1.4 (b) shows a simple parallel hybrid power-train layout.

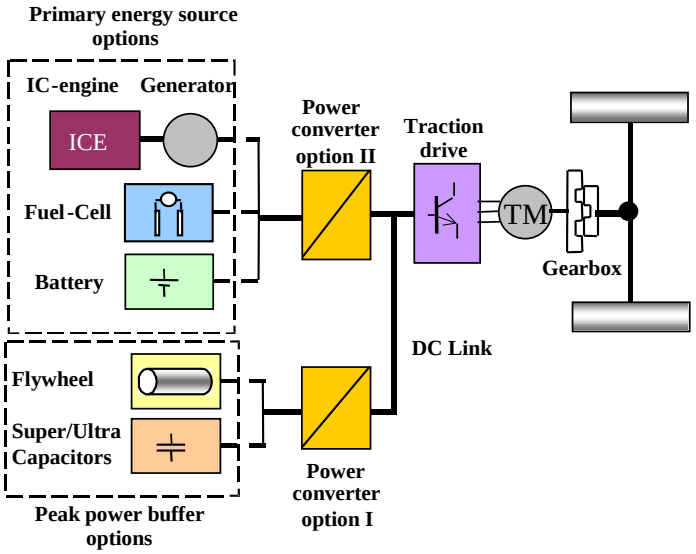

(a) Series power-train options.

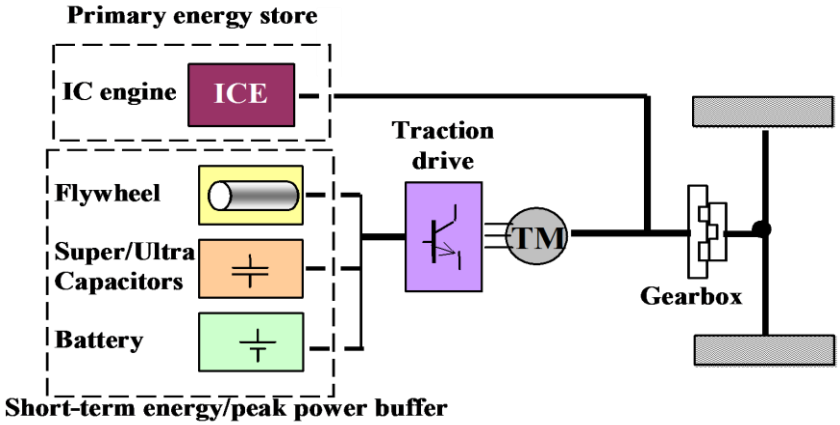

(b) Parallel HEV power-train options.

Fig. 1.4. General layout of vehicle power-train.

For pure battery electric vehicles, electro-chemical batteries can be used as the only energy source or chosen as the main energy source in a hybrid energy source system, where supercapacitors (SCs), for example, operate as a peak power buffers. Fig. 1.5 illustrates an example all electric power-train system. In order to control power flow, a DC/DC converter is installed in series with the SCs. Further, to achieve a controllable DC-link voltage, another DC/DC converter can be installed between the battery and machine drive, as will be explored further in Chapter 5.

As a special vehicle, a port crane for moving containers is also studied in this thesis. So far, in the yard of the port terminal, the cranes are still supplied by diesel ICE generators. This thesis investigates the potential of electrified power-trains for port crane operation. The port crane may have a similar power-train configuration to EV and HEV power-trains. The loading cycles of a typical system are studied and the energy storage systems and electric machines designed to meet the power and energy requirements.

Electrified power-trains have shown their competitiveness in transportation applications. However, there is a need to design the power-train system that can meet the power and energy requirements of the transportation applications. So far, the all-electric power-trains are mainly studies based on EV applications, but there is no academic research work reported on all electric power/energy systems for port cranes. Similarly, detailed design encompassing system losses, thermal management, component mass, volume, and system dynamic operation have not been reported previously. Induction machines are always employed for port cranes and the torque-speed operating points of the lift machine fits in with the traction torque-speed characteristic. Although induction machine is a mature technology, existing studies on traction induction machine design rely on optimization algorithms or iterative calculation programs. The key parameters influencing design for traction torque-speed characteristic are not identified. For EV power-trains, the energy storage system and traction machine are separately designed and the interactive influence between them is rarely considered. Further, interior permanent magnet machines are widely used as EV traction machines and hence most of the existing literature and industry deem that machines must be salient if they have to achieve high torque density and sufficient

field-weakening capability as the traction torque-speed characteristic requires. However, the reason is not well explained. The IPM machine field-weakening capability, in terms voltage distortion and ripple are rarely considered and explained.

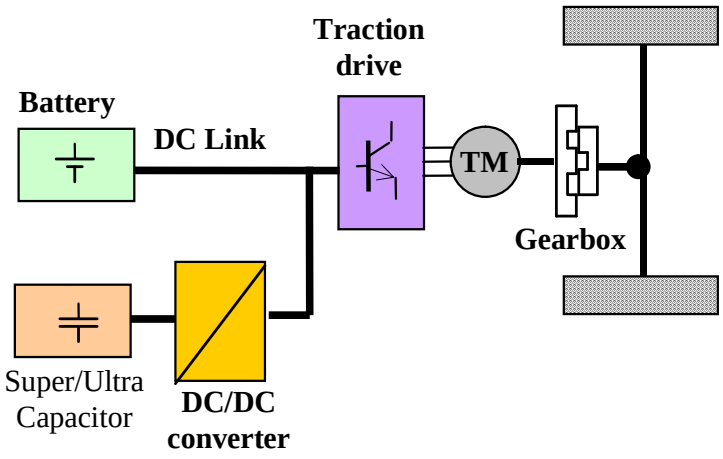

Fig. 1.5. Example all electric power-train system with a hybrid energy source.

1.3 Research Contributions

The author has contributed to a number of original developments in EV power-trains, include energy storage systems, traction machines and their interactive influence. These contributions are briefly described below:

(1) **Feasibility of all-electric energy storage system design is explored for a port crane power-train.**

A complete rubber-tired gantry cranes (RTGCs) power-train model is established and the energy storage system developed based on experimental test data, from which detailed component specification is made, accurate energy loss predicted, and hence, thermal management assessed and implemented. The interconnection issues in terms of energy flow, circuit voltages and current transients are assessed and hence the energy storage sizing procedure is suggested. In addition, according to the crane lift machine torque-speed requirements, considerations are taken into account for the hoist machine design.

(2) **Key design parameters for induction machines to realize a traction characteristic are identified, and hence the machine design procedure is proposed.**

Based on the combination of the induction machine 2-axis or *dq* model and steady-state equivalent circuit model key parameters for induction machine design to realize a traction characteristic are identified. Hence, a design procedure, independent of optimization algorithms or iterative calculation programs, is proposed to achieve traction characteristics with improved efficiency, power factor and field weakening capability.

(3) **A commercialized battery EV traction system is assessed by considering DC-link voltage and temperature variations, and hence system redesign methods are proposed.**

DC-link voltage and temperature variations are investigated for EV power-train design and the interactive influence between energy storage and traction machine design is evaluated. To overcome the issues of voltage and temperature variations, three system

design solutions are suggested. The trade-offs of these solutions is discussed in terms of electronic and machine packaging, and mitigation of faulted operation at high speeds.

(4) **A brushless permanent magnet machine with pole shoe topology is proposed to achieve better field-weakening performance.**

Comparison of interior permanent magnet (IPM) and surface-mounted permanent (SPM) machine topologies are studied, showing that brushless PM machines do not have to be salient to achieve traction torque-speed characteristics, which is the predominant but not wholly accepted school of thought, as is discussed in Chapter 6. Both of the two topologies suffer from high speed issues, in terms of on-load voltage distortion and torque ripple. These mechanisms are revealed and discussed. To makes full use of the respective advantages of the IPM and SPM machines, a pole shoe machine design is proposed.

1.4 Outline of the Thesis

Chapter 2 discusses the fundamentals of electrified power-train, including different energy storage technologies, traction machine technologies and their characteristics.

When designing an electric traction machine and associated power converter it is important to fully understand the system implications on machine design. To this end, a port crane is studied in Chapter 3 as an example of a more electric power-train. The simulation studies undertaken in this chapter highlighted the varied electrical power supply and mechanical loadings to which a traction machine system may be subject. Hence, Chapter 3 prepares the foundations for the studies in Chapter 4, 5 and 6.

In Chapter 3, a typical port crane loading cycle is analyzed and power flows deduced from which the values of the energy consumption and saving potential are calculated. Then alternative energy storage applications of diesel engine generators, battery packs, SCs, and flywheels in single and hybrid source configurations are discussed. A hybrid RTGC power-train model with appropriate power management is developed and the battery-SC hybrid energy storage systems are designed for both short- and long-period operation. Modern port cranes predominantly use inverter controlled induction machines, as opposed to earlier brushed DC based system. Hence, it is useful to note the wide acceptance of power electronic controlled machines in these applications.

In Chapter 4, therefore, the induction machine (IM) model is studied to determine the main parameters impacting on the machine torque and power capability applicable to the realization of a traction torque-speed characteristic. Importantly, the chapter attempts to align the theory behind the design of IM's for traction torque-speed capability with that of permanent magnet machines. In as much, the chapter identifies the key machine parameters against which to design. Based on this model analysis, an IM design procedure for traction applications is proposed, which improves machine performance. The machine design parameters are normalized in the per unit form and hence the proposed design procedure is applicable across different ratings.

The port crane study of Chapter 3 highlights the highly dynamic nature of the electrical system DC supply due to supply regulation and battery state-of-charge. Hence, Chapter 5

investigates the interactive influence between energy storage and traction machine design for a benchmark example all-electric vehicle power-train, the Nissan Leaf. The Nissan Leaf traction machine is evaluated and performance assessed by considering DC-link voltage and temperature variations typical of an automotive application, showing that the system lacks performance as battery state of charge decreases. An alternative traction machine design is proposed to satisfy the target performance. The vehicle power-train is then modified with the inclusion of a DC/DC converter between the vehicle battery and DC-link to maintain the traction system DC-link voltage near constant. A supercapacitor system is also considered for improved system voltage management. The trade-offs for redesigned systems are discussed in terms of electronic and machine packaging, and mitigation of faulted operation at high speeds.

During the electric machine studies undertaken in Chapter 5, operation of surface and interior permanent magnet machines above base speed introduced problems associated with the machine terminal voltage. These issues are explored in Chapter 6, where the Nissan Leaf IPM machine is again used as the benchmark machine, from which an example SPM machine with the same design constraints, is compared. The phase voltage distortion of both IPM and SPM machines are compared and the mechanisms are revealed. A new brushless permanent magnet machine topology with pole shoe rotor is proposed for reduction of peak current rating and voltage distortion.

Chapter 2

Electric Machine Fundamentals

2.1 Introduction

For all-electric vehicles or battery electric vehicles (BEVs) and series hybrid electric vehicles (HEVs), the electric traction machine is usually the only source of torque to drive the vehicle. Hence, the vehicle performance greatly depends on the electric machine traction performance capability, while the machine performance is impacted by the energy source, as will be discussed in Chapter 5. Hence, the electric traction machine should be designed to satisfy the traction characteristics within the output voltage and current constraints of the onboard energy source.

For BEVs and series HEVs, the traction machine performance is completely determined by the tractive effort versus vehicle speed. Typically, a maximum torque is required to accelerate the vehicle from zero speed to its rated speed within a specified time. For high speed cruising, less acceleration is required and hence high torque performance is unnecessary, but sufficient power is required to overcome road resistance and aerodynamic drag. Therefore, constant torque from zero to a defined base speed, followed by a wide constant power region from base to the vehicle maximum speed is typically required [8, 9]. Such a specification is often referred to as a traction characteristic. Ideally, the torque and power characteristics of the vehicle electric machine should closely match the vehicle tractive effort versus speed profile, as illustrated in Fig. 2.1.

Generally, torque and output power of electric machines are characterized by two classical operating regions: (i) constant torque, and (ii) constant power region, as shown in Fig. 2.2. In the constant torque region, the maximum torque capability is determined by the current

rating of the power electronic converter, while in the constant power region, flux-weakening is generally employed due to the DC-link limits. Thus, electric machine design cannot be undertaken in isolation, but has to be performed with consideration to the power electronic converter and energy source, which leads to a system-level design approach.

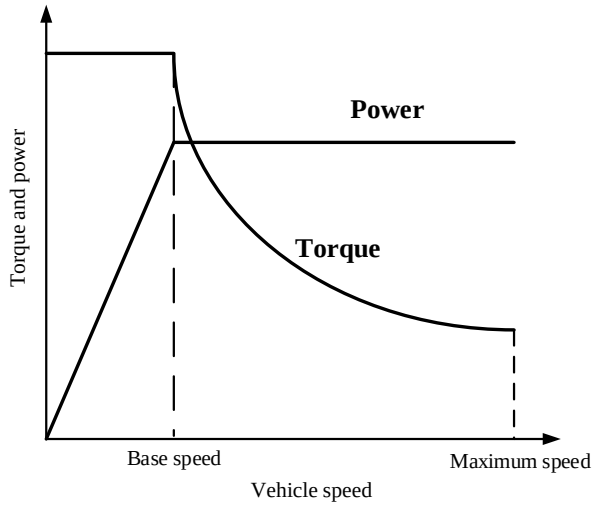

Fig. 2.1. Vehicle tractive effort versus speed profiles.

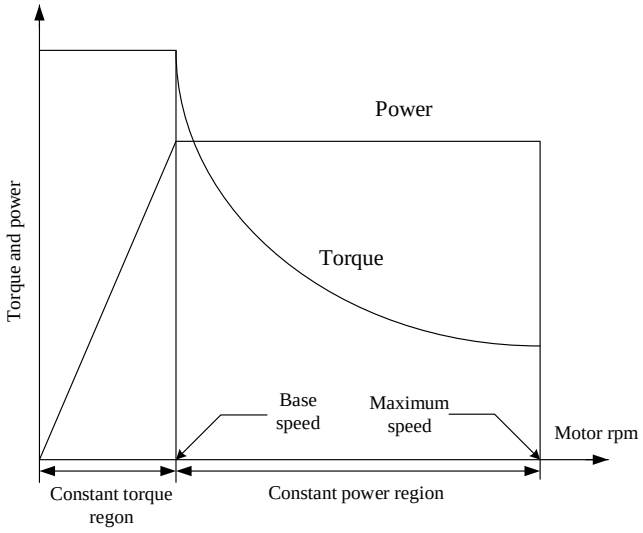

Fig. 2.2. Ideal torque and power characteristics of electric machines.

2.2 Electromagnetic Energy Conversion and Torque Production

Electric machines convert electrical energy into mechanical energy and vice-versa. The energy transfer is accomplished via the electro-magnetic field, involving a change of stored energy [10]. In Fig. 2.3, the electric machine is simply modelled as two coils. The position of Coil 1 is fixed and Coil 2 is rotating with speed of ω. The angle between the two coils, θ, is a function of time t, and L, M, V and i represent coil self-inductance, mutual-inductance, terminal voltage and current respectively with the subscript denoting the particular coil. For the general case, M, L_1 and L_2 can be functions of $\theta(t)$, although this may not be the case in practical machines.

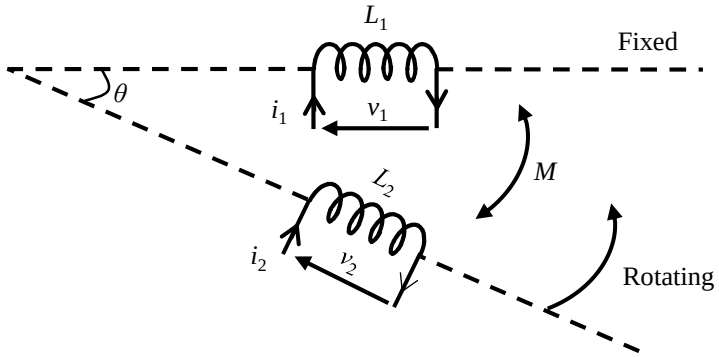

Fig. 2.3. Simplified two coil system.

For a loss-less system, the change in electrical energy, dW_e, equals to the change in stored energy in magnetic field, dW_f, plus the change in mechanical output, dW_m [10]:

$$dW_e = dW_f + dW_m \tag{2.1}$$

The stored energy in a magnetic field is:

$$W_f = \frac{1}{2} L_1 i_1^{\,2} + \frac{1}{2} L_2 i_2^{\,2} + M i_1 i_2 \tag{2.2}$$

Hence, the rate of change in stored energy is:

$$\frac{dW_f}{dt} = \frac{1}{2}\left[i_1^{\,2} \frac{dL_1}{dt} + L_1 \frac{di_1^{\,2}}{dt} + i_2^{\,2} \frac{dL_2}{dt} + L_2 \frac{di_2^{\,2}}{dt} \right] + \left[Mi_1 \frac{di_2}{dt} + Mi_2 \frac{di_1}{dt} + i_1 i_2 \frac{dM}{dt} \right] \tag{2.3}$$

Change in stored energy in time Δt is:

$$dW_f = \frac{1}{2} i_1^{\,2} dL_1 + \frac{1}{2} i_2^{\,2} dL_2 + i_1 L_1 di_1 + i_2 L_2 di_2 + Mi_1 di_2 + Mi_2 di_1 + i_1 i_2 dM \tag{2.4}$$

Similarly, the terminal voltage of coil 1 can be expressed as:

$$V_1 = L_1 \frac{di_1}{dt} + M \frac{di_2}{dt} + \left(i_1 \frac{dL_1}{d\theta} + i_2 \frac{dM}{d\theta} \right) \frac{d\theta}{dt} \tag{2.5}$$

where

$$\omega = \frac{d\theta}{dt} \tag{2.6}$$

$$\text{Instantaneous power} = vi \tag{2.7}$$

Hence, rate of change in electrical input energy is:

$$\frac{dW_e}{dt} = v_1 i_1 + v_2 i_2 \tag{2.8}$$

$$\frac{dW_e}{dt} = i_1 \frac{d}{dt}\left[L_1 i_1 + Mi_2 \right] + i_2 \frac{d}{dt}\left[L_2 i_2 + Mi_1 \right] \tag{2.9}$$

Change in electrical input in time Δt is:

$$dW_e = i_1^{\,2} dL_1 + i_1 L_1 di_1 + i_1 i_2 dM + i_1 M di_2 + i_2^{\,2} dL_2 + i_2 L_2 di_2 + i_2 M di_1 + i_1 i_2 dM \tag{2.10}$$

Change in mechanical output energy is:

$$dW_m = dW_e - dW_f \tag{2.11}$$

$$dW_m = \frac{1}{2} i_1^{\,2} dL_1 + \frac{1}{2} i_2^{\,2} dL_2 + i_1 i_2 dM \tag{2.12}$$

Change in mechanical output energy:

$$dW_m = \text{Torque} \times \text{displacement} \tag{2.13}$$

Therefore, the output torque for this change in mechanical energy is:

$$T = \frac{dW_m}{d\theta} \tag{2.14}$$

$$T = \frac{1}{2} i_1^{\,2} \frac{dL_1}{d\theta} + \frac{1}{2} i_2^{\,2} \frac{dL_2}{d\theta} + i_1 i_2 \frac{dM}{d\theta} \tag{2.15}$$

It can be noted from Equation (2.15) that torque is a function of the rate of change of inductances with displacement. The general torque expression of Equation (2.15) can be applied to all machine technologies, for example an interior permanent magnet (IPM) machine. For this case, the first two terms on the right hand side of the equation are terms relating to change in the machine magnetic structure, i.e. predominantly rotor saliency, while the third term models the torque contribution from the permanent magnets, i.e.:

$$T = \frac{1}{2} i_1^{\,2} \frac{dL_1}{d\theta} + \frac{1}{2} i_2^{\,2} \frac{dL_2}{d\theta} + i_1 i_2 \frac{dM}{d\theta} \tag{2.16}$$

2.3 Separately Excited BDCM with Traction Characteristic

Realization of the traction torque-speed characteristic illustrated in Fig. 2.2 from an electric machine is a consequence of the machine design parameters and control thereof. To understand the control features it is worthwhile considering the case of a separately excited brushed DC machine. Although this machine technology is not studied in this thesis, the analysis of this machine is general to that of the induction machine discussed in Chapter 4 and brushless PM machines discussed in Chapter 5 and 6, as encompassed by the General Machine Theory [10]. Therefore, to analyze the electric machine torque and power capability above base speed, the so-called field-weakening region, the separately excited brushed DC machines (BDCMs), is studied in this section. Due to the simple structure of this machine as illustrated in Fig. 2.4, the theory discussed in Section 2.2 can be straightforwardly applied. Coil 1 is replaced by the field coil and Coil 2 is replaced by the armature coils. Further, Coil 1 is fixed in space and Coil 2 now represents a pseudo-stationary coil fixed in space quadrature to Coil 1. Thus, the fields from Coil 1 and 2 are fixed in space quadrature by the action of commutator and brushgear. The machine armature coil voltage and field coil voltage can be expressed as:

$$v_a = M_{af}\omega_e i_f + R_a i_a + L_a \frac{di_a}{dt} \tag{2.17}$$

$$v_f = R_f i_f + L_f \frac{di_f}{dt} \tag{2.18}$$

where v, R, i, L and M are coil voltage, resistance, current, self-inductance and mutual-inductance respectively and the subscripts a and f represent armature and field. The machine electrical speed is ω_e.

In steady-state, the machine equations can be written as:

$$V_a = pM_{af} I_f \omega_r + R_a I_a \tag{2.19}$$

$$V_f = R_f I_f \tag{2.20}$$

where p represents pole-pair number and ω_r refers to the machine mechanical speed. Hence, the machine back-EMF is expressed as:

$$E = pM_{af} I_f \omega_r = k_o \omega_r \tag{2.21}$$

Since k_o is proportional to the field current, the back-EMF can be controlled by changing field current.

In steady-state, the machine armature power is given by:

$$P_a = V_a I_a = I_a k_o \omega_r + R_a I_a{}^2 = P_{mechanical} + R_a I_a{}^2 \tag{2.22}$$

which is composed of mechanical power and copper loss. Note, no expression is deduced from the fundamental electro-magnetic equations to account for iron loss. This loss mechanism is usually deduced empirically and accounted for later. Thus, the output power can be written as:

$$P_{mechanical} = T \omega_r \tag{2.23}$$

and output torque as:

$$T = \frac{P_{mechanical}}{\omega_r} = k_o I_a \tag{2.24}$$

Further, substituting Equation (2.19) into (2.24) yields:

$$T = \left(\frac{k_o}{R_a} \right) V_a - \left(\frac{k_o{}^2}{R_a} \right) \omega_r \tag{2.25}$$

Therefore, the machine torque-speed characteristic at a fixed field current and a fixed armature voltage is illustrated in Fig. 2.5. It can be noted that the machine maximum speed is proportional to armature voltage and inversely proportional to k_o. The machine characteristic crosses the torque axis at zero speed. However, this is usually an extremely high overload (OL) torque and hence overload armature current, operation at which would usually result in electrical or mechanical damage. Torque is usually limited to some maximum value, $T_{\max}$, by control of the armature current. This maximum torque may be at

the maximum thermal limit of the machine or at a continuous thermal limit as defined by the machine material properties (insulations). At this maximum torque a speed is usually defined, i.e. the base speed at full-load (or maximum load), as illustrated in Fig. 2.5. When supplying no-load, the machine speed will be limited to the maximum base speed, or no-load base speed, also defined on Fig. 2.5. Since the armature supply voltage is limited by the DC-link voltage, the machine base speeds are constrained by the DC-link voltage. To extend the machine speed above base speed the machine has to be field-weakened by gradual reduction of the stator field winding current as shown in Fig. 2.6.

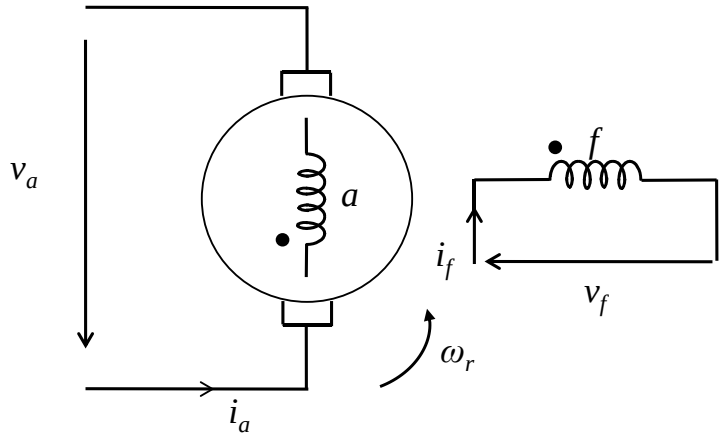

Fig. 2.4. Model of a separately excited brushed DC machine.

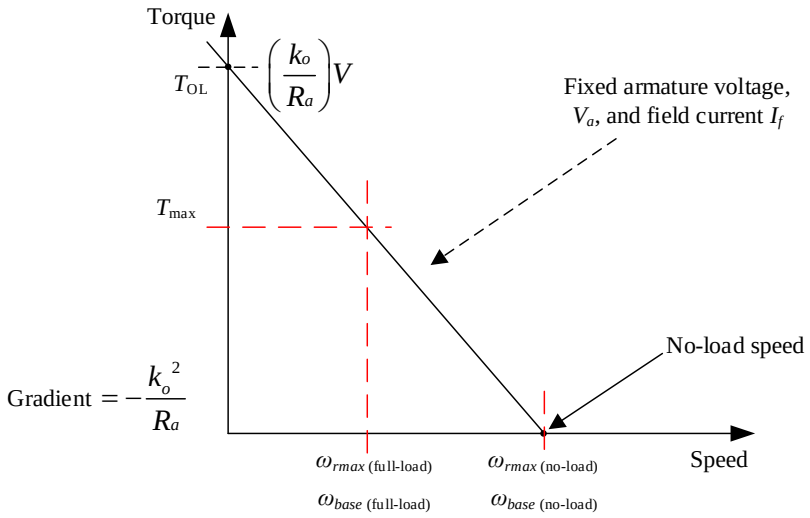

Fig. 2.5. Separately excited BDCM torque-speed characteristic.

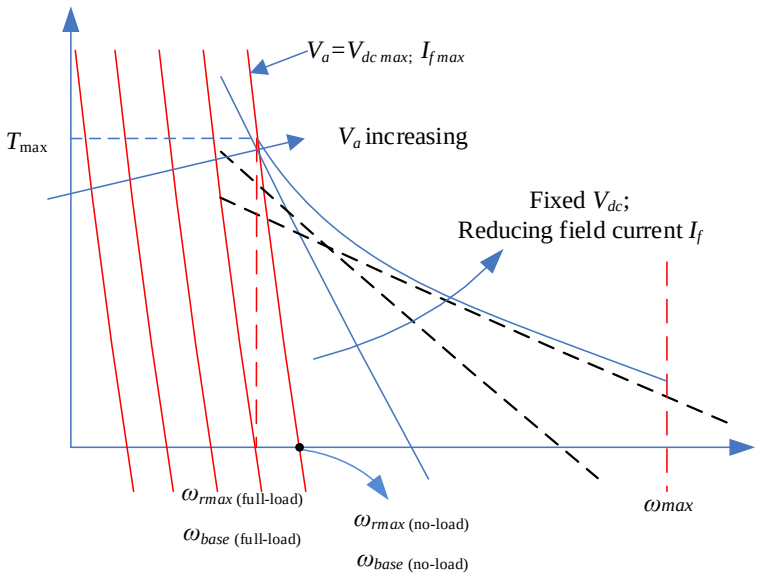

Fig. 2.6. Separately excited BDCM traction characteristic.

2.4 Generalized Machine Theory

For BDCMs, the commutator and brushgear ensures a fixed displacement between the rotor and stator fields, which gives a clear picture to understand the machine torque-speed characteristic. For induction machines, although there is a difference between the rotor mechanical speed and stator field synchronous speed, the induced rotor frequency results in no relative speed difference between the stator and rotor magnetic fields. Hence, there is a fixed spatial displacement between stator and rotor magnetic fields and hence the induction machine has the same torque producing mechanism as the BDCM. It is a similar case for synchronous machines, the stator and rotor fields are synchronized at the same speed, hence zero relative speed and a fixed spatial displacement between the stator and rotor fields.

All electromagnetic machines are a variation of a common set of principles which apply equally to DC and AC technologies, to generators and motors, to steady-state and transient conditions. However, 3-phase AC machines, such as induction, synchronous, brushless permanent magnet machines, suffer from the computational complexity of solving numerous coil equations, particularly those involving variables of position and time. While the solution of the machine coil equations is relatively straight forward by numerical techniques and modern day computational capabilities, transformation of machine equations to a 2-axis model gives a great insight into machine control requirements as well as the parameters that shape a machine's performance capability. To represent a multiphase, or more commonly a 3-phase AC machine as a 2-axis model similar in format to a BDCM machine, the 3-phase system is transformed to an equivalent 2-phase system, Clarke's transformation as illustrated in Fig. 2.7, converts the rotating 3-phase winding into a rotating 2-phase winding. Park's transformation is then employed to transform the rotating 2-phase winding into a stationary 2-phase winding, again as illustrated in Fig. 2.7. The Clark-Park transformations are discussed in many textbooks, hence no specific reference is given here.

With the 3-to-2 phase transformation, Generalized Machine Theory is introduced, which enables one to analyze the performance of all the diverse types of machines in terms the

torque, voltage, currents etc. In this way, most electromagnetic machines can be represented by a basic machine, the KRON primitive machine [10]. The primitive machine is a system of interconnected coils on 2 imaginary axes, the direct and quadrature axes. Most machine technologies can be analyzed by a suitable interconnection of these coils. The form of the primitive machine is chosen to be the simplest arrangement, whilst also being sufficiently general as shown in Fig. 2.8. Note, switched reluctance machine is one machine technology to which this modelling technique is not applicable, with other numerical techniques being applied for the analysis of this technology.

Induction, brushless permanent magnet and switched reluctance machines have all, with suitable design, been employed for EV traction. In the following section, the brushless permanent magnet machine is taken as an example and studied by considering the torque production and Generalized Machine Theory. The key machine design parameters to achieve a traction characteristic with consideration to the impacts of the power-train system are thus explored.

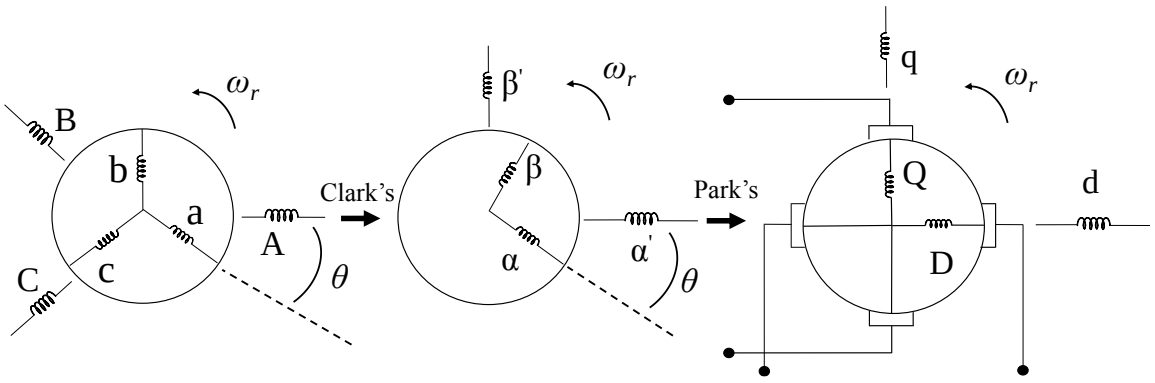

Fig. 2.7. Clark's 3-to-2 phase transformation and Park's 2-phase to 2-axis transformation.

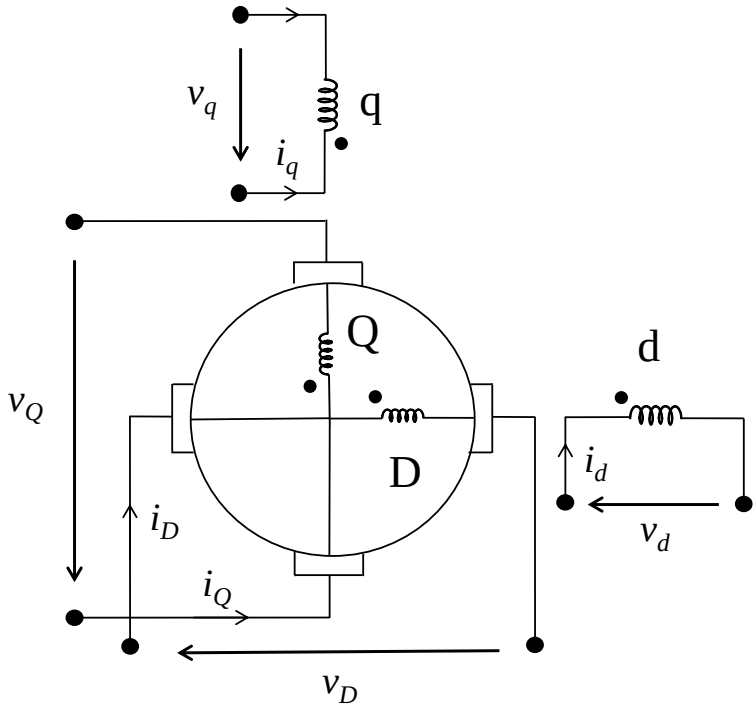

Fig. 2.8. Primitive machine.

2.5 Permanent Magnet Machine with Traction Characteristic

The appearance of high-performance rare-earth magnets made brushless permanent magnet (BLPM) machines suitable candidates for EV traction, since they promise high energy efficiency, high torque density under vehicular size and weight constraints [11-13]. Additionally, with the implementation of power electronic (PE) devices and rotor field orientation control, the torque and flux of BLPM machines can be separately controlled. More importantly, constant power operation over an extended speed range can be achieved by field-weakening operation of the machine, without compromising the Volt-Ampere rating of the traction converter [12, 14].

BLPM machines generally have two types of rotor topologies:

- interior permanent magnet (IPM) rotor, where magnets are buried within the rotor iron, and
- surface-mounted permanent magnet (SPM) rotor, where magnets are mounted on the rotor surface, [15, 16].

Typical IPM and SPM rotor structures are illustrated in Fig. 2.9. (a) and (b) respectively. The magnets, which have a relative permeability close to unity or that of air, appear as an airgap to the stator magneto-motive force. Therefore, for the SPM machine, the airgap reluctance is essentially uniform and hence the direct-axis reactance and quadrature-axis reactances are equitable. However, for IPM machines, high reluctance magnets are on the rotor direct-axis, while the quadrature-axis has low reluctance, soft magnetic paths such that the direct axis reactance is less than that on the quadrature axis reactance, resulting in rotor saliency [17].

It has been reported that BLPM machines have relatively high efficiency, high torque, and high power density for low speed operation because the excitation provided by the PMs is current free and essentially lossless (although there is same high frequency loss), while PM machines inherently have a short constant power range since the fixed magnets flux limits their extended speed range [18-21]. Here, a BLPM machine design procedure, based on a linear electro-magnetic model, is explored to realize a traction characteristic. The field-weakening capability of BLPM machines with consideration to IPM and SPM rotor

topologies is particularly discussed. Additionally, the machine performance is constrained by the other components in the EV power-train system. Additionally, the machine design also impacts on the design of the other power-train components, for example, peak voltage and current requirements.

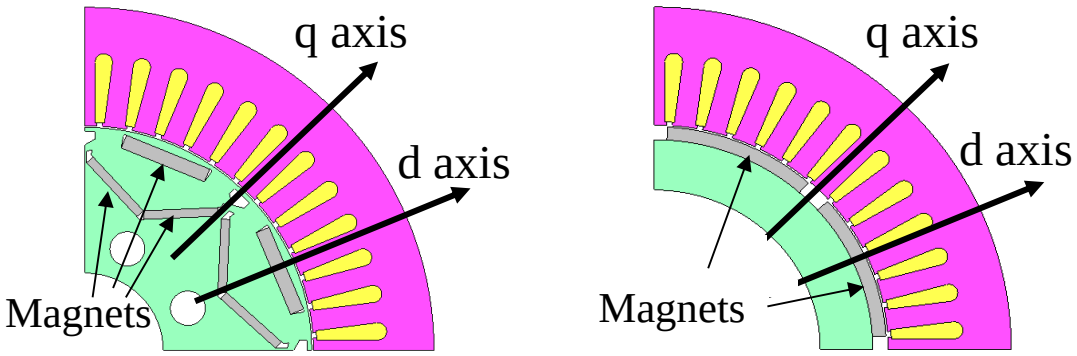

(a) IPM machine (b) SPM machine

Fig. 2.9. BLPM machines with IPM and SPM rotor topologies.

2.5.1 BLPM Machine Model

In this section, a linear electro-magnetic model of BLPM machines, coupled with a numerical direct search algorithm, is developed to determine the best choice of machine circuit parameters necessary to achieve a constant power capability over a wide speed range. This model is built by using the generalized machine theory and simplified with some assumptions. Firstly, magnetic saturation is neglected, which results in constant equivalent circuit inductances and magnet flux-linkage. Then, the stator winding distribution and machine inputs are assumed to be sinusoidal and electrically and mechanically balanced, also the airgap space harmonics and switching harmonics of the PE devices are neglected. In this way, the machine parameters which have significant influence

on the machine power capability over a wide speed range can be determined, the main outcome of the machine design procedure.

Since there are no electrical circuits on the rotor of BLPM machines, the machine per phase voltage equation can be represented as [10]:

$$\boldsymbol{V}_s = R_s \boldsymbol{i}_s + \frac{d}{dt}\left(L_s \boldsymbol{i}_s + \boldsymbol{\psi}_{PM}\right) \tag{2.26}$$

where R_s is the phase winding resistance, L_s is the phase synchronous inductance, $\boldsymbol{i}_s$ and $\boldsymbol{\Psi}_{PM}$ are phase current and PM flux space phasor.

The voltage equation in the synchronously rotating reference frame can be split into the direct and quadrature-axes:

$$V_{sd} = R_s i_{sd} + L_d \frac{di_{sd}}{dt} - \omega_e L_q i_{sq} - \omega_e \psi_{PMq} \tag{2.27}$$

$$V_{sq} = R_s i_{sq} + L_q \frac{di_{sq}}{dt} + \omega_e L_d i_{sd} + \omega_e \psi_{PMd} \tag{2.28}$$

where the subscripts *d* and *q* represent the *d*-axis and *q*-axis components and ω_e is electrical angular speed.

The PM flux is aligned with the direct-axis. In steady-state operation, the time derivative terms equate to zero. Hence, the voltage equations can be expressed as:

$$V_s \sin\delta = R_s I_s \sin\gamma + \omega_e L_q I_s \cos\gamma \tag{2.29}$$

$$V_s \cos\delta = R_s I_s \cos\gamma - \omega_e L_d I_s \sin\gamma + \omega_e k_o \tag{2.30}$$

where δ is the load angle, γ the current excitation angle and k_o is the permanent magnet back-EMF coefficient.

The voltage and current vectors and the associated angles are illustrated in Fig. 2.10 for motor operation. From Equation (2.29) and (2.22), the electrical angular speed can be derived from:

$$\omega_e = \left(\frac{-b + \sqrt{b^2 + 2ac}}{2a}\right) \tag{2.31}$$

$$a = \left(k_o - L_d I_s \sin\gamma\right)^2 + \left(L_q I_s \cos\gamma\right)^2$$

$$b = 2R_s I_s (k_o \cos\gamma + \frac{L_q - L_d}{2} I_s \sin 2\gamma)$$

$$c = \left(R_s I_s\right)^2 + V_s^2$$

Then, the rotor speed can be obtained from:

$$\omega_r = \frac{\omega_e}{p} \tag{2.32}$$

where p is the number of pole pairs.

The total electrical power includes copper loss and mechanical output (input) power, and is calculated from:

$$P = 3\left(V_{sq} I_{sq} + V_{sd} I_{sd}\right) \tag{2.33}$$

As with the BDCM, iron, windage and frictional losses are neglected at this stage of the analysis. Assuming a loss-less machine, which is reasonable for a high efficiency machine, the mechanical power, as a function of the machine parameters, phase current magnitude and current excitation angle is expressed as:

$$P_e = 3\omega_e \left(k_o I_s \cos\gamma + \frac{L_q - L_d}{2} I_s^2 \sin 2\gamma \right) \tag{2.34}$$

Hence, the electro-magnetic torque is derived as:

$$T_e = 3p \left(k_o I_s \cos\gamma + \frac{L_q - L_d}{2} I_s^2 \sin 2\gamma \right) \tag{2.35}$$

From Equation (2.35) it can be seen that in the constant torque region, for any magnitude of stator phase current, there is an optimum current excitation angle which leads to maximum electro-magnetic torque. As speed increases, this angle is chosen for maximum torque per Ampere operation until the maximum phase voltage constrained by the DC link is reached. Then machine enters to field-weakening region where the current excitation

angle is increased from the optimum value to 90 degrees electrical. Therefore, the d-axis component of the stator current vector is increased to reduce the air-gap flux.

For SPM machines, L_d equals to L_q, hence the torque per Ampere is maximized when the current excitation angle equals zero. For the IPM machine, the optimum current excitation angle is obtained by differentiating the electro-magnetic torque with respect to the current excitation angle and equating the result to zero:

$$\frac{dT_e}{d\gamma} = 3p\left[\left(L_q - L_d\right) I_s^2 \cos(2\gamma) - k_o I_s \sin\gamma\right] = 0 \tag{2.36}$$

Solving Equation (2.36) yields:

$$\gamma_{opt} = \sin^{-1}\left(\frac{-C + \sqrt{C^2 + 8}}{4}\right) \tag{2.37}$$

where $C = \dfrac{k_o}{\left(L_q - L_d\right) I_s}$

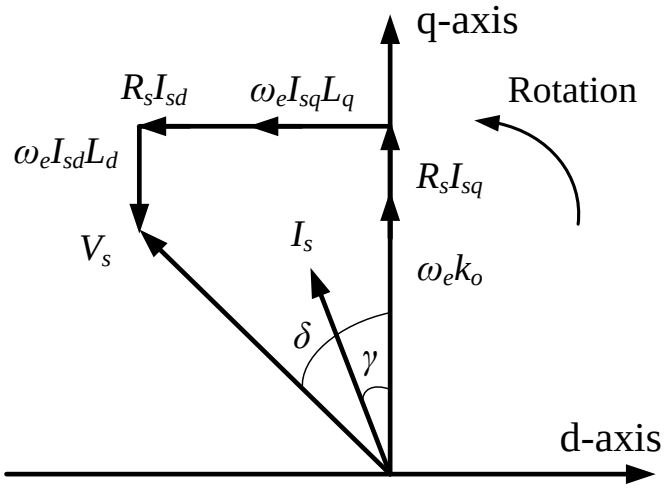

Fig. 2.10. BLPM machine vector diagram.

2.5.2 BLPM Traction Machine Design Procedure

In this section, an example SPM machine is studied. The machine model is normalized in per unit form, and analyzed to investigate the BLPM traction machine design procedure. Special attention is paid to the machine field-weakening capability. The values of the machine rated voltage and current at rated speed are chosen as the base values. Hence, the torque and output power at the machine rated operating point are equal to unity. All results are presented in normalized curves using a per unit system.

The maximum torque and power profiles of a SPM machine, constrained by the maximum phase voltage and current, are illustrated in Fig. 2.11, where it can be noticed that the machine is able to offer unity torque up to the base speed. However, above base speed, the terminal voltage is insufficient to enable the machine to maintain unity torque. Hence, the field-weakening capability is limited and the rated speed can be exceeded only by 30%; further reduce falling torque and power to zero at maximum speed. Since the machine is designed for vehicle traction effort, it must operate over an extended constant power speed ratio (CPSR), i.e. . In this case study, a 2.86:1 CPSR is set as the design target, this being a typical number specified by a number of automotive traction designs, the Nissan Leaf being one example, as discussed in Chapter 5.

In order to satisfy a 2.86:1 CPSR require, the expression of rotor speed is analyzed. Since the copper loss of the stator winding of traction machines is generally a relatively small proportion of the shaft output power and the resistive voltage drop is also negligible, the phase resistance in Equation (2.31) is neglected to facilitate easy access of the main design parameters impacting on extended speed operation. The simplified rotor speed can thus be expressed as:

$$\omega_r = \frac{|V_s|}{p\sqrt{\left(k_o - L_d I_s \sin\gamma\right)^2 + \left(L_q I_s \cos\gamma\right)^2}} \tag{2.38}$$

Above base speed, the current excitation angle is increased towards 90 degrees electrical at which the ideal maximum achievable speed becomes:

$$\omega_{r\,(\max)} = \frac{\left|V_{s\,(\max)}\right|}{p\left[k_o - L_d I_{s\,(\max)}\right]} \tag{2.39}$$

Therefore, according to Eqn. (2.31), the machine maximum speed limit is primarily depended on four parameters, viz:

(1) the supply voltage limit,

(2) the phase current limit,

(3) the machine back-EMF coefficient, and

(4) the direct-axis inductance.

More importantly, it can be noted that if the machine is designed such that:

$$k_o = L_d I_{s\,(\max)} \tag{2.40}$$

the maximum achievable speed is theoretically obtainable to be infinite.

According to Equ. (2.39), keeping the other parameters same, the maximum achievable speed of a BLPM machine is directly proportional to the supply voltage constraint. Fig. 2.12 illustrates the example machine torque and power versus speed profiles with a (1) 1.0 p.u., (2) 2.0 p.u. and (3) 2.23 p.u. voltage constraint. As shown, the increase in voltage yields a corresponding increase in torque and power at high speeds, and hence the high speed requirements can be satisfied. However, since the machine is required to provide a 0.35 p.u. torque at 2.86 p.u. speed to realise 2.86:1 CPSR, the rated speed of the PMSM is located to 2.27 p.u., which means the power ratings of machine and PE devices have to be increased to 2.27 p.u. and the machine field-weakening capability is not improved.

Fig. 2.13 illustrates the enhancement of machine torque and power profiles by increasing phase current constraint. It can be noted that the requirement of 2.86:1 CPSR could be achieved by raising the current constraint to approximately 3.22 p.u. From Equation (2.40), raising current constraint makes the value of the $L_d I_{s(\max)}$ product closer to the value of k_o. However, such current levels would give rise to issues. Firstly, copper loss and hence heat generation would be increased, which decreases machine efficiency and results in heat-dissipation problems. In addition, the thermal issue could cause a corresponding degree of irreversible demagnetization of the rotor permanent magnets. Moreover, both the power

rating of machine and PE converters have to be increased, which leads to overdesign at rated speed.

Given the power supply voltage and current constraints, one could adjust the machine parameters to best utilize the available power supply with-respect-to the converted power output. Here, the utility of the 2-axis model becomes self-evident. The main machine parameters influencing power at extended speed are the back-EMF coefficient and direct-axis inductance. Therefore, reducing k_o and increasing L_d is considered as follows.

The influence of reduction of k_o on machine torque and power performance are shown in Fig. 2.14, where it can be noted that none of the torque and power profiles can meet the target tractive requirements. Due to the reduction of the back-EMF coefficient, the machine maximum torque is decreased and the base speed is changed to a higher value. Consequently, varying the value of k_o only shifts the peak power to higher speed at the cost of losing power capability at lower speeds.

The impact of increasing the direct-axis inductance, L_d, on extended speed capability is illustrated in Fig. 2.15, where it can be noted that the machine field-weakening capability is improved at the expense of some loss of torque at the original base speed. To satisfy the power requirement at maximum speed, 4.5 p.u. direct-axis inductance is necessary. Although the machine base speed is shifted to a lower value, the power characteristic has been adjusted to be much closer to the required one. However, for any further increase in direct-axis inductance above 4.5 p.u., the value of the $L_d I_{s(\max)}$ product will be high than the value of k_o, resulting in a fall-off in both the peak power capability and the extended speed capability, due to the dominance of the winding impedance voltage drop on the total machine phase voltage.

By comparing the influences of adjusting the four parameters on the machine torque and power performance, the following conclusions are made:

(1) the increase in the supply voltage constraint will neither improve machine field-weakening capability nor rated operating performance;

(2) increasing the direct-axis inductance effectively facilitates field-weakening within the voltage and current constraints, but results in some reduction in torque and power at 1.0 p.u. speed;

(3) The loss in performance at base speed can be solved by increasing the phase current constraint or adjusting the value of the bac-EMF coefficient.

The direct- and quadrature-axis inductances of SPM machines can be considered equal, also the current excitation angle is zero from zero speed to base speed, thus the electro-mechanical power is simplified to:

$$P_e = 3\omega_e k_o I_s \tag{2.41}$$

Therefore, the modifications to the reference SPM machine design, which are required to realize the vehicle power-speed specification, are summarized as:

(1) increase the direct-axis inductance to 4.5 p.u. and satisfy the power requirement at maximum speed;

(2) increase both the phase current constraint and back-EMF coefficient to improve the power performance at unity speed. At the same time, the values of k_o and $L_d I_{s(\max)}$ have to be close enough, resulting in 1.13 p.u. for k_o and 1.06 p.u. for $I_{s(\max)}$. The power-speed profiles of the above design modifications are illustrated in Fig. 2.16.

For IPM machines, the direct-axis inductance is less than the quadrature-axis inductance, which results in rotor saliency. Hence, the machine torque consists of two components, i.e. permanent magnet or excitation torque and reluctance or saliency torque, as expressed by Equation 2.35. In order to investigate the influence of rotor saliency on the machine performance, the power-speed profiles of the reference SPM machine design ($L_d = L_q$) and 3 theoretical designs having quadrature-axis inductances varying from 2 to 4 times that of the unity direct-axis inductance are illustrated in Fig. 2.17. It can be noted that an increase in quadrature-axis inductance leads to an increase in the torque below base-speed, due to the reluctance torque component in the torque equation. However, changing the quadrature-axis inductance and hence the saliency ratio has no effect on machine field-weakening capability, although the reluctance torque provided by the IPM machine improves torque at low speed.

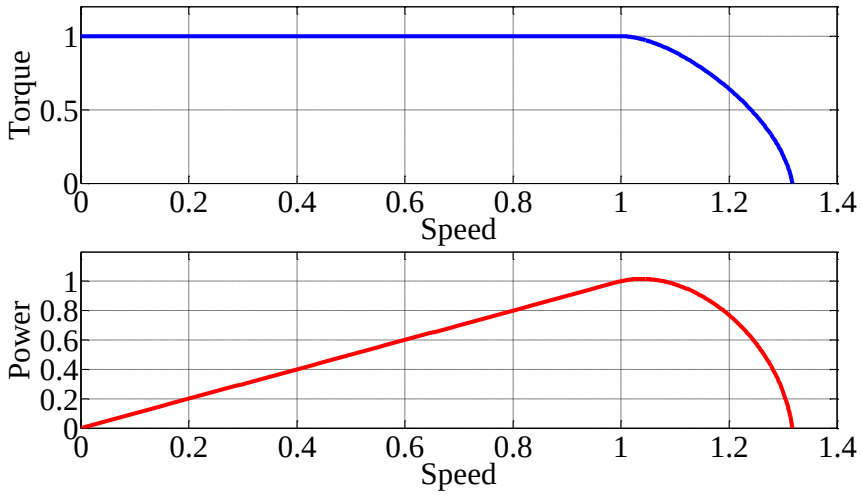

Fig. 2.11. Torque and power-speed profiles with unity phase voltage and current constraints.

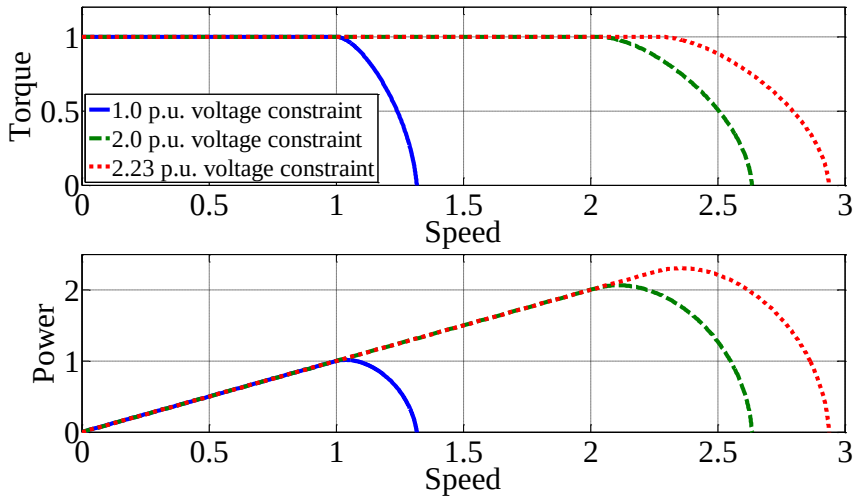

Fig. 2.12. Influence of phase voltage magnitude on field-weakening capability.

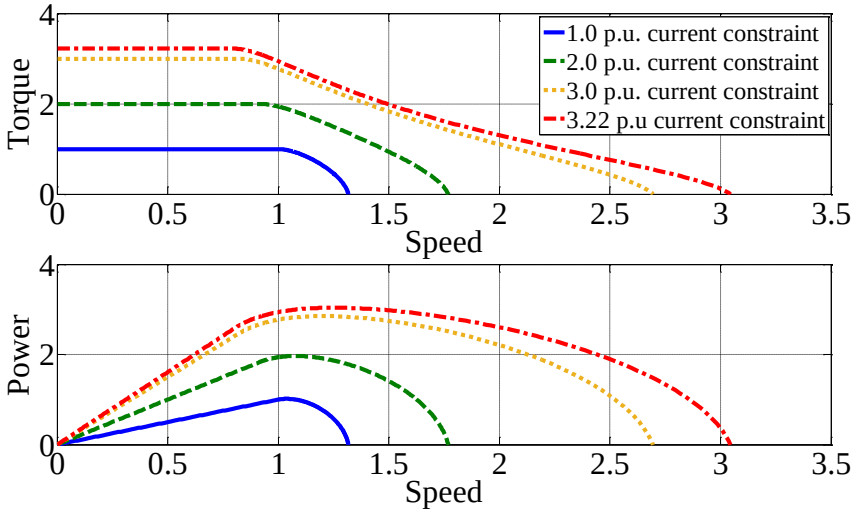

Fig. 2.13. Influence of phase current magnitude on field-weakening capability.

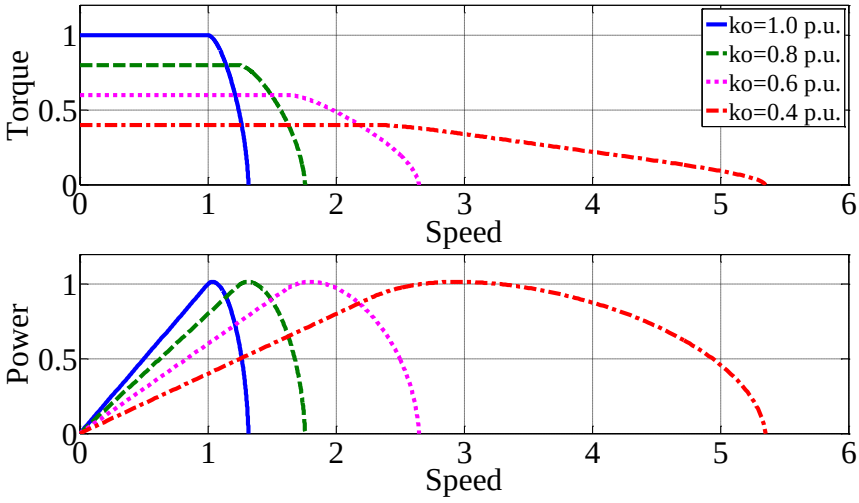

Fig. 2.14. Influence of emf coefficient on field-weakening capability.

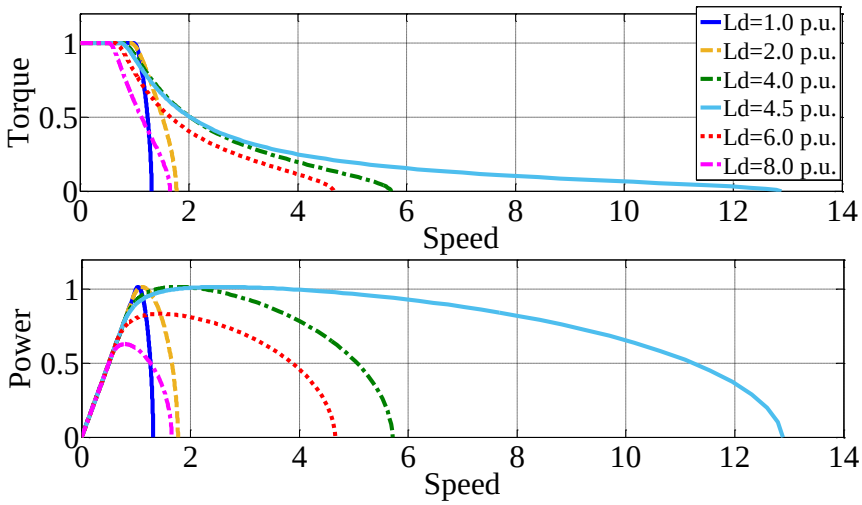

Fig. 2.15. Influence of direct-axis inductance on field-weakening capability (SPM).

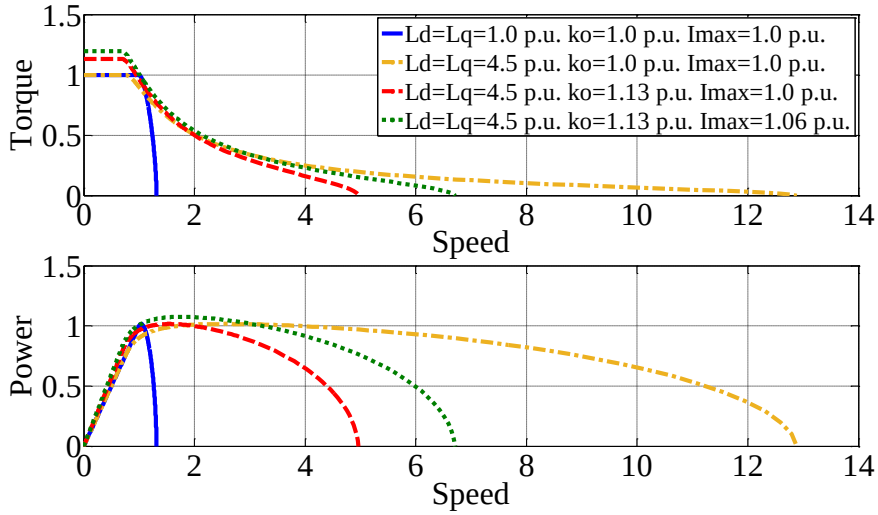

Fig. 2.16. Enhancement of machine torque and power profiles by proposed design modification (SPM).

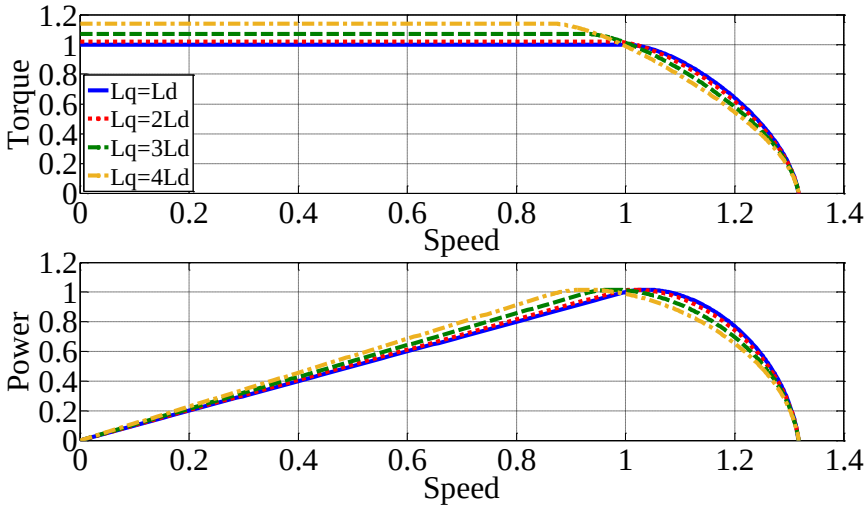

Fig. 2.17. Influence of increased saliency on field-weakening capability (IPM).

2.6 Conclusions

In this chapter, a BLPM machine design procedure, based on a linear electro-magnetic model, is implemented to investigate the impact of system parameters on the realization of a traction torque and power versus speed profile. The field-weakening capability of BLPM machines with consideration to IPM and SPM rotor topologies is particularly discussed. It can be shown that BLPM machines can be field-weakened to facilitate constant power operation over an extended speed range.

Analysis of a BLPM machine via a 2-axis machine model has highlighted the main machine parameters which have the greatest influence on its extended speed capability within the constraints of power supply voltage and current limits, viz:

(1) the phase current constraint $I_{s(\max)}$,

(2) the back-EMF coefficient k_o, and

(3) the direct-axis inductance L_d.

Therefore, the BLPM machine design procedure to realize a traction torque and power versus speed specification are summarized as:

(1) design the machine at the rated operating point, i.e. peak torque at base speed,

(2) increase the direct-axis inductance to back-EMF ratio to satisfy the power requirement at maximum speed, although the machine power performance at unity speed will be impacted;

(3) increase both the phase current constraint and back-EMF coefficient to improve the power performance at unity speed, at the same time, the values of k_o and $L_d I_{s(\max)}$ have to be close enough.

DC-link voltage and temperature variations are critical issues when designing BLPM traction machines. The condition of high temperature and low voltage determines the worst case for the BLPM machine. Therefore, the machine should be designed to satisfy the torque-speed requirement at worst case ambient and supply, which results in an obvious over design when the machine operates in more agreeable ambient or when the supply (or battery) voltage is corresponding to maximum state of charge. These issues will be studied in subsequent Chapters.

In Chapter 3, the combination of different energy and power sources in a vehicle power-train will be discussed by way of an example hybrid electric vehicle, a more electric rubber tyred gantry crane (RTGC) vehicle. Port crane application invariably use induction machines as the main energy converters due to cost issues.

The analysis of Chapter 3 shows that the port crane machines require specific traction torque and power versus speed requirements. Chapter 4 therefore studies the induction machine analysis and tries, as with the IPM and SPM study of this chapter, to identify the main parameters influencing such realization of a traction characteristic with the supply voltage and current constraints.

Adding supercapacitors (SCs) in parallel with the battery is one way to improve the DC-link voltage variation. In addition, implementing a bidirectional DC/DC converter between the battery and DC-link is one technique to give controllable DC-link voltage to the vehicle traction machine. Potentially, both of the two methods reduce the mass and power rating of the traction machine and simplify the torque control strategy, but as a trade-off, they require more power electronics, more complicated control of the system and additional hardware, e.g., SCs.

In Chapter 5, the vehicle power-train system will be modified with the inclusion of a DC/DC converter and SC to compare with the original system. The benefits and drawbacks in terms of system rating, efficiency, mass and volume will be evaluated.

Chapter 3

Energy Storage System for a Port Crane Hybrid Power-train

3.1 Introduction

Ports, where cargoes are loaded and unloaded and conveyances interchange, are comprehensive hubs of the marine transportation network and very important in the whole international business of goods transportation. Over the last 20 years, China has witnessed spectacular port development, with the volume of freight handled in the main coastal ports soaring 940% from 743 million tonnes in 1994 to 7696 million tonnes in 2014 [22]. In recent years, the cargo throughput of Chinese coastal ports has maintained a double-digit growth, a rate that is expected to remain strong over both the medium and longer terms. Despite its contributions to regional economic growth, the port industry requires significant energy consumption and is a source of global climate change and emissions are detrimental to public health [23, 24]. According to the Chinese transportation industry standards, the energy consumption is 360 tonnes of standard coal equivalent (SCE) per million tonnes of cargo throughput [25]. The energy consumption of cargo handling in the main costal ports of China for the past 20 years is illustrated in Fig. 3.1, which shows that the energy consumption for cargo handling in 2014 has increased by approximately 9 times from the amount in 1994. Such energy consumption has become one of the contributing sources of environmental pollutants in China. Since diesel-engine generators are widely used as their power source [26, 27], port cranes are contributors to energy and environmental problems both in the port area and the wider port locality. In order to reduce its adverse effects,

hybrid or more electric cranes with energy regeneration techniques are being considered to replace the traditional crane systems.

A crane system is a type of large machinery found at ports for loading and unloading intermodal cargoes [28]. In the yard of the port terminal, Rubber tyred gantry cranes (RTGCs) remain the primary machines for moving containers and represent a large fuel consumption at a typical port. Fig. 3.2 (a) illustrates an example traditional RTGC supplied by a diesel internal combustion engine generator set (ICE GenSet) and its configuration (lateral and front views), along with the core components, as shown schematically in Fig. 3.2 (b). The RTGC is able to move containers in a 3D space by its gantry, trolley and hoist in terminal yard. According to the conservation of energy, when hoisting up or accelerating the containers, cranes transform fuel or electrical energy into kinetic and gravitational potential energy; when hoisting down or braking the containers, large amounts of energy could be fed back to the system if the system could recover or provide some energy storage. Traditionally, the feedback energy is consumed by electrical resistance and wasted as heat [23]. Grid-powered electric RTGCs, equipped with a cable reel connecting to the grid terminal, is a solution for regenerative energy recovery. According to [29, 30], it reduces both the fuel consumption and emissions by approximately 90% compared to conventional RTGCs. Although this scheme results in significant improvement in terms of energy consumption and emissions, a huge port reconstruction is required. The grid-powered RTGC also results in some problems including the impact on power grid and, in particular, poor mobility of the RTGCs. Therefore, diesel powered ICE GenSets are generally used to provide the on-board energy for RTGCs.

For on-board energy storage RTGC, hybrid energy source system is an efficient solution, which also leads to a compact system. Hybrid energy source systems (HESS) mainly include two types of energy storage devices [28]. One, with high energy density (typically an electro-chemical battery), which provides extended operating time; the other, with high power density and reversibility, operate at acceleration and regenerative braking, examples being supercapacitors (SCs) or flywheels. For the port crane application, the rating of the energy storage device is mainly determined by the peak power demand in the hoist up

operation. However, a RTGC is running nearly 90% of the time in a light load operation and the time for container hoisting up occupies less than 20% of the whole operation time, so in most operation time, cranes do not require the peak driving power [26, 31]. Therefore, the selection of energy storage system will significantly influence the size and cost of the whole motoring and energy recycling system.

This Chapter mainly focuses on the RTGC energy storage sizing and machine design investigation. Firstly, the driving cycle from a case study of a typical RTGC is presented. Since the power and energy requirements determine the specification of the hybrid power-train system, the power flow of the crane system is analyzed and the value of the energy consumption and saving potential is calculated. Then alternative energy storage applications of diesel engines, battery packs, supercapacitors and flywheels in single and hybrid source configurations are discussed. Based on the system specification, a hybrid RTGC power-train model with proper power management is developed using Matlab/Simulink. For storage components, the ZEBRA battery and Maxwell supercapacitor are modelled in detail including their thermal analysis.

ZEBRA battery was chosen because it was validated by test data and thermally managed. The optimization of the battery-supercapacitor hybrid energy source system is investigated for both short and long period operations. The design of the hoist, trolley and gantry machines are studied based on the crane operating requirements.

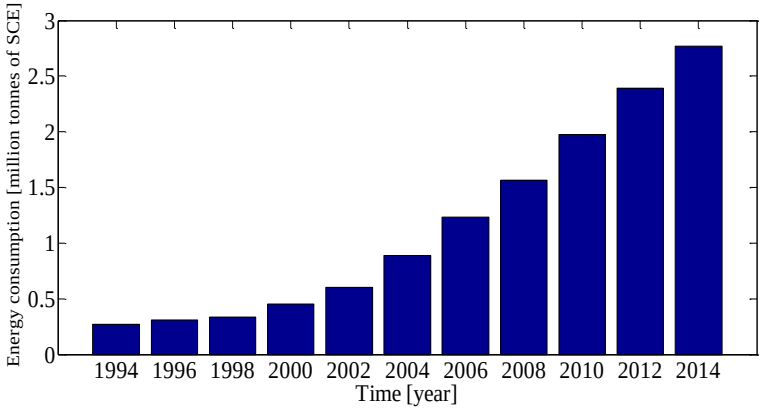

Fig. 3.1. Comprehensive energy consumption of cargo handling in the main costal ports of China for the past 20 years.

(a) Traditional diesel ICE GenSet RTGC.

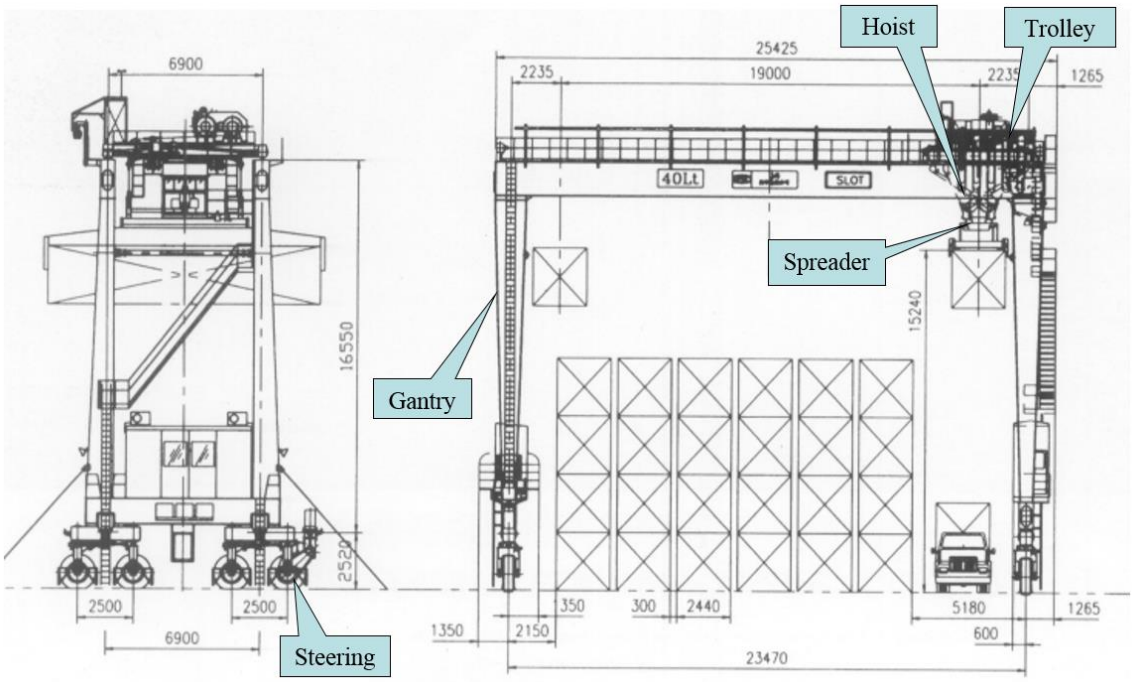

(b) RTGC configuration.

Fig. 3.2. Traditional diesel ICE GenSet RTGC and its configuration.

3.2 Existing Study on Energy Storage Sizing

Traditionally, the diesel ICE GenSet is sized for the peak power demand of the hoist motor, which results in a large GenSet system. To decrease the fuel consumption and emission caused by traditional large diesel ICE GenSet, SCs, flywheels or Lithium-ion batteries have been proposed as power buffers to downsize the GenSet [24, 26, 32, 33]. However, those hybrid systems are still fossil fuel-dependent since the ICE GenSet still provides the mean energy input. There is no academic research work reported on all electric power/energy systems for RTGCs. For battery-only systems, a significant battery mass is required since the RTGCs need to operate for a number of hours on a single charge. However, as battery technologies have made continued progress in terms of cost, energy density and lifetime over the last decade [34], their application becomes more practical and realistic. In 2012, a battery-only RTGC was transformed from a traditional RTGC by a Chinese government project [31]. The project showed that a battery-only powered RTGC maintained the same mobility as the traditional RTGC. More importantly, this all electric RTGC significantly reduced fuel consumption, emissions and maintenance costs. According to the project data, the battery-only system is an effective long term solution for RTGCs due to the environmental and economic benefits [31]. To reduce battery size, extend battery efficiency and cycle life, battery-supercapacitor hybrid energy source systems have been considered as an effective solution for automotive vehicular technologies as reported in [35-37], concepts which may also be applied to the RTGC HESS. On the other hand, economical consideration of HESS is not studied here and is subject of future research. Since the operational characteristics and driving cycle of RTGCs are different from electric vehicles, the Battery-SC HESS for RTGC application is investigated in this paper and a design methodology is proposed.

Sizing of the battery and SC systems for all-electric and hybrid-electric vehicles (EVs) is one of the major issues for HESS design. Although there is no existing literature for Battery-SC HESS cranes, there are many publications that discuss EV energy storage system sizing. In [38, 39], Sadoun et al introduces a method for HESS sizing, by formulating numerical optimization problems. However, the battery and SC models are

highly simplified and only nominal data from manufacturers' datasheets are included, which leads to rough results and estimates. R. de Castro et al [40] present two methodologies for HESS sizing, i.e. filter-based sizing and optimal sizing. The optimal sizing method relies on a nonlinear optimization problem and seeks the minimization of the installation and electrical charging cost of the energy source. Compared to the optimal sizing method, the filter-based sizing method is simple and numerically efficient, but only provides a rough approximation of ideal sizing, mainly because it only employs a simplified voltage-resistor model for the battery and SC and assumes that the peak power and energy capacities of each source are single value parameters, which is not the case in a practical application. In [41], Shen et al explore different combinations of batteries and SCs to satisfy different requirements in terms of EV range and acceleration time. For certain EV performance, a feasible region of different combinations of the number of batteries and SCs is determined and then an optimization problem is formulated to minimize the HESS mass in this feasible region. Shen et al [42] present a trade-off between battery cycle life and HESS size. Thereafter a multi-objective optimization problem is defined to both minimize the HESS mass and capacity loss of the battery. A sample-based optimization algorithm is required for solving this problem. In order to give a more accurate optimization sizing result, [43] and [44] take into account state-of-charge (SoC) related nonlinearities in the battery internal resistance and open-circuit voltage and SC capacitance. Hence, a large number of constraints are included in the nonlinear optimization, and the discretized equations at every sample interval need to be considered. Moreover, the battery-SC HESS sizing leads to a mixed-integer nonlinear optimization problem in [45]. Ostadi and Kazerani [45] chose a modified PSO algorithm, a population-based optimization technique, to solve the problem.

Most of the works in the literature employ optimization methods to size the HESS. Although simplified models are suitable for numerical optimization, they neglect or only roughly estimate the power loss of the energy storage units. Hence, the actual power, energy performance and efficiency of the energy storage units cannot be fully described yielding, at best, only idealized sizing results. However, the nonlinearity of the energy storage units

make it too complicated for conventional derivative-based methods to solve the optimization problem without compromising system design in some aspect, for example actual loss and temperature rise, so that additional optimization algorithms are required.

This Chapter combines detailed battery and supercapacitor models to fully assess the HESS requirements for a RTGC, a special form of hybrid EV, from which detailed component specification can be made, accurate energy loss predicted and hence thermal management assessed and implemented. The models, which are calibrated and validated by real road vehicle test data [46], can be used to assess the battery and SC dynamics and to understand the interconnection issues in terms of energy flow, circuit voltages and current transients. Hence, the sizing procedure does not have the issue of rough results and estimates. In addition, since the RTGCs are designed for fixed time operation, the HESS efficiency and thermal management is also of importance. This Chapter suggests different design strategies for different scenarios of short and long operation periods. Many papers discuss similar concepts for road vehicles, however, the application to port cranes has not been reported previously.

The contribution of this Chapter is the presentation of a study that encompasses system losses, thermal management, component mass, volume and system dynamic operation. These aspects have not previously been discussed in detail and applied to a full vehicle system.

3.3 Power-train Architecture

The RTGC power-train, including power/energy source, power electronic converters and electric machines, plays a crucial role in the crane operation process. Due to the advantages of simple structure and control, a series hybrid power-train system is suitable for the crane application. On the supply side of the power-train system, generally, there are various energy/power storage options which can supply energy/power in single configuration or in different hybrid combinations, as illustrated in Fig. 3.3. For single power/energy source configurations, the diesel ICE GenSet, with high energy density, are traditionally utilized. However, since the power rating of the diesel ICE GenSet is determined by the RTGC peak power requirement, it always operates in the low efficiency region, which leads to unnecessary fuel consumption and emissions. Moreover, the energy regenerated during the machine braking is wasted. The SC and flywheel are pollution free power/energy storage source with high efficiency [40-42]. Although both of them have high specific power, their low specific energy will result in a large and heavy components if they were considered to meet the energy requirement of the RTGC. By contrast, electro-chemical batteries, which have much higher specific energy than the SC and flywheel, can be a suitable candidate to replace the diesel ICE GenSet. For hybrid power/energy source configurations, SC or flywheel connecting in parallel with diesel ICE GenSet downsizes the GenSet system and reduces the fuel consumption and emissions. The supercapacitor bank or flywheel operates as a power buffer to supply energy in the event of peak power demand and store energy in the event of regeneration. However, this improved system still relies on the GenSet as the main source of energy and cannot maximize the energy saving and minimize emissions. The combination of battery and supercapacitor realizes zero emissions at point of application, is independent of crude oils, and enhances the system efficiency and reliability. In addition, there are many different ways for power electronic converters to connect the power/energy sources. Besides the AC/DC converter installed in series with the diesel ICE GenSet, the DC/DC converters, in Fig. 3.3, are optional. Since this chapter is focused on the modelling and sizing of the energy storage system, the multiple energy storage topologies are beyond the scope of this chapter, although their application is conceptually

the same. Here, the battery is directly connected to the DC-link and a DC/DC converter is used to interface the supercapacitor to the DC-link. In energy consuming mode, the power/energy sources provide the system DC-link, which in turn supplies the crane electric machines via DC/AC converters; in the regenerative mode, the electric power flows in the opposite direction managed via the power converters. Due to low cost, robust, mature manufacture and control technique [47, 48], variable speed induction machines driven by power converters are usually utilized as the driving units for the gantry, trolley and hoist drive. This Chapter does not consider the electric machine design in any further detail, although induction machine design will be discussed in Chapter 4.

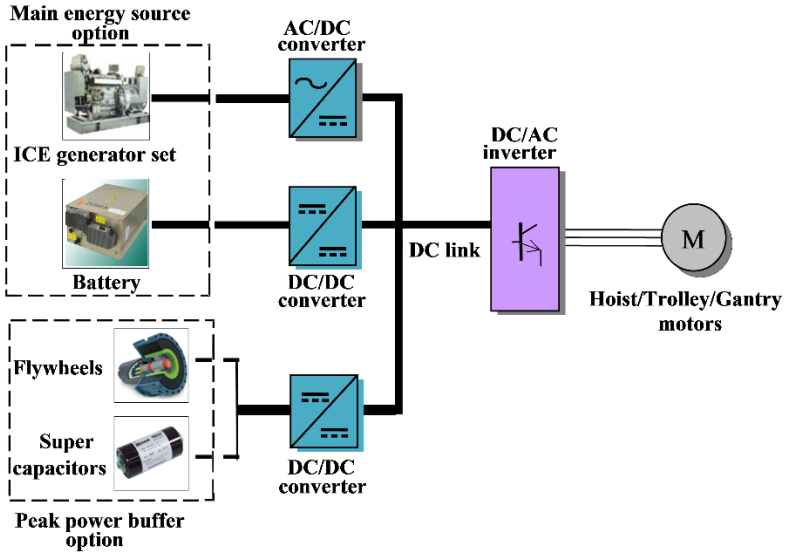

Fig. 3.3. Hybrid power-train components and their associated interconnection.

As a solid rule, the power and energy supply of the energy storage system must be sufficient to satisfy the system power and energy demand. However, the different power/energy storage device candidates shown in Fig. 3.3 provide various potential operating modes:-

(i) the main source of energy supply,

(ii) both energy source and power buffer and

(iii) energy recovery,

which could be correspondingly utilized for different conditions such as light load, full load and braking [49, 50]. Therefore, to achieve a compact volume, light weight power-train system with high performance and high efficiency, appropriate power/energy source should be selected and combined.

3.4 System Power and Energy Study

In order to determine the duty rating specification of the crane power-train system, the load cycles of a typical RTGC with its maximum load is studied in this section. A simplified model of the RTGC dynamics is built to estimate the power and energy requirements of the power-train system. The RTGC dynamic model will also be used to assess different energy source combinations to achieve an energy efficient combination.

For hoist operation, the containers are lifted up and down by the hoist motor driving the pulley drum via a gear box with its corresponding gear ratio. The total force required from the drive train can be expressed from first principles as:

$$F_t = F_r + mg + m\frac{dv}{dt} \tag{3.1}$$

where F_r is the friction between driving drum and rope, m is the container and spreader mass, g is the gravitational acceleration and v is the container velocity.

Then the drum angular velocity in terms of container velocity and hence the power required for the hoist operation are derived as:

$$\omega_d = \frac{v}{r_d} \tag{3.2}$$

$$P_h = vF_t + \omega_d J_d \frac{d\omega_d}{dt} \tag{3.3}$$

where r_d is the drum mean radius and J_d is the drum inertia.

Therefore, the hoist machine output power and torque can be calculated, viz.:

$$P_1 = w_1 J_1 \frac{dw_1}{dt} + \frac{P_h}{N_{GB}} \tag{3.4}$$

$$T_1 = \frac{P_1}{\omega_1} \tag{3.5}$$

where w_1, J_1 are the hoist machine angular velocity and inertia respectively, and N_{GB} is the gearbox efficiency.

Having determined the machine output power, the power and energy required from the energy sources can be calculated by considering the device efficiency, viz:

$$P_{s1} = \frac{P_1}{N_C N_E} \tag{3.6}$$

$$E_{s1} = \int P_{s1} dt \tag{3.7}$$

where N_C and N_E are the converter and machine efficiencies respectively.

Equations (3.1) – (3.7) provide the calculation in the case of machine motoring. In the case of regenerating, Equations (3.4) and (3.6) are changed to (3.8) and (3.9) respectively:

$$P_1 = w_1 J_1 \frac{dw_1}{dt} + N_{GB} P_h \tag{3.8}$$

$$P_{s1} = N_C N_E P_1 \tag{3.9}$$

By the same principle, the machine torque and output power, and the power and energy required from the energy sources can be derived respectively for trolley and gantry operation. Equations (3.1) – (3.9) are implemented in an RTGC dynamic model which is solved using the RTGC parameter specifications given in Table 3.1 of the system dynamic power and energy demands during a representative loading cycle. The velocity and power profiles of the power-train system for a typical duty cycle are illustrated Fig. 3.4. The average and peak power demand of one load cycle in the worst case are tabulated in Table 3.2, which indicates that the average power differs from peak power by a factor of 0.06, 0.017 and 0.19 for hoist, trolley and gantry machines respectively. Hence, the power rating of the main energy supply can be chosen to be much lower than the peak power assuming that the exceeded power will be provided by the power buffer.

Based on the calculation of the case study, for one duty cycle with maximum load (40.5-tonne containers), the energy consumption is 4.245 kWh and the regenerative energy potential is 2.255 kWh, which indicates that 53% of the consumed energy can be potentially recycled. Therefore, it is necessary to design an energy recovery power-train system for port crane energy saving.

The RTGC system assessment criteria are summarized as follows:

1) The electric machines, including the hoist, trolley and gantry machine, should satisfy the RTGC torque and speed requirements.
2) The energy storage system and power electronics should be capable to offer the peak power of the electric machines.
3) The energy storage system should be capable to supply energy for 16-hour operation or 4-hour operation, which depends on the different type of RTGCs.

Table 3.1. Example RTGC Specification [58].

RTGC parameters	Quantity	Units
Self-weight	138	tonne
Lifting height	18.1	m
Gantry span	23.6	m
Travel wheel gauge	9.2	m
Rated load lift	40.5	tonne
Hoisting with no load/rated load	56/28	m/min
Trolley travel with and without load	70	m/min
Gantry travel with no load/rated load	130/70	m/min

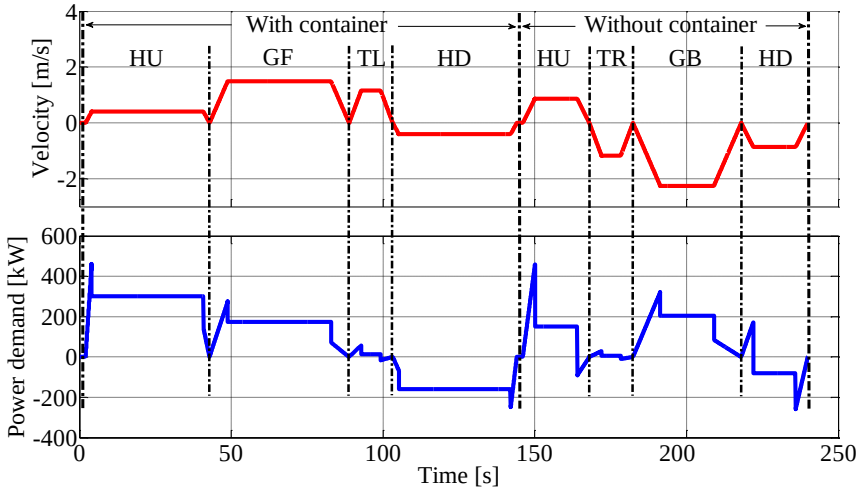

Fig. 3.4. Hoist, gantry and trolley speed and power demand (HU: hoist up, HD: hoist down, GF: gantry forward, GB: gantry backward, TL: trolley left, TR: trolley right).

Table 3.2. Summary of Power Requirements from Energy Storage.

	Average power (kW)	Peak power (kW)	
Hoist	29.6	Consuming	460
		Regenerative	250
Trolley	1	Consuming	60
		Regenerative	15
Gantry	51.6	Consuming	270
		Regenerative	0
Total	82.2	Consuming	460
		Regenerative	250

3.5 Pure Battery Energy Storage Design

To satisfy the load requirements, energy storage devices with high power and high energy are desired. As mentioned in Section 3.3, there are a few options, such as ICEs, electro-chemical batteries, supercapacitors and flywheels that may be used for the crane power-train, as discussed in Section 3.3. Considering the technical features of each energy storage device, ICEs or electro-chemical batteries can be used individually or chosen as the main energy source in the hybrid system, while supercapacitors or flywheels can operate as a peak power buffers in a hybrid system. In this section, the battery is modeled and operates as the only power/energy source for the RTGC. The simulation results are compared with the conventional diesel GenSet RTGC.

Traditionally, the diesel ICE GenSet, which provides electric power, is the only power and energy source for hoist, trolley, and gantry operation. Its power rating is determined by the peak power demand of the crane full load operation. In this case study, the system transient power demand is 0-460 kW in 2 seconds, which equates to a constant torque loading on the system prime mover, the ICE. This usually necessitates an overrating of the prime-mover by up to 50%. Consequently, a 700 kW diesel ICE GenSet is selected. However, during the operation duration, the maximum power output of the diesel ICE GenSet is only required in the heavy load (30-40.5 tonne container) hoist-up operation, which is only in 4 percent of the operating time. In addition, crane idle time is approximately 50 percent [31], while the diesel ICE GenSet must be in operation whether a container is being lifting or not. Moreover, the energy regenerated during crane braking is wasted. Due to the large amount of fuel consumption and greenhouse gas emission by the diesel ICE GenSet, turning it into an eco-friendly energy source is considered. An electro-chemical battery, which realizes energy recycle and zero emission, is a potential energy source to replace the diesel ICE GenSet.

Sodium-Nickel Chloride or ZEBRA battery [51], as shown in Fig. 3.5 which has good power and energy densities, is a promising electro-chemical battery candidate for crane application. The ZEBRA Z5C battery data-sheet is presented in Table 3.3. A ZEBRA Z5C battery model is developed in [52] and the equivalent circuit of a ZEBRA Z5C battery cell

is shown in Fig. 3.6. In the equivalent circuit, the open-circuit EMF of the battery is a function of its state of charge (SoC), as illustrated in Fig. 3.7, and the internal resistance varies with the magnitude of charge/discharge current and SoC, as illustrated in Fig. 3.8. Both the non-linear open-circuit EMF function and resistance characteristics are obtained from cell experimental test data for battery dynamics assessment. The model performance, in terms of battery voltage and current transients and energy flow, is validated by the test data from DESERVE, a Technology Strategy Board (TSB) funded project in the UK [46].

Table 3.3. ZEBRA Z5C battery data-sheet [51, 52]

Type	Zebra Z5C
Capacity (Ah)	66
Rated energy (kWh)	17.8
Open circuit voltage (V)	278.6
Max. regen voltage (V)	335
Max. charging voltage (V)	308
Min. voltage (V)	186
Max. discharge current (A)	224
Weight (kg)	195
Specific energy (Wh/kg)	91.2
Specific power (W/kg)	164
Peak power (kW)	32
Thermal Loss (W)	<120
Cooling	Air
Battery internal temperature (°C)	270 to 350
Ambient temperature (°C)	-40 to +70
Dimensions (W x L x H) (mm)	533 x 833 x 300
Number of cells per battery	216
Cell configuration	2 parallel strings of 108 series cells

Fig. 3.5. ZEBRA Z5C Traction battery [51].

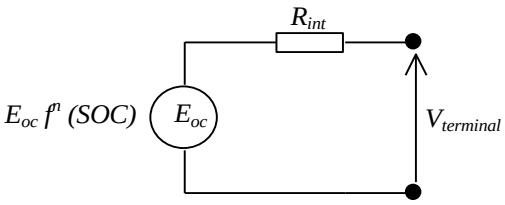

Fig. 3.6. Equivalent circuit of a ZEBRA Z5C battery.

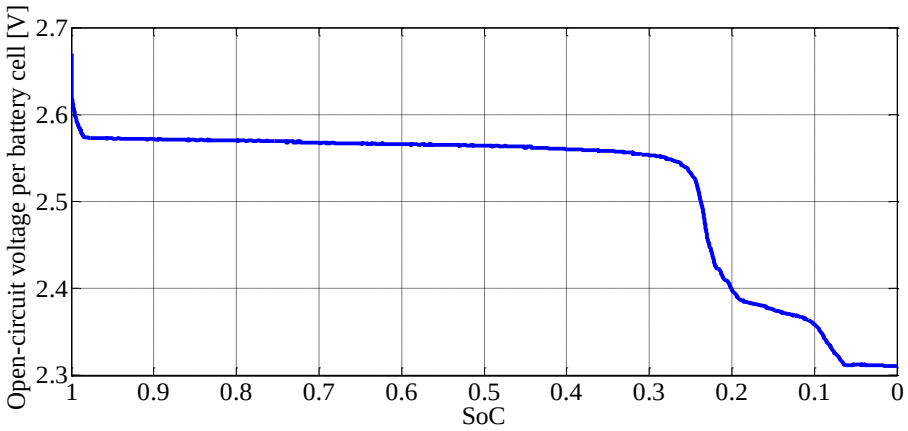

Fig. 3.7. Open-circuit EMF per battery cell.

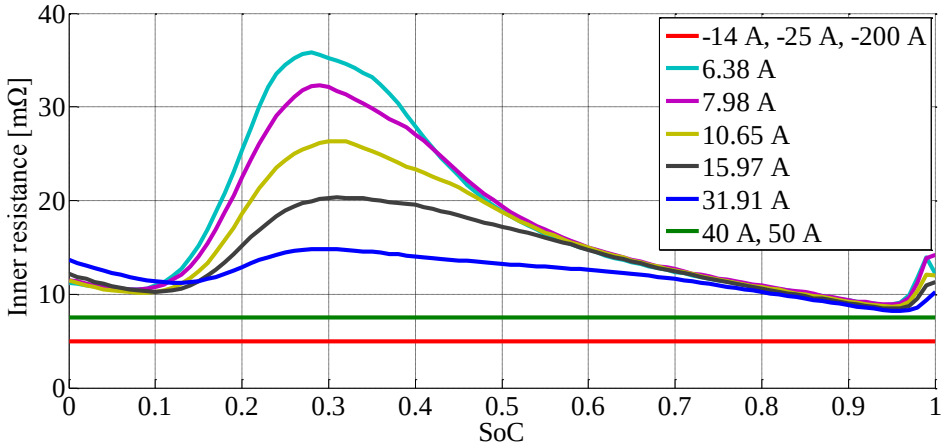

Fig. 3.8. Internal resistance per battery cell.

According to the different schedules of the port terminals, the RTG energy storage systems are designed for 4-hour and 16-hour operation. Compared to 16-hour operation RTGCs, the 4-hour operation RTGC requires lower battery cost and is suitable for short period loading and unloading, but regular battery charging is needed. Both the two cases require the same peak power rating of 460 kW, however, the total energy demand are 82 kWh and 326 kWh respectively, which results in an energy/power ratio of 0.18 and 0.7 respectively. The energy/power ratio is a key determinant of energy source selection. Generally, batteries, with high power density but low energy density, have higher energy/power ratio compared to the peak power buffers. The energy/power ratio of the ZEBRA Z5C battery is around 0.56, which indicates the energy capacity of 4-hour operation crane will be oversized to meet the peak power requirement.

For short period operation, i.e., 4-hour operation, the peak power demand dominates the battery sizing. Since the battery peak power is tested by discharging the battery at the high test current, the data of the battery specific power on the datasheet can be used for battery sizing. In addition, the peak power condition leads to the lowest battery voltage level and highest battery current level. Since the battery is directly connected to the DC-link, the battery number is determined by:

$$N_{b\_s} = max\left(\frac{V_{dc\_\max}}{V_{breg\_\max}}, \frac{V_{dc\_\min}}{V_{bdis\_\min}}\right) \tag{3.10}$$

$$N_b = \frac{P_{pk\_dem}}{P_{b\_sp}} \tag{3.11}$$

$$N_{b\_p} = \frac{N_b}{N_{b\_s}} \tag{3.12}$$

where N_{b_s} and N_{b_p} are the numbers of series-connected battery cells and parallel-connected strings, $V_{dc\_\max}$ and $V_{dc\_\min}$ are the upper and bottom bounds of DC-link voltage, $V_{breg\_\max}$ and $V_{bdis\_\min}$ are the maximum regenerating and minimum operating voltages per cell, N_b is the total number of battery cells, P_{pk_dem} is the peak power demand, and P_{b_sp} is the battery power capacity per cell.

Since the design requirements and constraints have been considered by Equation (3.10)-(3.12), the detailed battery model is utilized to slightly adjust the number of battery cells and confirm the battery real-time performance within the physical limits:

$$\left|i_{bdis}(t)\right| \le \left|i_{bdis\_\max}\right| \tag{3.13}$$

$$\left|i_{bch}(t)\right| \le \left|i_{bch\_\max}\right| \tag{3.14}$$

$$V_{bdis\_\min} \le V_b(t) \le V_{breg\_\max} \tag{3.15}$$

$$P_{breg\_pk} \le P_b(t) \le P_{bdis\_pk} \tag{3.16}$$

where $i_{bch}(t)$ and $i_{bdis}(t)$ are the real-time charging and discharging currents, $i_{bch\_\max}$ and $i_{bdis\_\max}$ are the maximum limits of battery charging and discharging currents, $V_b(t)$ is the real-time battery voltage, $P_b(t)$ is the real-time battery power, P_{breg_pk} and P_{bds_pk} are maximum limits of regenerating and discharging peak power. Note, both regenerating power and charging current are expressed with negative value.

However, for long period operation, i.e., 16-hour operation, the battery sizing with numerical equations is not as easy and accurate as the short period operation, because the energy demand becomes the dominant factor. Since the battery specific energy published by the manufacture is obtained under the conditions of fixed discharging current, it cannot be directly used to size the battery system for dynamic load applications. Therefore, the battery sizing procedure is as illustrated in Fig. 3.9. The series number of batteries is still determined by the DC-link voltage, but the total number of batteries is initially estimated by dividing the total energy demand by the energy capability per cell from the data-sheet. Employing the detailed battery model, real-time iteration of the battery number is applied in maximum load condition until the energy demand is satisfied. In this way, the accurate number of batteries is achieved. At the same time, the actual specific energy is obtained, which can be also used for the sizing of battery-supercapacitor hybrid energy storage. Due to the battery loss, the actual specific energy under maximum load is only 61.2 Wh/kg, which is significantly different from the value of 91.2 on the data-sheet.

The comparison between the ZEBRA Z5C battery package and a 700 kW Detroit Diesel/MTU diesel ICE GenSet is illustrated in Table 3.4. The 700 kW diesel GenSet is modelled as a fuel consumption map based on the specification sheet [53]. It can be observed that turning ICE GenSet into battery package improves the energy storage system in terms of mass, volume and efficiency. Even for long period operation, the total mass of the energy storage device is reduced by 59% and the total volume is decreased by 95%. According to the diesel-electric conversion coefficient of 3.47 (kWh/l) obtained from Chinese Government published battery charging test data [31], the battery energy consumption for 16-hours of operation is equivalent to 122.13 litres of diesel consumption. Therefore, the system efficiency is significantly increased resulting in an approximate diesel saving of 71.5%. The energy device cost comparison is not studied here and is subject of future research

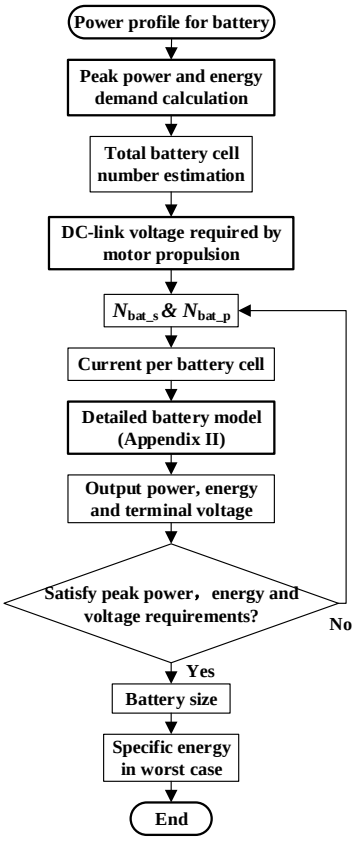

Fig. 3.9. Pure battery storage sizing procedure flow chart for long period operation.

Table 3.4. GenSet and Battery Energy Storage.

	Diesel GenSet		ZEBRA batteries	
	4 hours	16 hours	4 hours	16 hours
Total mass[1] (tonne)	12.8	12.8	2.925	5.265
Total volume[1] (m^3)	74.1	74.1	2	3.6
Electrical energy (kWh)	-	-	81.6	326.2
Consumption (litres)	107.1	428.5	31.44[2]	122.13[2]
Efficiency[2] (%)	21.9	21.9	75.6	77

[1] The total mass and volume of diesel GenSet include the generator set with largest alternator option, enclosure, silencer, and tank.

[2] Based on the diesel-electric conversion coefficient of 3.47 (kWh/l) [31].

However, although the electro-chemical battery satisfies the power and energy requirements, its peak transient current is large, i.e., 1000A in this case, as illustrated in Fig. 3.10. Such a high peak transient current leads to negative effects for batteries. Firstly, according to Fig. 3.11, large battery charge and discharge current gives rise to higher battery energy loss. In this case study, 97.48 kWh energy loss is caused by the battery internal resistance for 16 hour RTGC operation, which gives rise to a low battery cycle efficiency of 77%. In addition, according to Fig. 3.7, there is about a 14% open-circuit terminal voltage variation due to the reduction of battery state-of-charge (SoC). For a 550 Volts rated battery package, there will also be over 100V voltage-drop due to the peak discharging current during acceleration and 30V peaks due to the peak charging current in regenerative braking. Consequently, the battery output voltage variation, as shown in Fig. 3.12, is between 420V and 580V, which has implications for the control and design of the electric machines and power electronic converters. Moreover, the high cyclic operation with large charge and discharge current reduce the battery life, leading to high maintenance cost [51]. Furthermore, for a 4 hour crane operation, since the peak power demand dominates the battery sizing, an oversized battery package is necessary to compensate for the low power density of batteries. In order to reduce the battery current, efficiency and DC link voltage variation, a high power density and effective peak power buffer, such as a supercapacitor or flywheel can be integrated in a hybrid energy source combination.

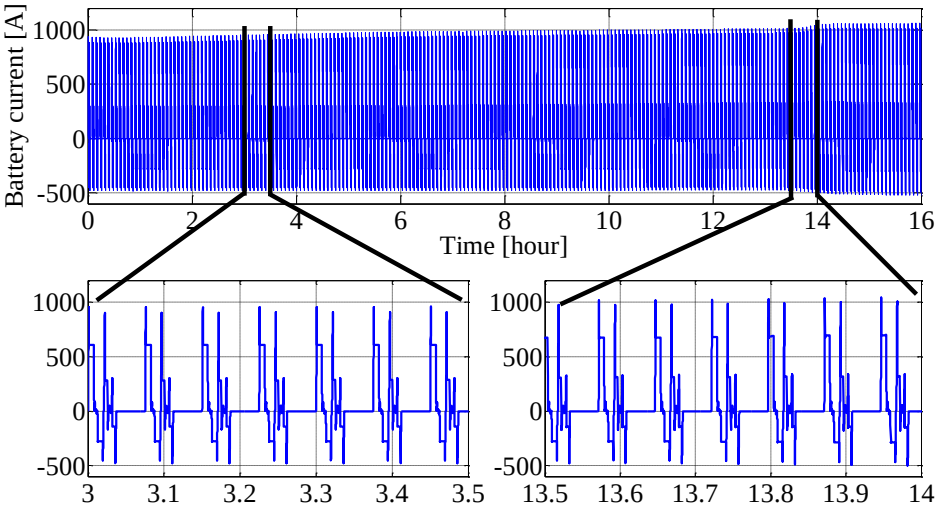

Fig. 3.10. Battery current for pure battery energy storage.

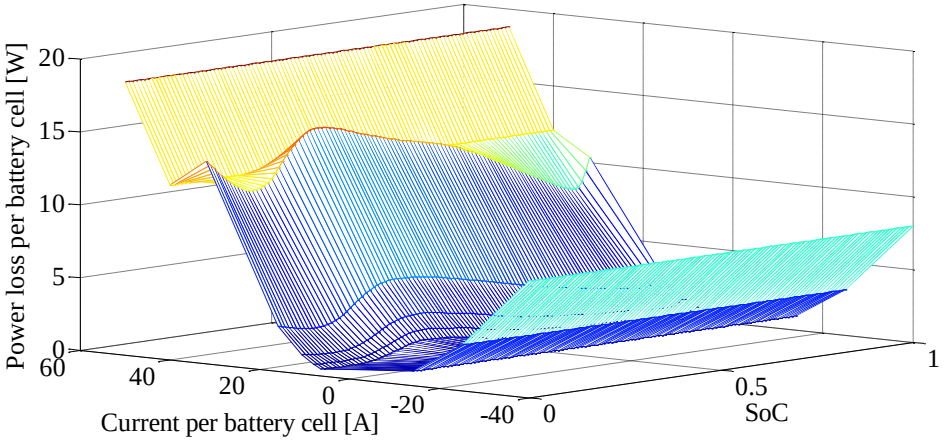

Fig. 3.11. Power losses per battery cell.

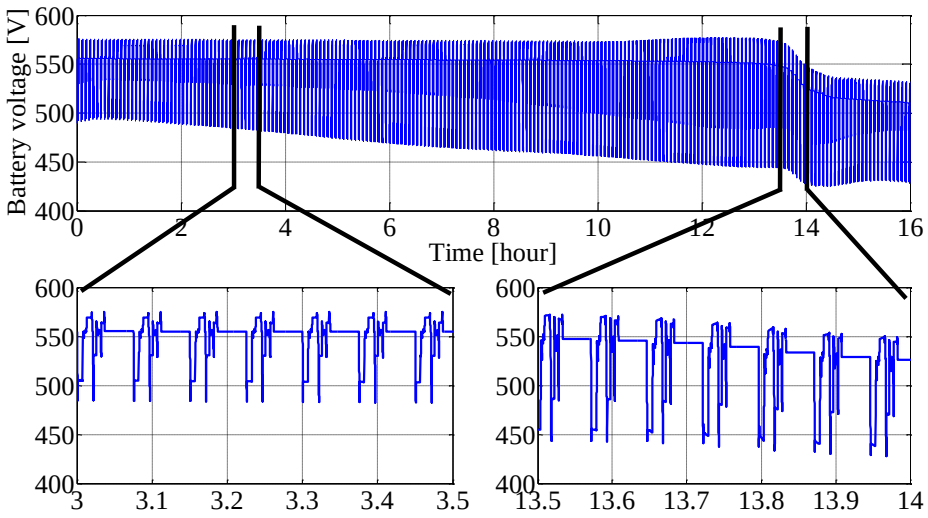

Fig. 3.12. Battery voltage for pure battery energy storage.

3.6 Supercapacitor Model

Supercapacitors have been widely used for their high power density, long service life, quick charging and discharging and lower maintenance problems than electro-chemical batteries [23, 54]. Supercapacitors are able to operate under high power charging and discharging circumstances, such as load lifted up and down, gantry acceleration and deceleration. In such cases the supercapacitor service life will not be influenced by the high charging and discharging currents. However, the supercapacitor is a low energy dense device. The supercapacitor model can be simplified as a loss-less capacitor where the effective operational stored energy is expressed as:

$$E_{SC} = \frac{1}{2} C(v,\theta)\left(V_{MAX}{}^2 - V_{MIN}{}^2\right) \tag{3.17}$$

where $C(v, \theta)$ is the supercapacitor capacitance which is a function of cell voltage and temperature (as discussed later), V_{MAX} and V_{MIN} are the maximum and minimum operational voltage levels.

Similarly, a flywheel is an energy storage device with high power density but low energy density. In the flywheel system, energy is stored in the flywheel inertial elements and an integral motor/generator is interfaced to the electrical system during charging and discharging. In charging mode, the motor speed up the flywheel to store the energy as kinetic energy. In discharging mode, the flywheel is slowed down to convert kinetic energy to electrical energy through the generator. Flywheels are able to both source and absorb large amounts of power at high cycle rates demanded, for example, by the crane application, with long cycle life and high energy efficiency [32]. A flywheel model is simplified as an additional inertia added to the rotor of an electric machine, so the effective operational stored energy can be expressed as:

$$E_w = \frac{1}{2} J_w \left(\omega_{w\max}{}^2 - \omega_{w\min}{}^2\right) \tag{3.18}$$

where J_w is the combined machine and flywheel inertia, and $\omega_{w\max}$ and $\omega_{w\min}$ are the maximum and minimum operational rotating speeds of the flywheel respectively.

Due to its low energy/power ratio, if the supercapacitor or flywheel is employed alone as the energy storage device, its peak power will be oversized, resulting in a large and heavy unit to meet the energy requirement. However, in the hybrid power-train system, giving full play to their own superiority, the maximum power demanded from the battery will be reduced and more energy would be effectively recovered from regenerative braking by the peak power buffer. Since the operation principle and characteristics of supercapacitor and flywheel are similar, only the battery-supercapacitor hybrid energy system is investigated in this case study.

The classical capacitor model is shown in Fig. 3.13, which consists of the constant capacitance, an equivalent series resistance (ESR) and an equivalent parallel resistance (EPR). The commercial 48 Volt, 165 F Maxwell supercapacitor unit shown in Fig. 3.14, is considered for this case study. Since the capacitance of a supercapacitor is strongly dependent on the terminal voltage, a SC model is developed based on the classical capacitor model structure of Fig. 3.13, whereby an additional series resistance and absorption capacitance are added and a non-linear model for the main capacitance is modelled via a lookup table, as shown in Fig. 3.15. The variable non-linear capacitance function is determined from test data, as illustrated in Fig. 3.16. In addition, to understand the SC operational temperature caused by internal power dissipation in the resistive elements, the SC thermal model is included. The SC model is validated by test data from the DESERVE project [46].

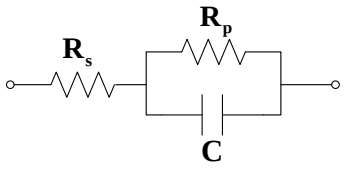

Fig. 3.13. Classical capacitor model [56].

Fig. 3.14. 48 Volt, 165 F Maxwell supercapacitor unit [52].

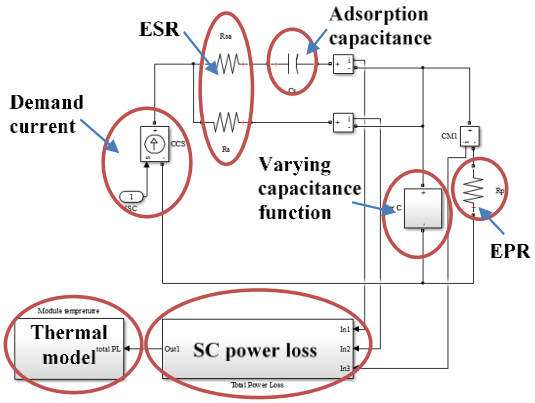

Fig. 3.15. Maxwell SC model in Matlab/Simulink [52].

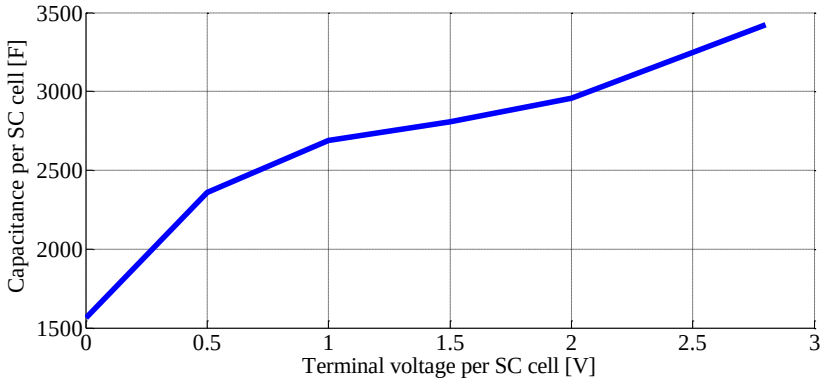

Fig. 3.16. SC variable non-linear capacitance function from test [46].

3.7 Hybrid Energy Storage System Design

3.7.1 Control strategy

To implement the battery-supercapacitor hybrid crane operation, a power-train system model with a DC/DC converter installed in series with SC and then in conjunction with battery is designed, as illustrated in Fig. 3.17. As discussed in Section 3.5, the battery lifetime and efficiency can be improved if the peak transient charging and discharging current is mitigated by supercapacitors. In addition, since the batteries and supercapacitors are characterized by different operating voltages, the DC/DC converter is controlled to match the output voltages of the batteries and supercapacitor and thus manage power flow. The block diagram of the control system is shown in Fig. 3.18.

For the battery-SC hybrid system control, the numerically efficient filter-based strategy is utilized, although this control strategy is not suitable for HEV applications. Due to the uncertainty in the HEV driving cycle, the cut-off frequency may need to be adjusted for different load demand and hence filter-based method may introduce large phase shift that degrades performance of HEV applications [57]. However, RTGC is a special vehicular application which has special operation characteristic. According to Fig. 3.4, there is obvious frequency difference between the high frequency peaks and the fundamental signal, hence the frequency ratio is small enough to result in a reasonable phase shift. In addition, the RTGC driving cycles are more regulated than HEV, so the cut-off frequency only requires slight adjustment. Both the container and RTGC have to move in specified order, velocity and distance, hence the RTGC driving cycle is much more foreseeable. Therefore, although the filter-based method is dependent on heuristics and empiric experience, it works well for the RTGC application.

The control system realizes the double closed loop control of the battery current and the duty ratio of DC/DC converter. The PI controller, in the outer loop, is used to control the battery current according to the difference between the desired SC voltage and feedback SC voltage. By controlling the SC voltage, the power-train system power flow is controlled. After the peak power supply, the highly discharged SC stops discharging and then is

charged by the breaking regenerating energy or the energy from the battery to prepare for the next peak power demand. Therefore, the SC keeps its charge sustenance. Besides, a low-pass filter is designed to smoothen battery current and a current limiter is followed to achieve reasonable current magnitude. Therefore, the transient demands are supplied by supercapacitor. In the inner loop, SC demand current is used as the input and a fast and stable PI controller is designed to control the duty ratio for DC/DC converter. Based on the proposed control strategy, the control system is built for the hybrid RTGCs.

3.7.2 Crane operation for short period

According to the previous study, for 4-hour crane operation, the peak power requirement dominates the energy storage design and hence the energy capacity is oversized for pure battery operation. Due to its high power density capability, the supercapacitor can be utilized to cut off the high frequency peaks and reduce the volume and mass of the energy storage. The HESS sizing is still determined by the power demand of hoist machine, which is illustrated in Fig. 3.19. The battery sizing in the battery-SC hybrid configuration for short period crane operation is similar to the pure battery case. The series number of battery cells is determined by the DC-link voltage specification, in Equation (3.10)-(3.12). However, since the transient power peaks are supplied by the SC, the total battery size is determined by the maximum value of P_1 in Fig. 3.19 and 4-hour energy requirement E_s.

$$N_{b\_h} = Max\left(\frac{P_1}{P_{b\_sp}}, \frac{E_s}{E_{b\_sp}}\right) \tag{3.19}$$

where N_{b_h} is the number of battery cells in the HESS and E_{b_sp} is the actual value of battery energy capacity per cell obtained by the pure battery system design in Section 3.5.

Theoretically, SC is designed to satisfy the transient power of P_2. However, since the SC has batter transient performance than battery, SC will quickly start to supply. Therefore, in this study, the SC is sized to satisfy the peak power demand and the energy of E_1 in Fig.3.19. The SC specific energy shown on the datasheet cannot be directly used for sizing. As mentioned in Section V, the capacitance of a supercapacitor is strongly dependent on the

terminal voltage. The non-linear capacitance function illustrated in Fig. 3.16 is employed to obtain the usable energy capacity and hence the SC actual specific energy. The HESS sizing procedure, which is combined with the battery sizing procedure is illustrated in Fig. 3.20. Both detailed battery and SC models are utilized and real-time iteration is implemented to satisfy the system peak power and energy demand. The SC number is adjusted to satisfy the required efficiency of the HESS. The HESS sizing results for 4-hour crane operation is presented in Table 3.5. Figs. 3.21-3.24 show the control results of the short period operation hybrid RTGC for one typical load cycle. An example crane load cycle is illustrated in Fig. 3.21 and the corresponding duty ratio of the DC/DC converter is controlled to boost the supercapacitor voltage to match the battery voltage, as illustrated in Figs. 3.21 and 3.22. Fig. 3.24 (a) shows the fast response speed and good control accuracy of SC current. In addition, the supercapacitor is controlled to either provide high transient power in hoist-up operation or capture regenerative power in hoist-down operation, as shown in Fig. 3.24 (b), which reduces the peak power stress on battery.

Compared to the traditional diesel GenSet and pure battery energy storage, the hybrid energy source system results in a more compact and lightweight solution. In addition, according to Fig. 3.24 (b), the transient power peaks of the load power are filtered and flow through SCs, so that the battery operates as the main energy source with lower current fluctuation. Therefore, the battery stress can be significantly alleviated, which improves battery lifetime.

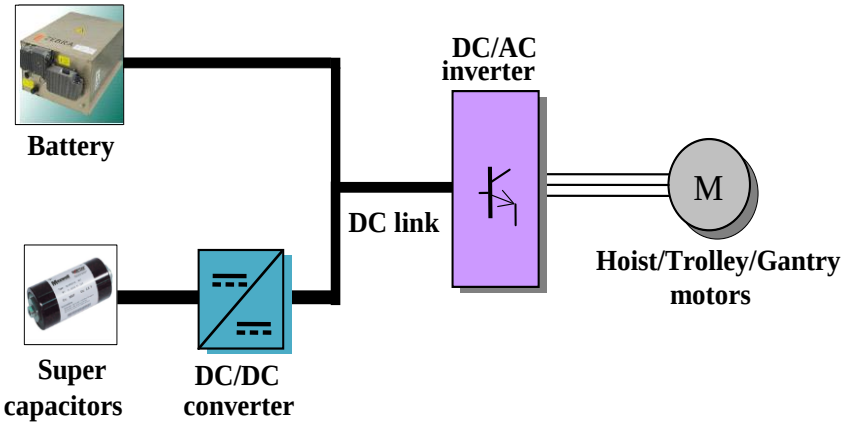

Fig. 3.17. Battery-supercapacitor hybrid RTGC power-train.

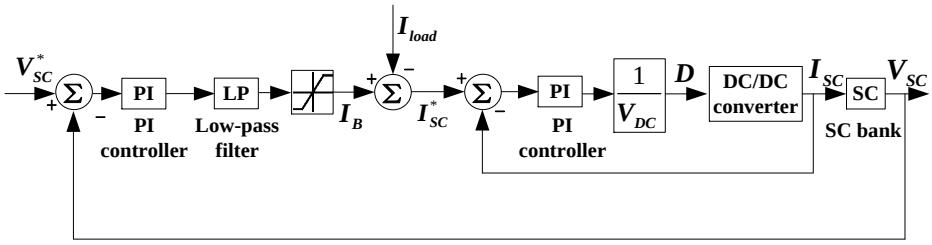

Fig. 3.18. Hybrid RTGC control system.

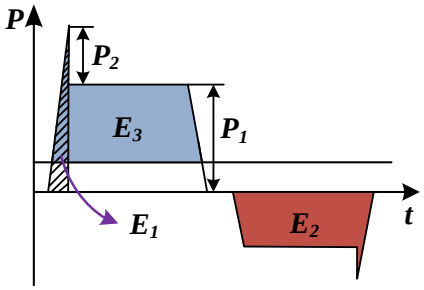

Fig. 3.19. Classical Power and energy demand of hoist machine.

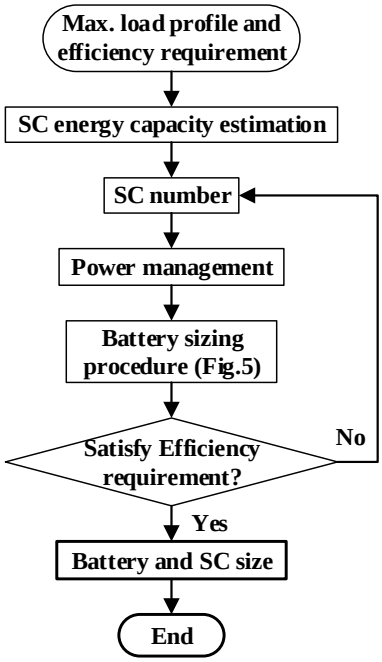

Fig. 3.20. Battery-SC HESS sizing procedure.

Table 3.5. Battery-supercapacitor Hybrid Theoretical Specification.

	Specific power (W/kg)	Specific energy (Wh/kg)	Energy/ power (h)	Mass (tonnes)	Volume (m3)
ZEBRA batteries	164	91.2	0.56	1.755	1.2
Supercapacitors	3814	3.8	0.001	0.142	0.13
Hybrid system	436.5	84.5	0.19	1.9	1.33

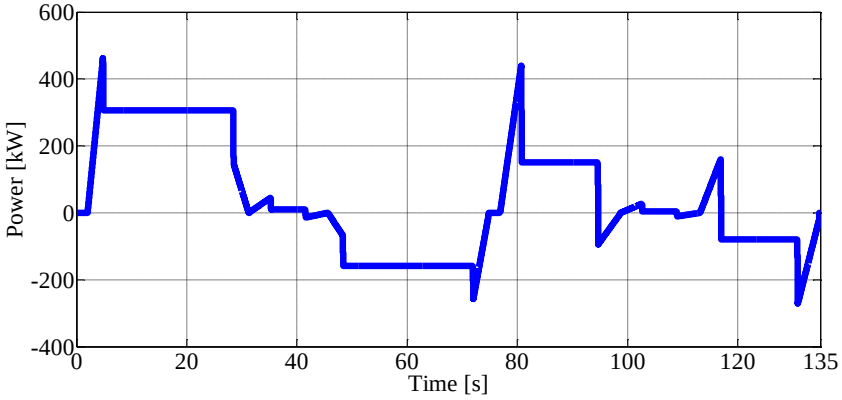

Fig. 3.21. Example load cycle.

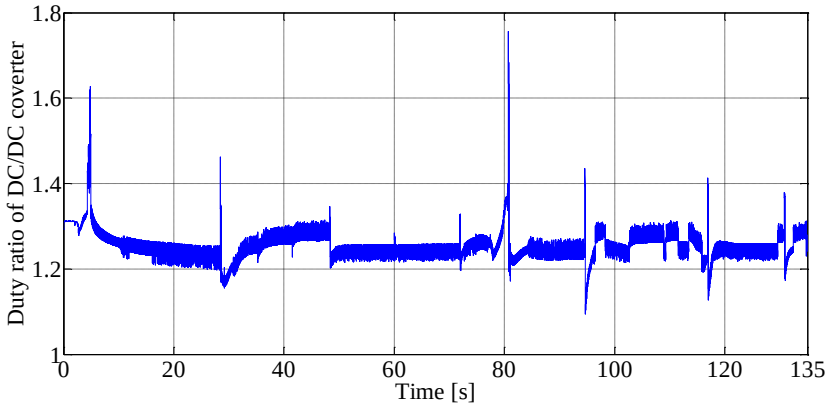

Fig. 3.22. Duty ratio of DC/DC converter.

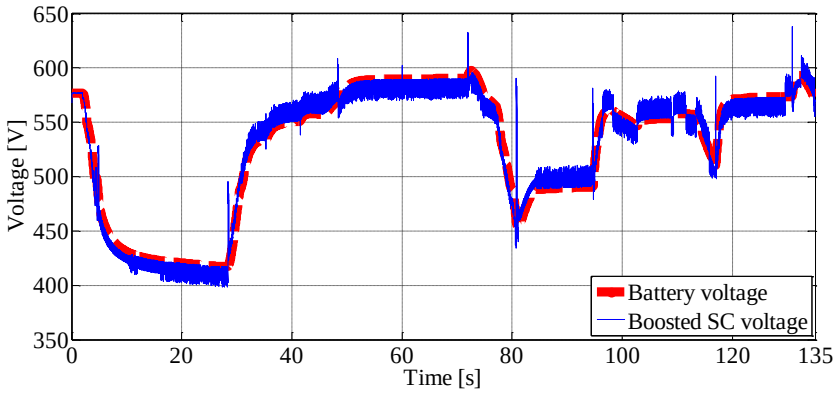

Fig. 3.23. Battery voltage and boosted SC voltage.

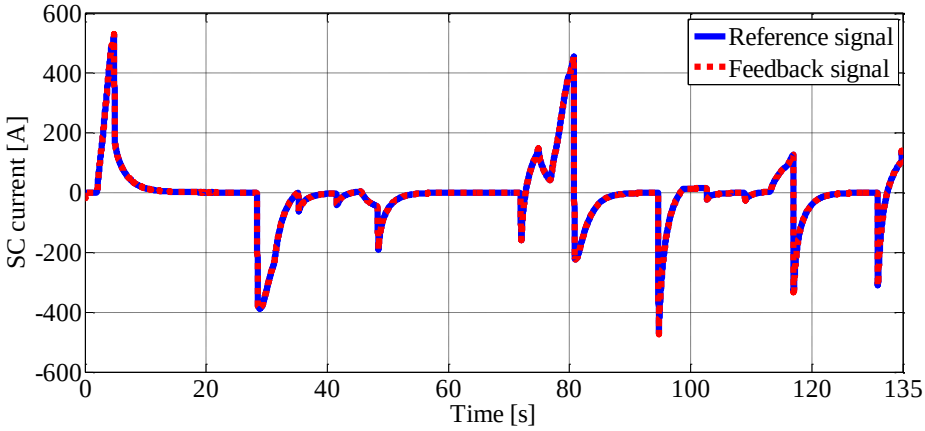

(a) SC current control results.

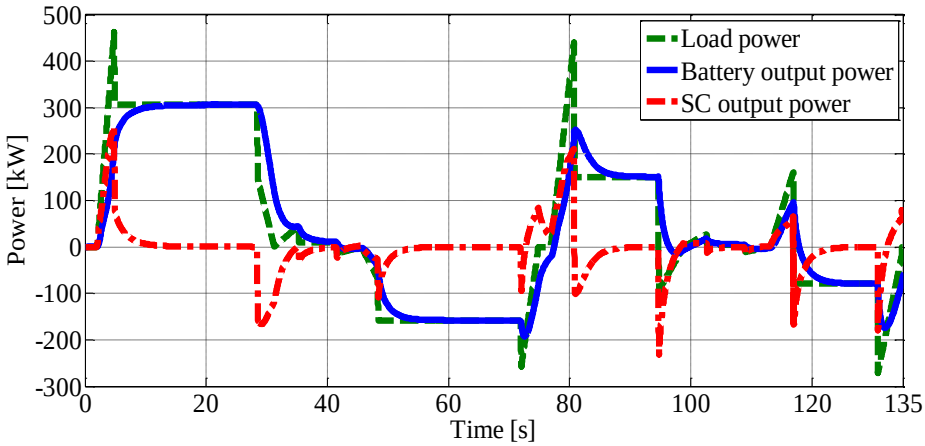

(b) Power management results.

Fig. 3.24. Hybrid energy storage results.

3.7.3 Crane operation for long period

For 16-hour crane operation, the total energy demand dominates the energy storage design. For pure battery configuration, the specification of the large battery package satisfies both the peak power and energy demands. However, as discussed previously, the large peak transient current adversely affects the batteries. To overcome the negative effects, supercapaciters are still suitable candidates to be integrated into the energy storage system. Since the battery energy/power ratio is already lower than the desired energy/power ratio, the supercapacitor is mainly used to improve the system efficiency rather than increase the system power density. In this section, the previously developed power-train system model is utilized to investigate the hybrid crane energy system design for long period.

The level of the size of the SC results in different level of HESS efficiency. If it is just required to cut off the transient power peaks, the SC usable energy capacity is designed to satisfy the value of E_1 in Fig. 3.19, which is same as the HESS design for short period crane operation. In this case, due to their energy limit, the supercapacitor modules operate as a power buffer to only supply or receive the transient power peaks, which significantly reduces the battery peak charging and discharging current. However, since the battery package is still the main power and energy source, considering the loss of the SC and DC/DC converter, the system efficiency is slightly improved compared to the pure battery power/energy source. With increasing supercapacitor modules, if the SC usable energy capacity satisfies the value of E_2, the supercapacitor modules will not only share much more power supply, but also receive all the regenerative power. Since supercapacitors capture the braking energy more efficiently than the electro-chemical batteries, the system efficiency is moved up to a higher level. As the number of supercapacitor modules is further increased, when the SC usable energy capacity achieves the value of E_3, the battery pack only needs to continuously supply the average current to the power-train, so that the battery power loss is minimized, according to Fig. 3.11.

Based on above analysis, the design procedure illustrated in Fig. 3.20 is used for battery-SC HESS sizing. Based on the maximum load profile and the energy storage system efficiency requirement, the SC usable energy capacity is estimated and the total number of

SC cells is determined. The SC usable energy capacity and the power management employed decide the power and energy share of battery package. Then the battery number is achieved by the procedure shown in Fig. 3.9 and SC number is adjusted to satisfy the efficiency requirement. For long period crane operation, the battery is sized to satisfy the total energy requirement. With continuously increasing the number of supercapacitor modules, the HESS efficiency is improved as illustrated in Fig. 3.25. It can be noticed that at the beginning of the third step, the battery current is close to the average current demand, since the supercapacitors are large enough to release and receive the main charging and discharging currents. However, if the supercapacitor size is further increased, the battery current will not be lower than the average demand value, and hence the battery pack size will not be smaller for any further increase in SC number. The efficiency increasing steps is as a result of the size and total usable energy capacity of SC. In addition, as the battery efficiency is improving with the increase of SC size, the battery package size can be reduced, as illustrated in Fig. 3.26.

As a high temperature Sodium-Nickel-Chloride battery, the ZEBRA battery is controlled to operate with its internal temperature within a range from 250 ºC to 350 ºC by the battery thermal management [46]. However, since the SC modules are using force ventilated cooling, their thermal behavior is modelled with an assumed ambient temperature of 25 ºC, as shown in Fig. 3.27. By magnifying the temperature curve, it can be noticed that the SC module temperatures vary with cyclic loading. During supercapacitor charging and discharging operation, power loss is dissipated in the supercapacitor cell resulting in an increase in the cell temperature. In idle condition, the SC temperature is decreased. For the whole 16-hour crane operation, the SC modules are able to operate with the minimum and maximum temperature limits of 0 and 55 ºC [46].

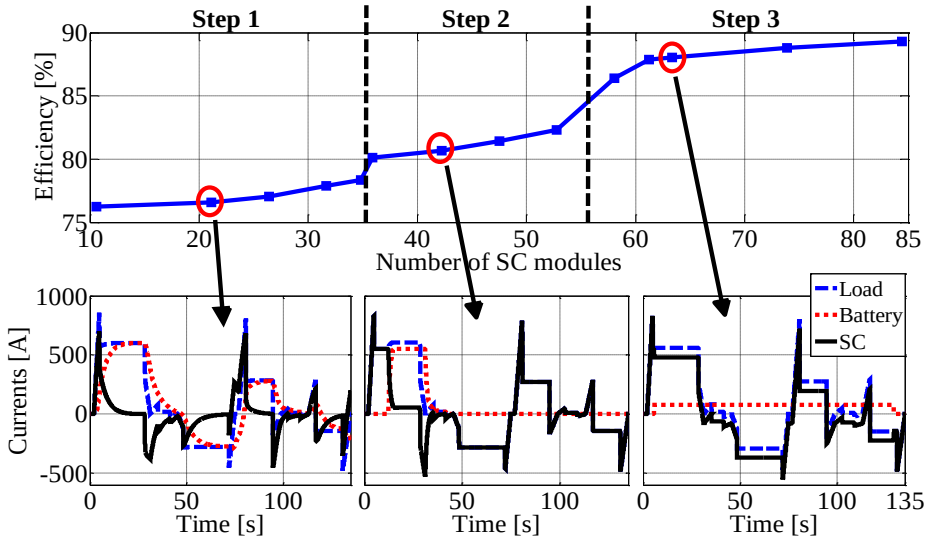

Fig. 3.25. Impact of the number of SC modules on system efficiency.

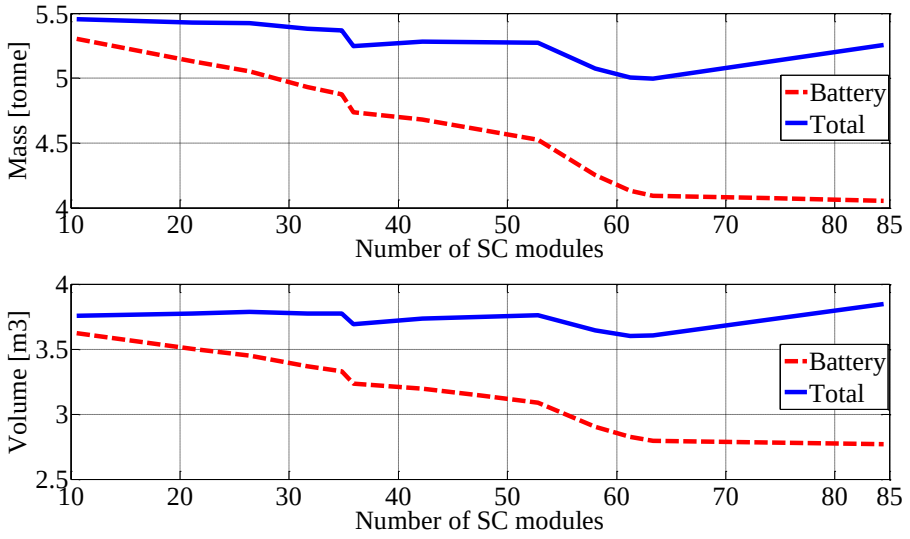

Fig. 3.26. Impact of the number of SC modules on system mass and volume.

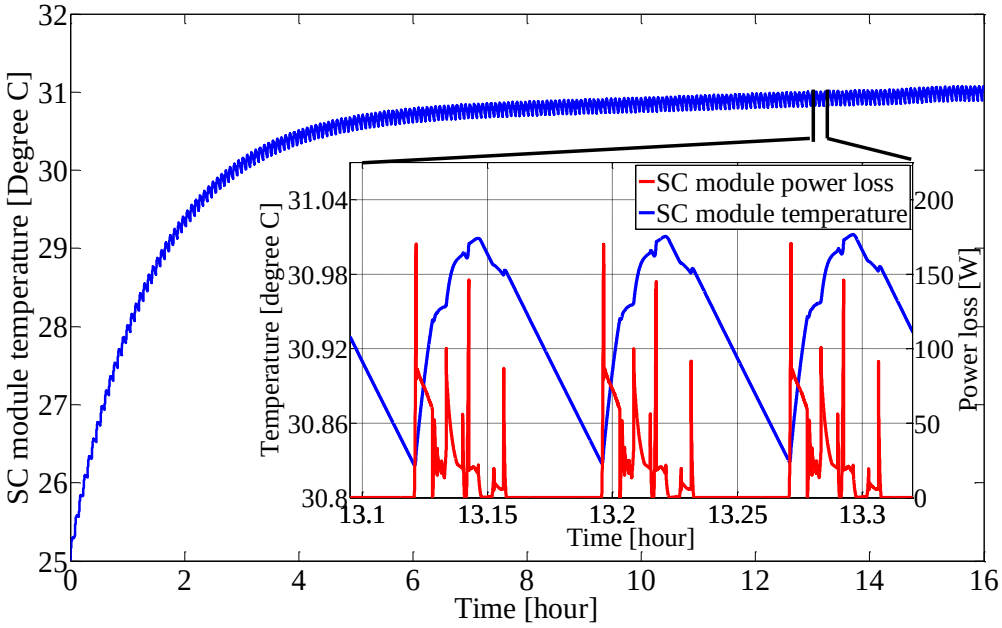

Fig. 3.27. Simulated SC module temperature with cyclic loading.

3.8 Machine Design Consideration

3.8.1 Torque-speed Characteristic of Machines

Due to its low cost, robust, simple structure, mature manufacture and control technique [9], induction machines are always employed for RTGC. In this particular application case study, there is one hoist machine, two trolley machines and four gantry machines. The torque-speed operating points of each machine are illustrated in Fig 3.28. It can be noted that the hoist machine torque-speed characteristic in Fig. 3.28 (a) is a traction characteristic, which requires high torque over a low speed region for on-load operation and a low torque at high speed for no-load operation. According to operating torque-speed points, the hoist machine can be designed as a traction machine with 2:1 constant power speed ratio. Comparing to the hoist machine, the trolley and gantry machines do not requires good field weakening capability and hence traditional induction machines can be utilized for those two types of machines.

3.8.2 Hoist Machine Design Considerations

There are a few considerations to be taken into account during the hoist machine design:

(1) According to torque and power requirements, the hoist machine should be designed to have 3290 Nm for full-load operation and 330 kW at maximum speed operation.
(2) The corner speed of 961 rpm, can be set to be the rated speed of the machine, which suggests the machine to have 6 poles referenced to a 50 Hz base frequency.
(3) Considering the supply voltage constraint, the machine will be designed with certain field weakening capability. In this case, a constant power speed ratio of 2 is required.
(4) In the conventional fixed voltage, fixed frequency induction machine design procedure; in order to meet the start-up requirement, including limiting starting current and maximizing starting torque, narrow and deep rotor slots are used, which affect the efficiency and reduce the power factor in low speed operation. With inverter fed

systems, the starting torque can be controlled and hence the starting current can be replaced by rated current [59]. So it is more suitable to use wide and shallow rotor slots for the inverter driven IM.

(5) In general, due to the high order harmonics caused by the PWM power electronic inverter drive switching scheme, the machine may experience efficiency decrease and losses, thus temperature, noise and vibration levels may increase [59, 60]. To depress the high order harmonics, the basic considerations are: (i) increasing the leakage reactance of stator and rotor; (ii) using short pitch winding; (iii) choosing proper combination of rotor/stator slot number [59, 60].

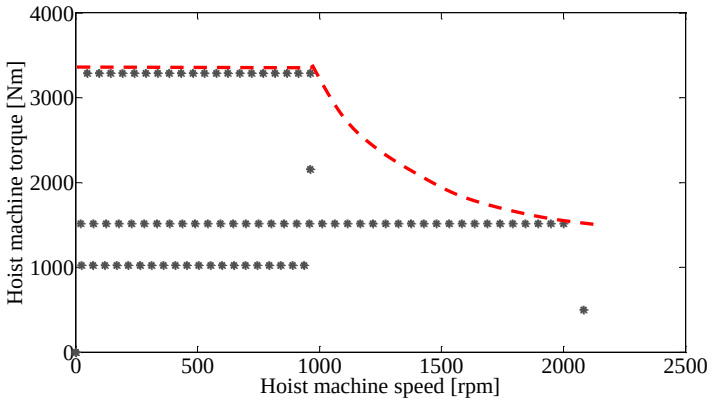

(a) Hoist machine.

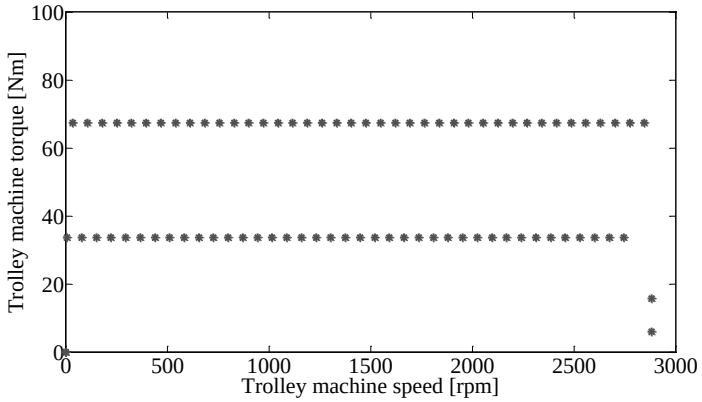

(b) Trolley machine.

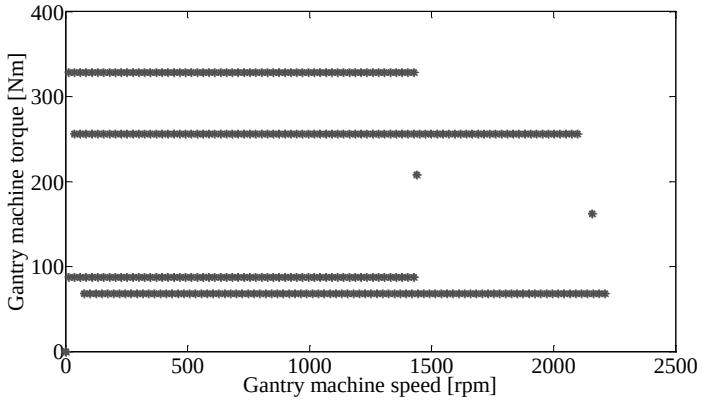

(c) Gantry machine.

Fig. 3.28. Torque versus speed characteristics for RTGC machine.

3.9 Conclusions

This Chapter investigates the feasibility of energy storage systems for implementation in hybrid energy source systems (HESS) providing the power-train of an electrified rubber tyred gantry crane (RTGC). Based on the dynamic analysis of a typical RTGC, the energy requirement and power rating of the crane power-train system are specified. Comparing with the traditional diesel ICE crane application, the electric crane, especially the battery-supercapacitor hybrid crane, shows a great potential for regenerative energy recovery, which is associated to a reduction in fuel costs and emissions.

For system analysis, a complete RTGC power-train Matlab/Simulink model is established. Both the battery and supercapacitor model are developed based on cell experimental dynamic assessments and validated by test data from the DESERVE project. In addition, to assess the module thermal performance, a thermal model for the supercapacitor is included. A filter-based control strategy, which is simple implementation and numerically efficient, is proposed to allow the battery to operate as the main energy source with constant or low fluctuation of current and the supercapacitor to capture and release peak charge and discharge currents.

The battery-supercapacitor hybrid energy storage systems are designed for both short and long period operation, which results in effective energy conversion, and hence lower emissions, together with a compact construction solution. The procedures for design of battery alone and battery-supercapacitor hybrid energy source systems are shown to be different and independent of the optimization method chosen. These procedures are developed in the Chapter. Further, the HESS systems are graphically optimized and proposed for RTGC applications. In addition, the system transient peak power demand of 0-460kW in 2 seconds, equates to a constant torque loading on the system prime mover, the ICE. This usually necessitates an over-rating of the prime-mover by up to 50%. Consequently, the ICE is over-sized for the other lower torque/power operations, resulting in non-optimum operation in terms of fuel consumption and emissions. The improvement in system transient response afforded by the HESS thus results in a significant reduction in energy source mass and volume.

The study results reveal the benefits of hybrid energy sources, will have guiding significance for the design and improvement of port crane hybrid energy source systems and will thus impact on marine goods transportation in terms of energy consumption and emissions.

Chapter 4

Modelling and Design of Induction Machines for Traction Applications

4.1 Introduction

As discussed in previous Chapters, traction torque-speed characteristics, i.e., high torque at low speed and power at high speed, are typical requirements in many electrical drive system applications. The constant power speed ratio (CPSR), or high speed to full-load base speed ratio, varies with application, for example, the ratio may be 2:1 for lift machinery as discussed in [61] and Chapter 3, 2:1 for some home appliances [62], 3:1 for computer numeric controlled machine tools [63] and more recently, 2 to 3:1 for electric and hybrid-electric vehicles [64].

The induction machine (IM) is a mature technology and a suitable candidate for traction applications. IMs designed for traction applications are supplied via power electronic (PE) converters, rather than being connected direct-on-line (DOL) to a fixed voltage, fixed frequency (FVFF) power grid. DOL connected IMs are currently the main machine technology used in industry with a figure of 80% typically quoted [65]. However, PE driven IMs, in variable torque-speed drive applications, are becoming more popular since they offer a wider (rectangular) torque-speed characteristic envelope from zero to full-load base speed, improved system dynamics (especially when vector controlled) and potential for higher system energy conversion efficiency. Traction applications extend the torque-speed characteristic further towards a maximum speed by field-weakening [66, 67], as illustrated in Fig. 4.1 showing a typical IM characteristic and an ideal traction constant power profile.

According to [67], extending the constant power region will significantly lower the machine rating. However, with the variation of the supply frequency and machine air-gap flux, the IM equivalent circuit parameters vary so that the machine cannot maintain constant power in the entire high-speed range. Therefore, an induction machine design procedure is required to achieve a traction torque-speed characteristic. To design a traction machine while considering the traction system design, especially within the voltage and current constraints imposed by the PE converter, it is necessary to identify the key design parameters. It was discussed in Chapter 2 that for brushless permanent magnet (PM) machines, the back-EMF coefficient, k_o, primarily impacts on the machine maximum torque from zero to base speed. In the field weakening region, the ratio between k_o and the *d*-axis inductance-current product, L_dI_s, becomes the main design factor to ensure a onstant power range [68]. Similarly, for switch reluctance (SR) machines, extended-speed operation can be achieved by reducing the number of turns per phase from the optimized for maximum torque/Ampere at base speed, with the compromise being a reduction of torque/Ampere below base speed [69], which is effectively the same procedure as for brushless permanent magnet machines. However, existing studies on traction IM design rely on optimization algorithms or iterative calculation programs. Therefore, the key parameters influencing design are not identified. This Chapter addresses this deficiency with consideration to the traction system design.

To identify the key parameters required to design IMs with traction torque-speed characteristics, an induction machine model is developed. Based on model analysis results, an induction machine design procedure is proposed, which offers comprehensive performance improvements in terms of efficiency, power factor and field weakening capability. The machine design parameters are normalized in per unit form and hence the proposed design strategy is applicable across different ratings. As an example, a 2.2 kW industrial induction machine is studied as a benchmark machine and results are compared to measured data to validate the FEA model. The benchmark machine is shown to have a poor traction characteristic. The proposed design procedure is employed to redesign the machine to achieve a traction characteristic.

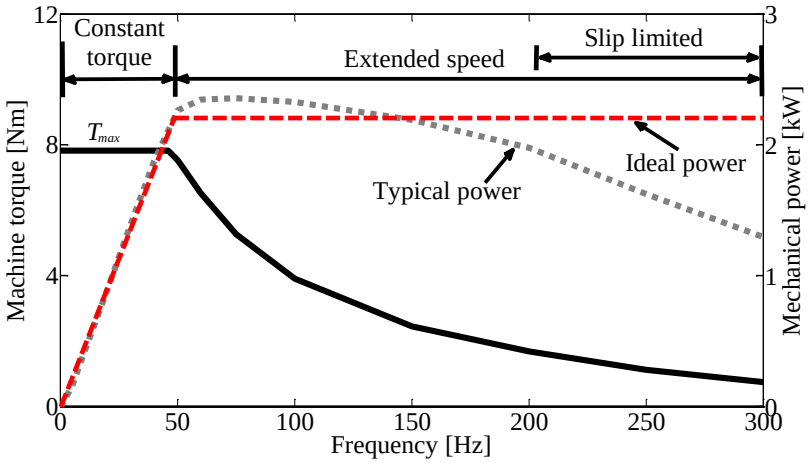

Fig. 4.1. Torque and power characteristics of the benchmark IM.

4.2 Existing Induction Machine Design Studies

Traditionally, the initial stage design process is based on empirical equations to produce the basic dimensions and geometrical parameters that satisfy the machine requirements at the steady-state rated operation point. Then, finite-element analysis (FEA), which permits higher accuracy electromagnetic analysis, is utilized to predict detailed performance. The traditional induction motor design steps are illustrated in Fig. 4.2. Usually, the machine dimensions and geometrical parameters have to be changed and analyzed iteratively before a final acceptable result of the rated operation point is achieved [70]. However, for variable speed applications, the traction machine should satisfy the requirements over the whole load cycle rather than one operating point.

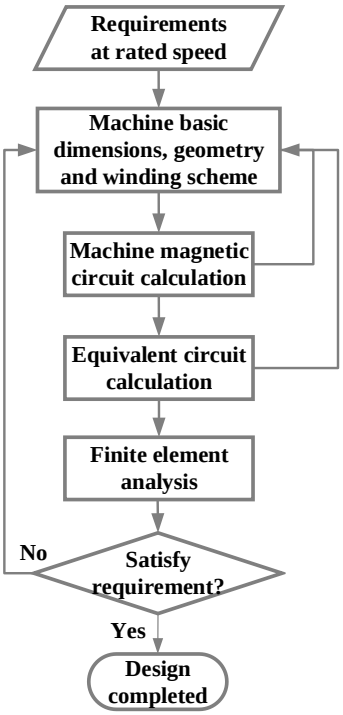

Fig. 4.2. Traditional IM design steps.

To maximize machine performance, much attention has been paid to optimization procedures for IM design. Generally, the induction machine is required to be expressed as

mathematical functions for optimization algorithms. Most of the optimization objects, such as efficiency and maximum torque, can be achieved by seeking the maximum or minimum values of the functions under the machine constraints [71]. For example, optimization algorithms in [71-73] were developed for maximizing the maximum torque-to-nominal torque ratio, starting torque and minimizing machine mass and volume respectively. The design strategies proposed in [74, 75] determined the optimum rotor slot shape for maximum efficiency. Furthermore, a trade-off among the different constraints in terms of supply voltage, pole number and maximum speed was investigated in [76]. However, for one specific optimization algorithm, only one of the machine features and one operation point is optimized. To optimize the machine overall operating points, a wide multidimensional variable design space is required, which is difficult to implement and extremely time consuming for FEA evaluation. In addition, the machine field weakening capability is rarely considered by existing optimization algorithms.

Since AC traction machines are driven by PE converters, the positive effects provided by the machine drive can be considered to benefit the machine design, although there are also negative impacts to be overcome [77]. The primary concern of a conventional IM is the starting performance, i.e. requirements for low starting current, high starting torque, high starting efficiency and limited temperature rise. Traditionally, deep-slot or double-cage rotors, which increase the rotor resistance during starting, are adopted for DOL squirrel cage IM to satisfy these starting requirements. However, the deeper the rotor slot is, the more the rotor leakage inductance is, which reduces the machine pull-out torque and power factor. For variable speed IMs, magnitude and frequency of supply voltage can be adjusted to satisfy the starting requirements [78]. In this case, the utilization of deep-slot or double-cage rotor is unnecessary and the improvement of efficiency, power factor and pull-out torque can be expected by using wide and shallow rotor slots. At a certain speed in the field-weakening region, the machine output power drops below the rated power and the ratio of this speed to the base speed is defined as constant power speed ratio (CPSR) [79], Fig. 4.1. Generally, the highest torque demand and the maximum speed requirement are the main initial design parameters for traction machines [80, 81]. Therefore, a higher value of

CPSR is conducive to the reduction of machine rating [7], which requires a higher maximum torque to nominal torque ratio [82-85]. The authors in [83-85] pointed out that the machine maximum torque can be improved by changing the machine lamination geometry and airgap to obtain lower stator and rotor leakage inductance. In addition, the results presented in [83-85] highlight that the use of variable speed drives yields new design freedoms compared to FVFF driven IMs that can be used in the traction design procedure. However, these results only provide methods to improve some certain aspects of conventional IM performance. Thus, complete traction machine design procedure still needs to be explored.

The design procedure proposed in [86-89] extended the conventional IM design procedure to an iterative design program over the full IM speed range. The method is based on the use of classical empirical formulae to produce the machine initial dimensions and geometrical parameters, the machine performance is then tested over the whole speed range and the machine dimensions and geometry are modified iteratively until the machine performance satisfies the traction requirements. However, this method relies on the developed software for simulation iterations and is time consuming. More importantly, there is no clear guidance and results for achieving the traction characteristics. The work in [90] presented an IM design procedure for field-weakening operation, which does not require an iterative program. It is carried out to evaluate IM parameters to achieve a given field-weakening region of operation and then the machine dimensions are obtained by solving a system of non-linear equations based on the evaluated parameters. However, this design procedure is highly dependent on the machine formulae and the detailed geometric parameters cannot be determined.

4.3 Modelling of Variable Speed Induction Machines

For a given PE converter driven IM, the machine stator phase current is limited by the converter current rating and machine thermal rating. The stator phase current vector angle is chosen to keep the machine operating at maximum torque-per-Ampere (MTPA) until the maximum phase voltage constrained by the DC link voltage is reached [91].

4.3.1 Classical Torque and Power Characteristics

Ideally, the IM torque and output power are characterized by three classical operation regions:

(i) constant torque,

(ii) power to maximum speed and

(iii) slip limited (or natural mode) [67, 82], as shown in Fig. 4.1.

In the constant torque region (zero to base speed), the machine rated torque can be maintained by keeping a constant voltage-frequency ratio (V/f). The constant V/f also maintains the flux level and machine currents to the rated value. In this case, the machine output power increases linearly with the increase of supply voltage. At the base speed, the supply voltage magnitude is limited by the maximum PE converter DC-link voltage. If the supply frequency keeps increasing, the V/f ratio is no longer constant and the machine enters to the extended speed region where the machine current is constant but the airgap flux reduces inversely proportional to the supply frequency. Hence, torque decreases inversely proportional to the speed. Above the machine operates at pull-out slip to maximize the output torque, which results in a reduction in output power.

Obviously, the machine parameter variations are not fully considered by classical IM characteristic analysis, so that the machine torque and power performance cannot be characterized accurately. This issue may give rise to misleading IM analysis, especially in the extended speed region. In practice, the machine is controlled to move along the MTPA trajectory in the constant torque region. In the field-weakening region, the motor can produce more peak output power than rated power, due to the decrease of the magnetizing component of stator current and increase of the torque component [92]. However, with the

increase of supply frequency and slip speed, the IM becomes more and more inductive so that the output power starts to reduce.

4.3.2 MTPA Derivation

In the synchronous reference frame, the IM rotor flux-linkage and voltage in the *d*- and *q*-axis can be expressed as [93, 94]:

$$\begin{bmatrix} \psi_{rd} \\ \psi_{rq} \end{bmatrix} = L_r \begin{bmatrix} i_{rd} \\ i_{rq} \end{bmatrix} + L_m \begin{bmatrix} i_{sd} \\ i_{sq} \end{bmatrix} \tag{4.1}$$

$$\begin{bmatrix} V_{rd} \\ V_{rq} \end{bmatrix} = R_r \begin{bmatrix} i_{rd} \\ i_{rq} \end{bmatrix} + \frac{d}{dt} \begin{bmatrix} \psi_{rd} \\ \psi_{rq} \end{bmatrix} + \left(\omega^e - \omega_r^e\right) \begin{bmatrix} -\psi_{rq} \\ \psi_{rd} \end{bmatrix} \tag{4.2}$$

where V, ψ, R, L and i are voltage, flux-linkage, resistance, inductance and current respectively and the subscripts *s*, *r*, *m*, *d* and *q* represent stator, rotor, mutual, *d*-axis and *q*-axis; ω and ω_r are synchronous speed and rotor speed; superscript *e* represents electrical speed in synchronous reference frame.

With the implementation of the rotor field orientation control, the machine rotor flux is aligned with the *d*-axis, which can be expressed as:

$$\psi_{rd} = |\psi_r|; \;\; \psi_{rq} = 0 \tag{4.3}$$

Hence, the rotor voltage equation of a squirrel cage IM at steady state can be simplified to:

$$\begin{bmatrix} 0 \\ 0 \end{bmatrix} = R_r \begin{bmatrix} i_{rd} \\ i_{rq} \end{bmatrix} + \left(\omega^e - \omega_r^e\right) \begin{bmatrix} 0 \\ \psi_{rd} \end{bmatrix} \tag{4.4}$$

In this case, the machine rotor current is aligned with the *q*-axis:

$$i_{rd} = 0, \; i_{rq} = -\frac{\left(\omega^e - \omega_r^e\right)}{r_r^{'}} \psi_{rd} \tag{4.5}$$

Substituting Equation (4.5) into (4.1), the machine flux linkage is determined by the *d*-axis component of stator current:

$$\psi_r = L_m i_{sd} \tag{4.6}$$

Therefore, the *d*-axis and *q*-axis components of stator current is decoupled, with *d*-axis component the flux component and the *q*-axis component the torque component. The machine electromagnetic torque is derived as:

$$T_e = p \frac{L_m^2}{L_r} i_s^2 \sin\theta\cos\theta = F_1(\theta) \tag{4.7}$$

where *p* is the number of pole-pairs and θ the angle between stator current and rotor flux vectors.

Equation (4.7) indicates that, for certain magnitudes of stator current, the machine torque is a function of θ and hence it can be maximized when θ is optimized. Corresponding to the machine constant torque region, the induction machine MTPA trajectory is ideally achieved by maintaining θ at 45 degrees from zero to base speed, although the actual MTPA trajectory deviates from the ideal trajectory due to saturation effects, as illustrated in Fig. 4.3 (path A-B). The current-limit circle in Fig. 4.3 is determined by the maximum stator phase current. The voltage-limit ellipses are determined by the phase voltage corresponding to different supply frequencies. With increased supply frequency, although the stator current is still maintained at maximum, the voltage provided by the PE converter is not large enough to maintain the MTPA trajectory. In this case, the *d*-axis component of stator current deceases with an increase of stator phase current vector angle, resulting in the machine field-weakening region, as shown in Fig. 4.3 (path B-C).

For the IM, the primary advantage of MTPA is reducing the machine copper loss and hence maximizing the machine efficiency. In addition, the last MTPA operating point is the start of field weakening operation, which is suitable to be chosen for the IM rated point. However, while there is much research on MTPA control for IMs [95, 96], the IM design procedure for MTPA operation is rarely discussed. In this thesis, the IM is designed to achieve MTPA operation at base speed, which also results in power and torque improvements in the field weakening region.

4.3.3 A New Modelling Scheme for Variable Speed IMs

In this section, a new IM modelling process is expressed, which leads to more accurate torque and power characteristics over the whole speed range than the classical characteristics.

Since the flux component and torque component of the stator phase current are aligned with the *d*-axis and *q*-axis respectively, the stator phase current vector angle, as the main parameter impacting on the MTPA operation, is derived as:

$$\theta = \arctan\left(\frac{i_{sq}}{i_{sd}}\right) = \arctan\left[\frac{L_r\left(\omega^e - \omega_r^e\right)}{R_r}\right] \tag{4.8}$$

In order to investigate the machine parameters impacting the current angle, the IM electromagnetic torque derived from the IM equivalent circuit is introduced:

$$T_e = \frac{m_1 p}{2\pi f}\frac{V_s^2\frac{R_r^{'}}{s}}{\left(R_s + c\frac{R_r^{'}}{s}\right)^2 + (X_{s\sigma} + cX_{r\sigma}^{'})^2} \tag{4.9}$$

$$c \approx 1 + \frac{X_{1\sigma}}{X_m}$$

By combining it with the IM equivalent circuit, θ can be represented by the IM equivalent circuit parameters and supply frequency:

$$\theta = \arctan\left(\frac{4\pi pAL_r f_s}{-B + \sqrt{B^2 - 4AC}}\right)$$

$$A = \frac{2\pi f_s}{p}c^2 T_e \tag{4.10}$$

$$B = 2\frac{2\pi f_s}{p}T_e R_s c - V_1^2 m_1$$

$$C = \frac{2\pi f_s}{p}T_e\left[R_s^{\,2} + (X_{ls} + cX_{lr}^{'})^2\right]$$

where m_1, f_s, R_s, X_{ls}, X'_{lr}, R'_r, X_m and T_e are phase number, frequency, stator resistance, stator leakage reactance, rotor leakage reactance and rotor resistance, magnetizing reactance and electromagnetic torque respectively. Note, the rotor values are referred to the stator side.

Assuming the resistances and inductances of the equivalent circuit are constant, then by combining Equation (4.7), (4.8) and (4.10), the stator phase current vector angle is only determined by the supply frequency. Hence, the machine output power can be expressed as a function which depends on θ or f_s:

$$\begin{aligned} \theta &= F_2(f_s) \\ T_e &= F_1\left[F_2(f_s)\right] \\ P &= T_e\omega_r = F_3(\theta) = F_3\left[F_2(f_s)\right] \end{aligned} \tag{4.11}$$

Equation (4.11) indicates that the IM output power envelope varies with the stator phase current vector angle, which is determined by the supply frequency, rather than remaining constant.

Fig. 4.4 summarizes the scheme of the IM modelling method. Here, the IM current is thermally limited and the machine voltage is constrained by maximum DC-link voltage. Firstly, the *dq* two-axis model is used to obtain the current angle, θ. The steady-state per-phase equivalent circuit, which is derived from the *dq* model, includes expressions for per phase parameters which thus enable the current angle, θ, to be expressed in terms of the machine design parameters. Then, the stator current and voltage constraints are applied to calculate the machine torque and output power function, i.e. Equation (3.7). The supply frequency is provided as input to achieve a more accurate torque and power characteristics.

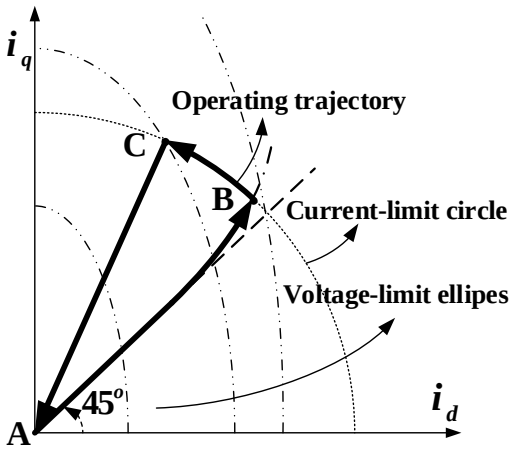

Fig. 4.3. IM operating trajectory.

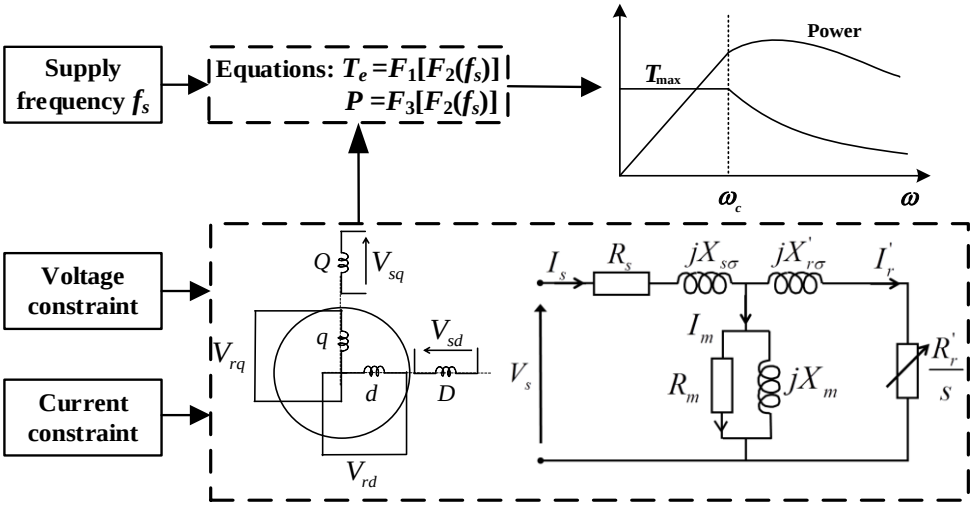

Fig. 4.4. New IM modelling scheme.

4.3.4 Main Parameters for Traction Machine Design

Previous analysis indicates that the stator phase current vector angle of 45 degree offers MTPA operation in constant torque region. For IM field weakening operation, since the d-axis component value of the stator current is larger the *q*-axis component, the stator phase current vector angle is between 45 to 90 degrees. By substituting Equations (4.7) and (4.8) into (4.11), the machine output power can be rewritten as:

$$P = \frac{L_m{}^2 i_s{}^2}{L_r}\left(\omega \sin 2\theta - \frac{pR_r}{L_r}\sin^2\theta\right) \tag{4.12}$$

It can be noticed that, for certain machine parameters, the machine output power in the field-weakening region increases with reduction of the value of θ. To investigate the impact of machine parameters on the value of θ, the machine model is normalized in per unit form. The machine base speed is chosen as one per unit speed. Fig. 4.5 illustrates θ the versus different equivalent circuit parameters at both 1.0 and 4.0 p.u. speeds with unity utilisation of supply current and voltage. It indicates that for both rated and high speed operation, θ is much more sensitive to the change of magnetizing reactance than the other parameters. Further, it can be found that, when the stator or rotor leakage reactance rises to a certain value, θ stops increasing because the stator current cannot remain maximum and the machine begins to enter to the slip limited region, Fig. 4.5 (b). The machine magnetizing reactance is expressed as:

$$X_m = 4 f_s \mu_0 \frac{m_1 \left(N_1 K_{dp1}\right)^2}{K_s p} l_{ef} \frac{\tau}{\delta_{ef}} \tag{4.13}$$

where μ_0, N_1, K_{dp1}, K_s, l_{ef}, τ and δ_{ef} represent the permeability of vacuum, number of stator winding turns, winding factor, full loading electric potential, effective core length, pole-pitch and effective airgap length respectively. According to Equation (4.13), then for a certain frequency, the X_m can be determined by the stator winding scheme, effective core length, pole-pitch, effective airgap length, and especially the number of winding turns, which provides the guidance for machine design to extend the constant power operation.

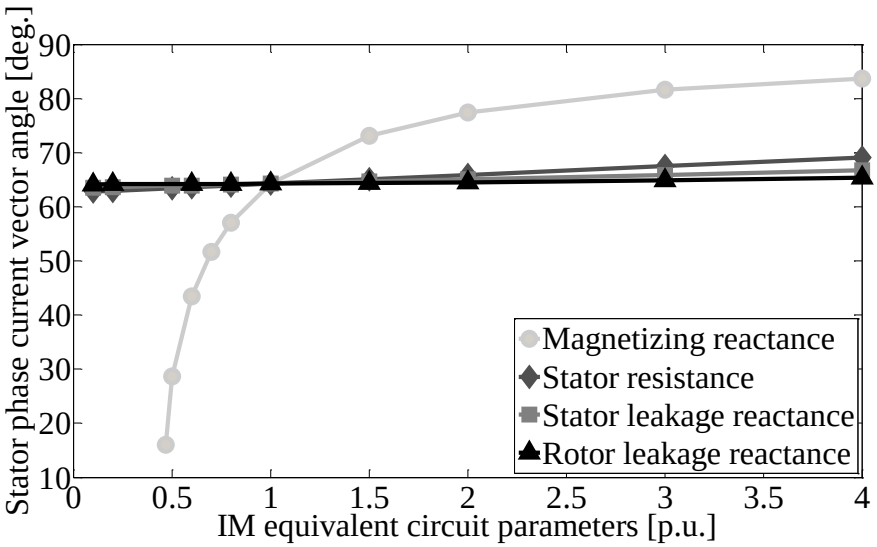

(a) At base frequency (speed), 50 Hz.

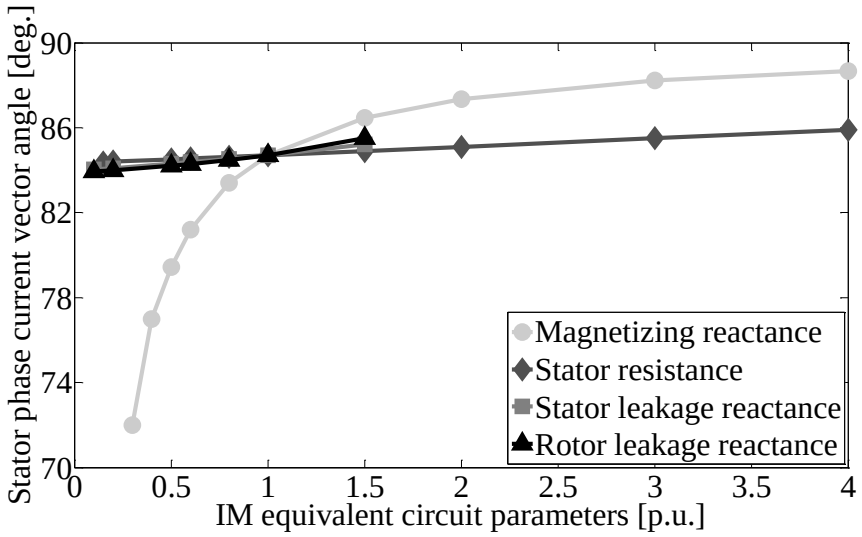

(b) At 4 x base frequency (speed), 200 Hz.

Fig. 4.5. Stator phase current vector angle versus IM equivalent circuit parameters.

4.4 IM Design Procedure for Traction Applications

4.4.1 Conventional IM Design Procedure

Conventional IM design typically proceeds from the application of classical sizing equations. According to the torque and power requirements at the rated operating point, the machine electric and magnetic loadings are estimated by industrial standards and hence the machine dimension, slot geometry and stator winding are established using empirical sizing formula. Then, the flux densities of the machine slots, yokes and air gap are calculated by machine magnetic circuit analysis. Discriminant analysis is applied to check the flux densities of different parts of the machine stator and rotor laminations. Based on the stator winding scheme and rotor slot geometry, the machine main inductance, stator and rotor resistance and leakage inductance are calculated, which determines the IM equivalent circuit. In this way, the machine rated performance, in terms of torque, power and efficiency at rated operating point, is obtained. Finally, the machine starting capability is evaluated. In this procedure, the values of empirical coefficients, such as full load EMF coefficient and saturation coefficient, are initialized and iterated. When the design results cannot satisfy the requirements, machine size and parameters will be adjusted to reach a satisfactory design. A detailed Conventional IM Design Procedure is illustrated in Fig. 4.6.

4.4.2 Traction machine design procedure

The design procedure of a traction machine with wide speed range is different from that of the traditional FVFF induction machine. The IM analysis in the previous sections clarifies the impact of the stator phase current vector angle on IM rated and high speed operation, and further on the machine design procedure. In order to extend the constant power range, a smaller stator phase current vector angle is preferred for high speed operation. On the other hand, in constant torque range, the current angle of 45 degrees is desired for the MTPA trajectory.

Fig. 4.7 compares the flowcharts of conventional and variable-speed IM design procedures. It can be observed that due to the vector controlled PE converter, the starting torque is not

a machine design requirement for traction IMs. More attention is paid to the requirements of MTPA and field weakening operations. This design procedure is proposed with theoretical support, which provides a clear guidance for traction machine design. It is efficient and does not rely on random iterations and complicated, and sometimes inappropriate, optimization algorithms. The three main steps are:

(1) Design the machine at Base Speed:

This procedure starts with a machine design at base speed, since this operating point specifies the maximum steady state torque and power specification. The traction machine dimensions are initially calculated by using classical sizing equations. FVFF DOL IM designs need to satisfy the high start-up torque and overload capabilities, the consequence of which leads to the stator phase current vector angle being away from 45 degrees. For some traction applications, such as electric vehicles, the machine is designed with high electric loading, which results in heavy saturation at base speed. In this case, the stator phase current vector angle is greater than 45 degrees. In order to achieve the MTPA operation at base speed, the initial design has to be modified by tuning the main geometric design parameters.

(2) Stator winding tuning for MTPA operation:

The stator phase current vector angle θ significantly impacts on the machine torque and power performance. The value of θ is sensitive to the value of machine magnetizing reactance which is related to the stator winding scheme and directly proportional to the square of the number of stator series turns per phase. Therefore, the value of θ at base speed can be effectively decreased to achieve MTPA operation by reducing the number of winding turns. At the same time, the stator phase current vector angle is also reduced at high speeds, which improves the machine field-weakening capability. Further, due to the reduced stator winding turns, the machine electrical loading is decreased, reducing the maximum torque in the constant torque region. This trade-off is typical of other machine technologies, i.e., PM [97] and SR machines [69]. In order to balance the maximum torque and field weakening performance, the machine rotor design is modified.

(3) Rotor redesign:

Reduction of the number of stator winding turns provides a number of benefits. Firstly, the machine field weakening performance is improved, as discussed above. In addition, the stator resistance is decreased so that the stator copper loss is reduced. More importantly, since the stator conductor area is reduced, the stator slot area can be smaller. In this case, keeping the same stator outside diameter, the stator inner diameter can be enlarged so that the rotor diameter can be increased, which is an effective method for more torque production, as the torque increases proportional to the square of rotor radius. On the other hand, for PE converter driven IM, a suitable torque at zero speed can be obtained without excessive rotor resistance [78]. Therefore, lower rotor resistance and leakage inductance can be achieved by using wide and shallow rotor slots and hence an enhancement of efficiency, power factor and peak torque can be expected [77]. In addition, to reduce the rotor Joule loss, copper can be used as the rotor bar material. The machine performance at both base and maximum speeds will be evaluated after the design. If the requirements are still not satisfied, the main machine dimensions have to be modified and the procedure repeated.

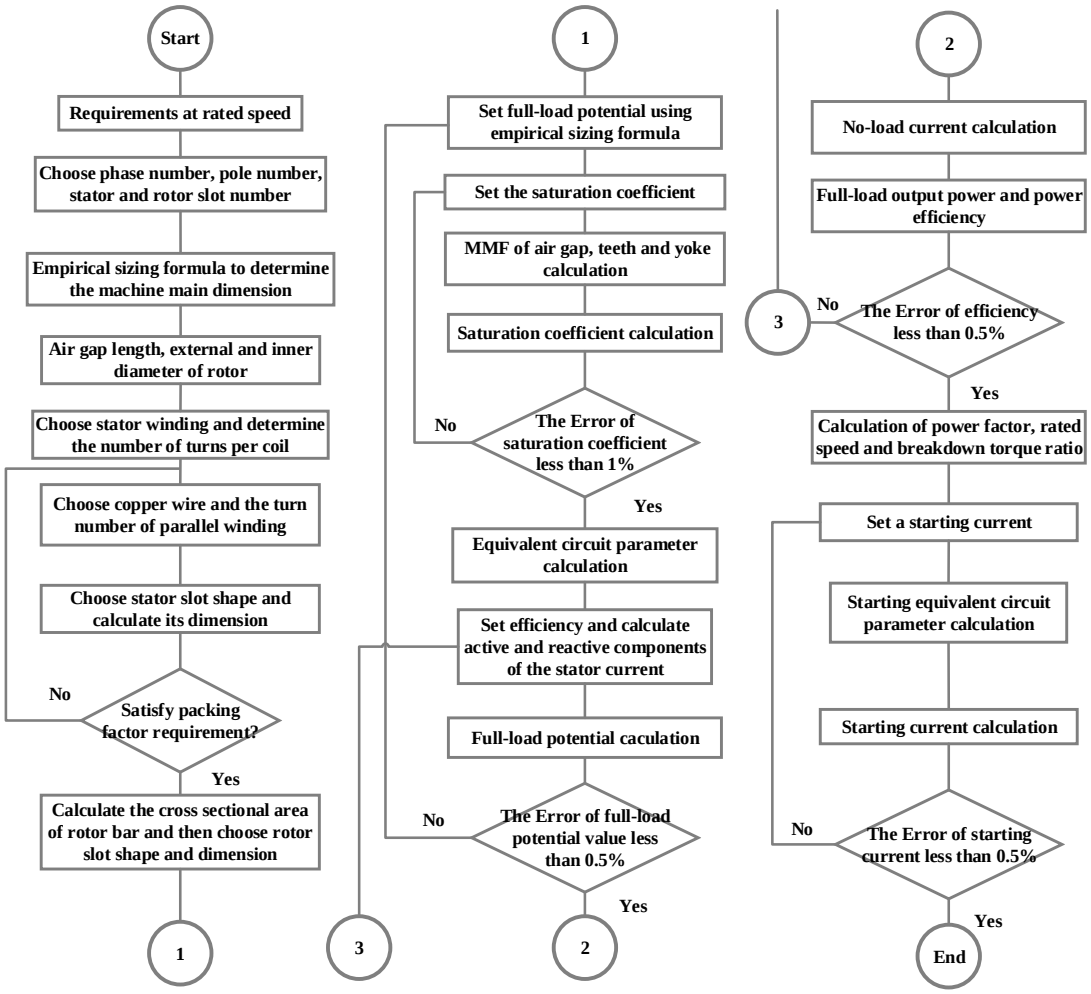

Fig. 4.6. Traditional IM design procedure

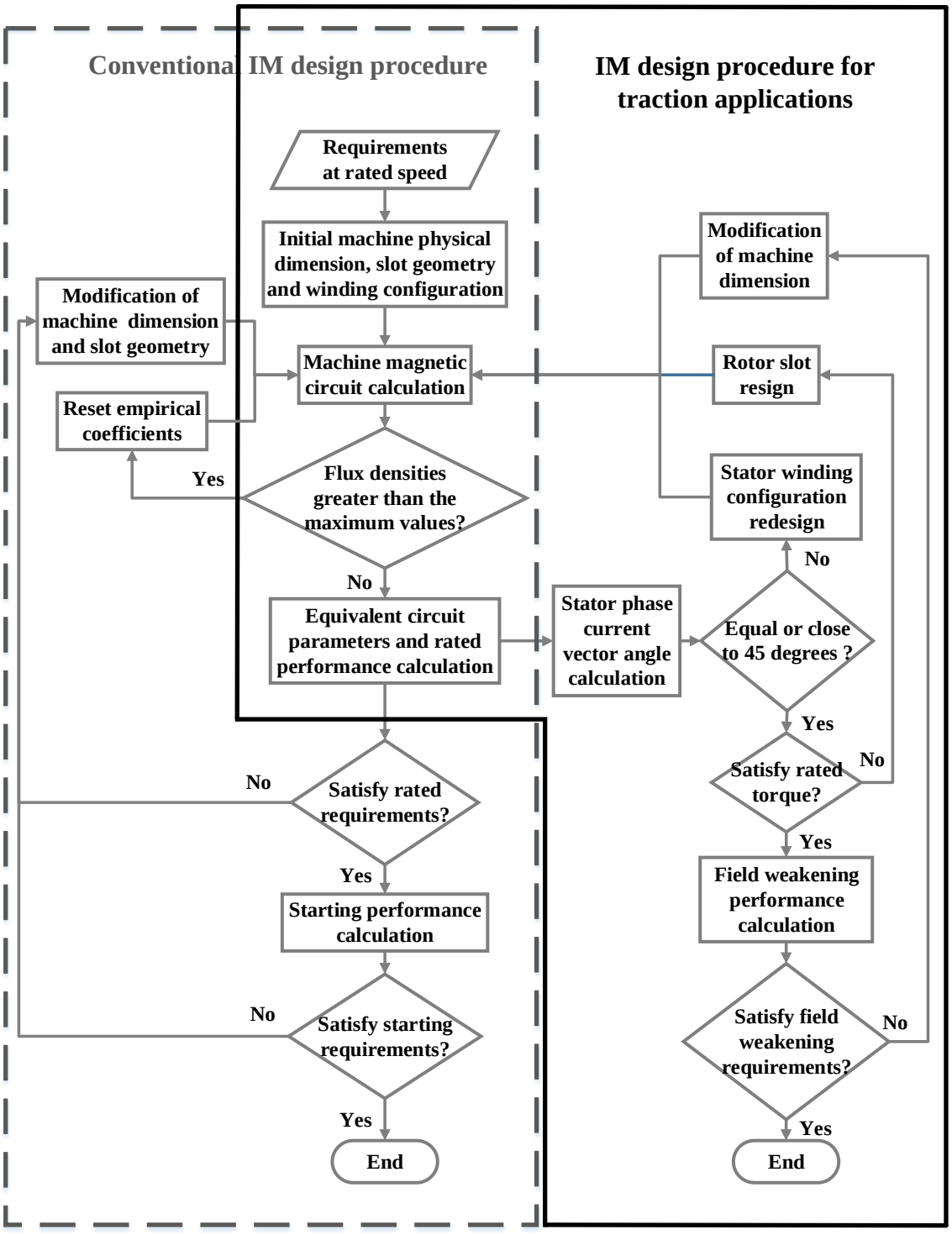

Fig. 4.7. Comparison between conventional and traction characteristic design procedures for IMs.

4.5 Analysis and Further Design of an Example IM

4.5.1 Benchmark Machine Analysis

In this section, a conventionally designed FVFF DOL 2.2 kW IM, Fig. 4.8, is studied as a benchmark machine to illustrate the new traction design procedure. For analysis and further design of this machine, a detailed finite element analysis (FEA) model is developed. The FEA model is validated by comparing the simulation results with the measured results, an example of which are presented in Table 4.1 at the machine rated operating point. It can be observed that the model calculation agrees with the measured data within acceptable experimental error.

Fig. 4.1 illustrated the torque and power characteristics results from the FEA model. The output power increases linearly with increase of the supply frequency in the constant torque region, until the phase voltage constraint is reached at the rated operation point. However, in the field weakening region, the torque does not simply decrease inversely proportional to speed. The machine output power initially rises and then reduces with increasing frequency. According to Equation (4.10) and (4.12), the stator phase current vector angle at base speed is 65 degrees and it progressively increases in the field-weakening region. Therefore, MTPA is not obtained at base speed and machine output power cannot remain constant in the field weakening region, which results in the machine CPSR of only 2.3:1.

4.5.2 Effects of number of stator winding turns

The constant power region can be extended by reducing the number of stator series turns per phase. Hence, by maintaining the dimensions and lamination geometry of the benchmark IM, the machine torque and power performance with a variable number of stator winding turns is investigated, as illustrated in Fig. 4.9. It can be noticed that with reducing turns, from 45 to 35, the machine high speed performance is improved, in Fig. 4.9 (a). However, with fixed phase current, reduction of winding turns reduces electrical loading and hence the maximum torque in the constant torque region is reduced, as illustrated in Fig. 4.9 (b). This is the design trade-off.

Table 4.1. List of Important Nomenclature and Parameters.

Quantity	Measured data	Model data
Line to line voltage (Vrms)	400	400
Supply phase current (Arms)	4.29	4.29
Load torque (Nm)	7.27	7.57
Rotor speed (RPM)	2885	2871
Stator Joule loss (W)	189	189.36
Rotor Joule loss (W)	89.4	87.86
Iron-core loss (W)	62.2	63.5
Efficiency (%)	84.89	86.97
Power factor (p.u.)	0.87	0.88

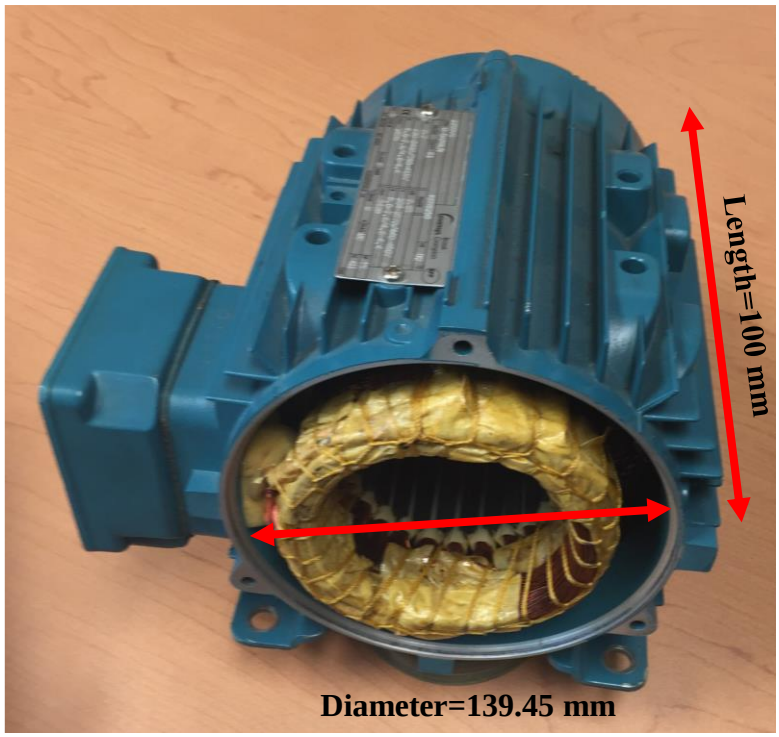

Fig. 4.8. 2.2 kW induction machine.

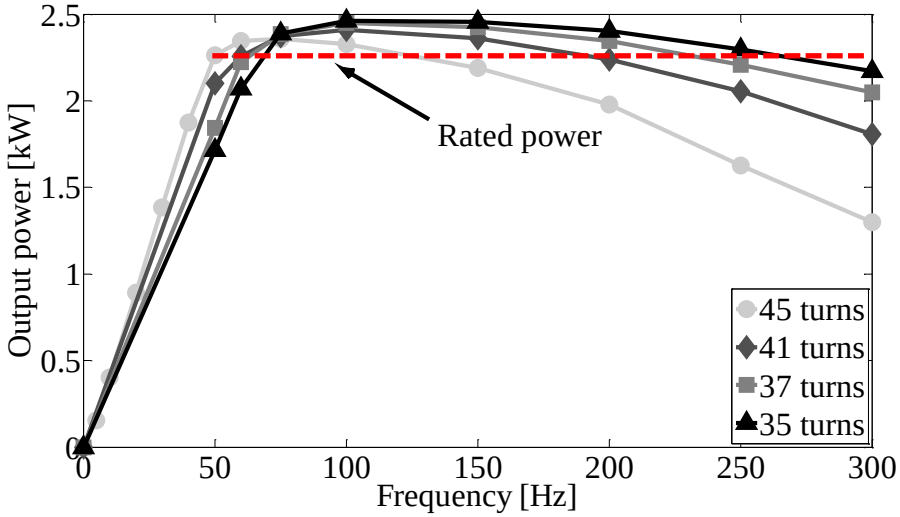

(a) Mechanical power versus frequency (speed).

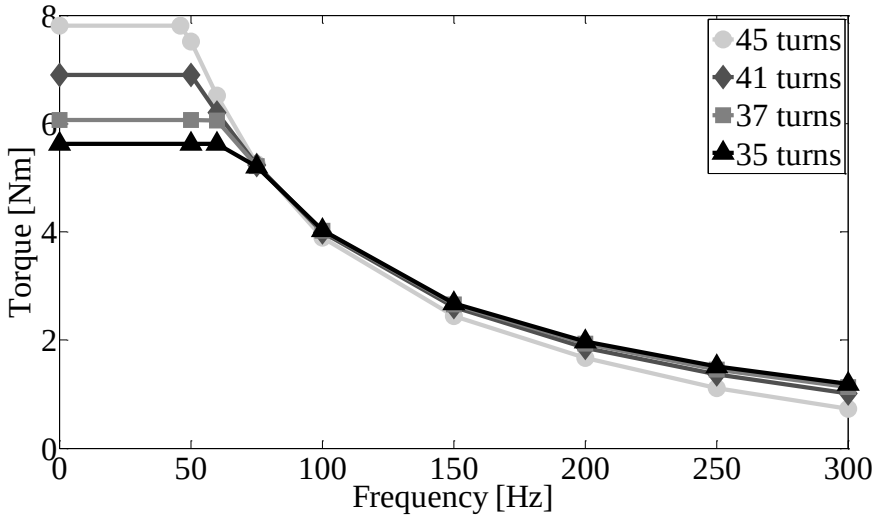

(b) Torque versus frequency (speed).

Fig. 4.9. Machine performance as a function of stator winding turns.

4.5.3 Rotor Redesign Results

The decrease of torque due to reduced stator turns can be compensated by the rotor redesign of the FVFF DOL IM rotor. As discussed previously, PE converters control current and frequency. Hence, large rotor resistance for starting is no longer a design goal. Therefore, conventional deep and narrow rotor slots can be replaced by shallow and wide ones, as shown in Fig. 4.10 (a). Such a rotor slot design contributes to the reduction of rotor resistance and leakage reactance, which results in the increase of machine efficiency, power factor and pull-out torque. In addition, the rotor slot is semi-opened to improve the machine maximum torque output. Since the stator phase current vector angle is robust to the rotor resistance and reactance, the machine MTPA will not be impacted.

Keeping the same machine dimension and same rotor bar material (aluminium) with the benchmark IM (Motor 1), a new IM (Motor 2) is designed by utilizing the proposed procedure. Fig. 4.10 (a) illustrates the machine rotor slot geometry and Fig. 4.11 power (b) and torque-speed (c) characteristics. Table 4.2 summarizes the design results. Since the benchmark machine is not designed to achieve MTPA at rated operating point, the maximum torque in the lower frequency region is 3.9% higher than the rated torque at 50 Hz, which means the machine is overdesigned from a traction perspective. Motor 2 is designed with base speed as the rated operating point. Therefore, Motor 2, maintain the same rated torque, contributes a 13% reduction in loss and hence achieves a 1.5% higher efficiency. In addition, there are improvements in terms of efficiency and power factor in the field weakening region. Especially, at high speed operating point (300Hz), the efficiency gain is 8% and power factor improved by 0.24 p.u., which results in the high speed torque and output power of Motor 2 being significantly (70%) greater than Motor 1. More importantly, the machine CPSR is improved to be 4.5:1, compared to the benchmark machine CPSR of 2.3:1. However, using wider rotor slots results in a lower of rotor bars, which gives rise to higher torque ripple.

In order to reduce the rotor bar area and increase the rotor bar number, an obvious option is to replace aluminium bars with more conductive material, such as copper, which also offers further improvement of the machine efficiency. Thus, maintaining the same stator

design of Motor 2, the machine rotor is redesigned with die-cast copper bars (Motor 3). The rotor slot shape is still shallow and wide, but the slot area is reduced so that the rotor bar number can be increased. Besides the improvement of machine efficiency, Motor 3 further increases the machine power factor at high speed, which leads to a CPSR of 5.3:1. Moreover, the machine torque ripple over the whole speed range is improved back to the same level of Motor 1.

As discussed in Section 4.4, with the reduction of the number of turns per slot, the stator slot area can be smaller. Consequently, even if stator outside diameter remains the same, the rotor diameter can be enlarged to contribute more torque (Motor 4). The machine laminations and FEA solutions at corner speed of Motor 1 and Motor 4 are compared in Figs. 4.10 (b) and (c) respectively. It can be noticed that Motor 4 has a slight larger rotor than the benchmark machine. In addition, since the stator phase current vector angle is decreased by means of the proposed design procedure, the field component of the stator phase current is enlarged, which results in a slight increase of flux density for Motor 4.

4.5.4 Parameter Test and Performance Analysis

The machine parameters of the four induction machines, for both rated speed and high speed, are obtained by no-load and locked-rotor test, Fig. 4.10 (a). Obviously, the machine parameters can be divided into two groups:

(i) original machine (Motor 1), with higher magnetizing reactance (X_m), higher leakage reactance (X_{ls} and X_{lr},) and consequently larger current vector angle (θ), and

(ii) new machine designs (Motors 2, 3 and 4), with lower magnetizing reactance, lower leakage reactance and consequently smaller current vector angle.

Motor 4 achieves the lowest leakage reactance and current vector angle for both rated speed and high speed. Correspondingly, the power- and torque-speed characteristics of Fig. 4.10 are divided into two groups:

(i) original machine and

(ii) new machine designs.

It can be noticed that the new machine designs contribute a significant improvement to field-weakening performance. Motors 3 and 4, with copper rotor bars, have a wider constant power region than Motor 2, with aluminium rotor bars. The power and torque performance of Motors 3 and 4 are close, although Motor 4, with lower leakage reactance, realise a higher power factor and saves copper material due to the lower number of stator winding turns.

Table 4.2. Comparison of design results and performance.

Quantity		Motor 1	Motor 2	Motor 3	Motor 4
Core length (mm)		100			
Airgap length (mm)		0.3			
No. of stator slots		24			
Stator D_o / D_i (mm)		137.45 / 66.68	137.45 / 66.68	137.45 / 66.68	137.45 / 69.68
No. of winding turns		45	41	41	40
Rotor bar material		Aluminium		Copper	
No. of rotor bars		29	25	27	27
Joule loss (W)	50 Hz	277.25	228.34	198.29	205.94
	300 Hz	196.5	253.75	210.25	216.57
Iron-core loss (W)	50 Hz	63.52	70.41	71.23	70.53
	300 Hz	84.35	22.77	23.81	24.6
Efficiency* (%)	50 Hz	86.97	88.38	89.45	89.22
	300 Hz	80.21	88.08	90.28	90.21
Power factor* (p.u.)	50 Hz	0.880	0.890	0.885	0.888
	300 Hz	0.56	0.80	0.83	0.86
Torque (Nm)	50 Hz	7.57	7.57	7.59	7.59
	300 Hz	0.73	1.13	1.21	1.23
Pk-pk torque (Nm)	50 Hz	0.61	1.06	0.56	0.65
	300 Hz	0.12	0.45	0.11	1.11

* Neglecting considering windage and friction loss

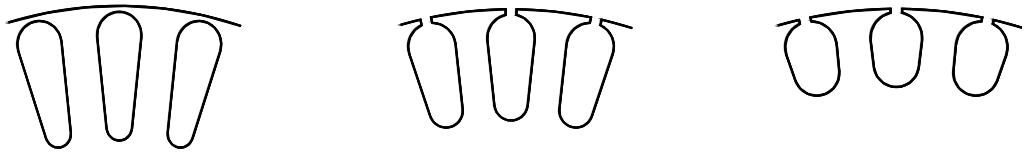

Design 1 Design 2 Designs 3 and 4

(a) Comparison of IM rotor slots.

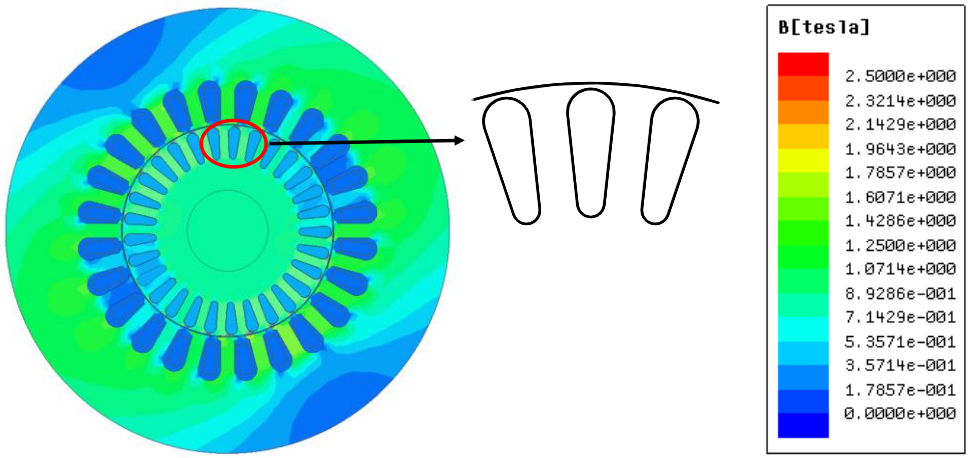

(b) Machine laminations and flux distribution for Motor 1 at 50 Hz.

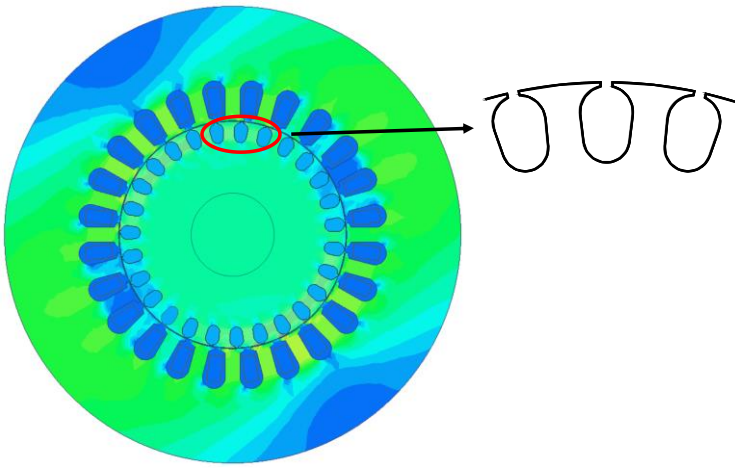

(c) Machine laminations and flux distribution for Motor 4 at 50 Hz.

Fig. 4.10. Machine designs and flux distributions.

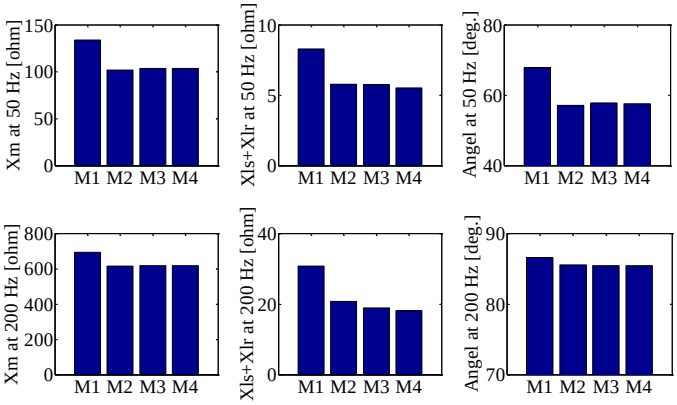

(a) No-load and locked-rotor test parameters of the four machine design.

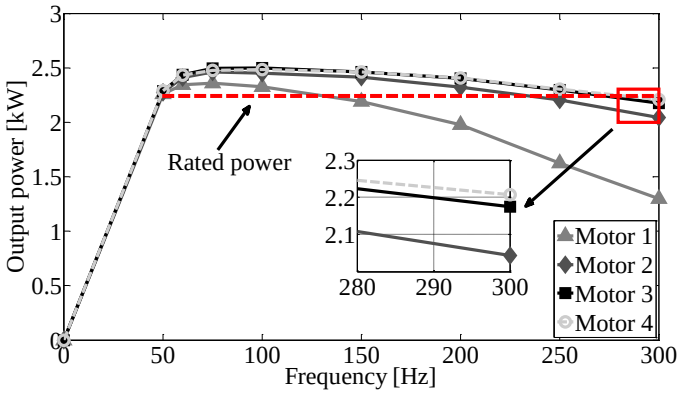

(b) Mechanical power versus frequency (speed) characteristics.

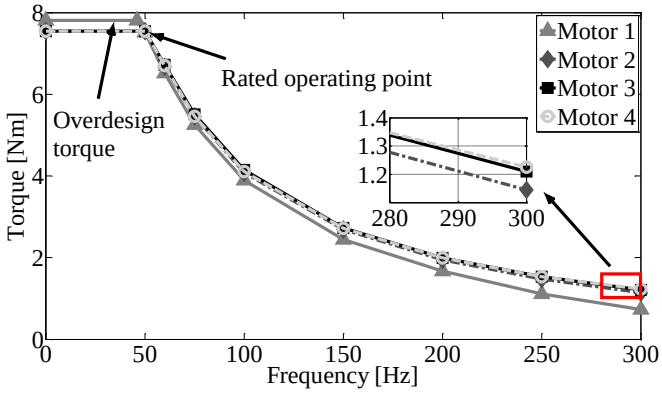

(c) Torque versus frequency (speed) characteristics.

Fig. 4.11. Machine designs and flux distributions.

4.6 Conclusions

Traction machines, supplied via PE converters, have to be designed for the complete power-speed characteristic rather than one or two key steady-state operating points as would generally be the case for FVFF DOL IMs. Therefore, the machine modelling and design procedures are different. According to existing published works on variable speed IM design, most of the machine design relies on optimization algorithms or iterative calculation programs and the key parameters for machine design are thus not clearly identified. This Chapter proposes a new modelling scheme for variable speed IMs that identifies the key design parameters influencing the traction torque-speed characteristic. At base speed the magnetizing reactance, X_m, is the dominant parameter that impacts on machine torque. However, in the field weakening region, the stator phase current vector angle, θ, becomes the main design parameter. The IM extended-speed operation can be achieved by reducing the magnetizing reactance, X_m, (by reducing the number of turns per phase). In this case, the low speed torque will be decreased due to the reduction of Ampere-turns. Then, the rotor resistance, $R_r^{'}$, and leakage inductance, $X_{lr}^{'}$, will be decreased (using wide, shallow and open mouth slots instead of narrow, deep and closed mouth slots) to compensate for the torque reduction. Thus, the design concept is similar to that of PM machine design, where the back-EMF coefficient, k_o, is adjusted and the d-axis inductance–phase current product, $L_d I_s$, increased to improve the extended field weakening region.

Based on these points, an IM design procedure for traction applications is proposed. An FVFF DOL IM is studied as a benchmark machine which is subsequently redesigned using the proposed design procedure to illustrate the procedure and show improvements of machine performance in terms of efficiency, power factor and field weakening capability.

Chapter 5

An Investigation on the Impacts of DC-Link Voltage and Temperature Variations on EV Traction System Design

5.1 Introduction

As discussed in earlier Chapters, the EV traction system consists of electric traction machine(s), power conversion electronics and energy source(s). The energy source(s) provide a DC voltage or DC-link supply via power electronic converters, which in turn supplies or accepts energy to/from the traction machine. Since the energy density of electro-chemical batteries is significantly less than gasoline [99], high efficiency power-trains are a necessity to achieve reasonable vehicle driving range.

The appearance of high-performance rare-earth magnets make brushless permanent magnet (PM) machines suitable candidates for EV traction, since they promise high energy conversion efficiency and high torque density within vehicular volume and mass constraints [100]. As discussed in Chapter 2, BLPM machines generally have two types of rotor topologies: (i) interior permanent magnet (IPM) rotor, where magnets are buried within the rotor body, and (ii) surface-mounted PM rotor (SPM), where magnets are mounted on the rotor surface [101]. IPM machines have the widely quoted benefits of saliency torque contribution, less magnet mass, superior demagnetization withstand [102] and, as such, have been widely adopted in commercial hybrid electric vehicles (HEVs) such as the Honda Accord, Hyundai Sonata and Toyota Prius, and all-electric vehicles (EVs), such as the

Nissan Leaf [103]. However, the authors in [104] indicate that SPM machines are also a suitable traction machine topology when they are appropriately designed.

In EV traction systems, the battery provides a DC-link to supply DC power to the traction inverter that then converts DC to AC power to drive the traction machine, TM in Fig. 5.1 (a). The process is reversed for regenerative braking of the vehicle. DC-link voltage and temperature variations are critical issues when designing an electric vehicle traction system. For brushless PM machines, ambient temperature variation impacts the performance of the rotor PM material and hence machine operation, a feature that should be considered at the PM traction machine design stage. Additionally, when there is no control of the DC-link voltage, the DC-link voltage varies during vehicle loading cycles, which impacts the performance of the traction machine and hence vehicle power-train, and also impacts the inverter voltage and current requirements.

Considering the DC-link voltage variation, existing literatures discuss the advantages and disadvantages and control strategies implemented when a DC/DC converter or a power buffer is connected between the battery and inverter. However, the decision is not clearly defined and is confused by individual application preference. In addition, the impact of voltage and temperature variation on the IPM traction machine torque and power performance have seldom been evaluated and hence solutions are not suggested. Traction system design and sizing based on the above issue has not been reported to-date. This chapter therefore evaluates the performance of a benchmark battery EV traction system, by considering variations in DC-link voltage and ambient temperature for accepted automotive operation. The Nissan Leaf vehicle traction system is used as a benchmark system throughout this Chapter since there is much public domain test data available for the machine and vehicle system that can be used for experimental validation of the subsequent simulation studies reported herein. To overcome the issues of voltage and temperature variations, three solutions, including installing a DC/DC converter, installing a power buffer and traction machine redesign, are explored and compared in this chapter. The trade-off of these solutions are discussed in terms of electronic and machine packaging, and mitigation of faulted operation at high speeds.

5.2 Background and Existing Literature

There are two types of energy storage device for the EV traction system, i.e. primary energy sources that have high energy density and peak power buffers with high power density that compensate or constrain the peak power demand from the primary energy source(s). By way of example, electro-chemical batteries can be used as the energy source in an all-electric traction system or chosen as the main energy source in a hybrid energy source system, where supercapacitors (SCs), for example, operate as peak power buffers. In order to control power flow, it is necessary to install a DC/DC converter in series with the energy source or the peak power buffer or both, as illustrated schematically in Fig. 5.1 (a), where the dashed boxes indicate optional system components. Referring to Fig. 5.1 (a), the SC and DC/DC converter 1 may or may not be included in a pure battery EV power-train. If the vehicle utilizes a hybrid energy source then either DC/DC converter 1 or DC/DC converter 2 may be required as a minimum for system functionality. Traditionally, DC/DC converter 2 and not DC/DC converter 1 would be chosen as a minimum option to ensure good energy utilization if a SC was installed in the power-train [105]. Although the SC system adds complexity and component count, the SC provides transient energy to the DC-link alleviating battery voltage and current stress, which improves battery lifetime [105]. Some assessment of the differences between four typical configurations for EV power-trains are summarized in Table 5.1, where "+" indicates a positive attribute, "-" a negative attribute and "--" a highly negative attribute. The four cases are further explained below. Note:

Case 1: battery alone without DC/DC converter;

Case 2: battery alone with DC/DC converter 1;

Case 3: battery-SC with DC/DC converter 2; and

Case 4: battery-SC with DC/DC converter 1 and 2.

When the DC-link is directly connected to the battery, as is the case for the Nissan Leaf power-train shown in Fig. 5.1 (b) [106, 107], the DC-link voltage varies during vehicle loading cycles due to the state-of-charge (SoC) and internal impedance voltage drop of the battery [108]. This voltage variation impacts on the performance capability of the traction

machine and hence vehicle power-train, and also impacts on the inverter voltage and current requirements. This variation in DC-link voltage limits the traction machine controllable region and field-weakening capability. In addition, the magnitude of DC-link voltage determines the voltage and current ratings for the power converter devices and the traction machine. Authors in [109, 110] discussed traction machine torque control methods and field-weakening strategies by considering DC-link voltage variation. However, the impacts of voltage variation on traction system design, including the traction machine design and traction inverter Volt-Ampere (VA) rating have not previously been reported.

Table 5.1. Comparison of Different Power-train Configurations.

	Case 1	Case 2	Case 3	Case 4
DC-link voltage variation	--	+	-	+
PE* device utilization	+	-	-	--
Complexity and cost	+	-	--	--
Battery protection	--	-	-	+
System control	+	-	-	--

*PE: power electronic

Implementing a bidirectional DC/DC converter between the battery and DC-link to maintain voltage stability ensures the best utilization of the traction machine and inverter at the expense of adding an additional power conversion stage. This is often discussed, but no assessment has been presented to clearly show the impact on component size due to this design choice. This Chapter addresses this deficiency.

In hybrid electric vehicle power-trains, for example the Toyota Hybrid System II (THS II), it is claimed that the DC/DC converter can boost the system voltage and increase the electrical power input of the inverter for the same current level which, combined with the machine rotor optimization, results in a higher machine power output than the previous generation of THS [111]. The boost DC/DC converter also enables some reduction in the number of battery modules connected in series [112] although the impact on reduced battery energy is not made clear, leading to some misconceptions in terms of on-board energy

management. For pure electric vehicle power-trains, the benefits of adding a boost DC/DC converter between the battery and DC-link can be summarized as:

(i) with the DC/DC converter, the battery pack and traction machine can be designed independently [113];

(ii) the boosted DC-link voltage extends the machine maximum speed and power-to-weight ratio [112];

(iii) a higher phase voltage leads to a reduction of machine current to keep constant power, which decreases machine copper loss [114];

(iv) the DC/DC converter ensures a reduced current distortion of the inverter output, which improves the machine torque ripple [115]; and

(v) the adjustable DC-link voltage improves the inverter efficiency at low speed operating points [116, 117], although the DC/DC converter contributes additional losses for the traction system [118, 119].

On the other hand, the inclusion of a DC/DC converter introduces larger passive components, increased complexity, cost and a reduction in reliability [115, 118]. Hence, [115, 118, 119] suggest that it is advantageous not to have a DC/DC converter. However, the decision is not clearly defined and is confused by individual application preference. In addition, the system design and sizing with and without DC/DC converters are not investigated.

With a DC/DC converter implemented, the DC-link voltage may still fluctuate due to the load fluctuation. In order to reduce the fluctuation, several DC-link voltage control strategies for EV power-trains have been studied. In [120], the DC-link voltage is regulated with complicated operating mode detection and control loop transition. In [121, 122], the traction inverter is analyzed as a constant power load and then PID controllers are used to stabilize the DC/DC converter output in vehicle driving mode. By considering the DC-link voltage fluctuation during the operating mode changes, a double loop control strategy is proposed in [123]. In addition, authors in [124] proposed a control algorithm for the Cascaded H-Bridge Three-Level DC-DC converters for DC-link voltage stabilization, which suppresses the DC-link voltage fluctuations by adding a feed-forward control. Authors in [125]

introduce a DC-link capacitor voltage balancing method based on adjusting the width of phase-shifted PWM for battery energy storage systems. Three-level neutral point clamped (NPC) inverters, which have lower switching loss at higher switching frequencies, have been widely suggested for EV traction inverters. If this topology is employed as the traction inverter, the system may suffer from unbalanced DC-link capacitor voltages. To equalize the capacitor voltages, authors in [126] employ a PI controller algorithm to generate the duty cycle for the switches, but this may lead to unsymmetrical switching and increased THD in the DC-link voltage in practice. A hysteresis controller algorithm reported in [127] is another DC-Link voltage balancing method, but it is only suitable for high dynamic EV operation. To overcome these two issues, authors in [128] developed a switching sequence control scheme, which helps to reduce the number of converter switching sequences and balances the two DC-link capacitor voltages. A three-level traction inverter with the proposed DC-Link Voltage Balancing Algorithm is compared with the conventional two-level inverter in [129]. Authors in [130] proposed a space-vector and carrier-based hybrid PWM-based DC-link voltage balancing algorithm for NPC inverters. The NPC switch duty cycles are calculated by the carrier-based topology to reduce the computational time and control complexity; the space vector PWM strategy is employed to balance the two DC-link capacitor voltages. As reviewed above, the DC-link voltage variation caused by transient DC-link voltage fluctuation can be stabilized and balanced by suitable control strategies. However, battery terminal voltage variations due to battery regulation (internal impedance-current voltage drop) and SoC are different issues and the main focus of this Chapter. Here, the use of peak-power buffers and intermediate DC/DC converters to maintain the traction inverter DC-link input voltage will be assessed.

Adding supercapacitors (SCs) in parallel with the battery is another way to improve the DC-link voltage transient variation [131]. In this way, battery current fluctuations can be reduced by controlling the SC voltage. Authors in [132] proposed a rule-based strategy for SC voltage control, which was based on the real-time battery, SC and machine operating conditions. Model predictive control presented in [133] is another method for energy management, which shows good performance when linear models are used. To solve

nonlinear problems, a power control framework is proposed in [134], which comprises of two stages:

(i) computing the SC reference voltage from real-time load dynamics and

(ii) formulating a convex optimization problem to optimize the power flow.

Based on this strategy, authors in [135] introduce an optimization formula to extrapolate the reference SC voltage for next vehicle action, and then a minimization problem is defined to smooth the SC voltage. In addition, fuzzy logic control is employed by [136] for splitting power demand between battery and hence SC, thus reducing the peak charge/discharge current stress on the battery. In [137], an optimization problem is formulated to obtain the optimal current split between battery and SC. A real-time neural network controller is trained based on off-line optimization results to make real-time control decisions, showing improved performance in reducing the battery current fluctuations. Thus, the inclusion of SCs with proper SC voltage control method reduces the battery peak current and hence reduces the DC-link variation. However, it cannot stop the battery voltage decreasing to the minimum value as defined by the battery SoC. Further, although battery-SC combinations with DC/DC converter 1 and 2 achieves controllable DC-link voltage and lower battery peak current at the same time, they result in more complicated system control and PE device utilization, while conceptually incurring a cost penalty. Hence, the cost penalty (in terms of hardware), for improving DC-link power management, is discussed here.

Considering to the ambient temperature, the EV may have to operate in outside ambient of -40 ^{o}C to +40 ^{o}C, with machine rotor temperature variations from -40 ^{o}C to +120 ^{o}C. The PM material B-H characteristic varies with rotor temperature [138]. At low temperature, the magnet remanent flux density for a sintered NdFeB grade is higher. In this case, if traction machine inverter control function is lost, the inverter resorts to an uncontrolled full-bridge rectifier. If such a fault occurs when the vehicle is operating above the system base speed, the machine may generate line-line back-EMFs equivalently higher than the battery terminal voltage, which will result in uncontrollable regenerative currents, possible vehicle braking and hence safety concerns. Theoretically, temperature variation also impacts the battery performance, including terminal voltage and output power. However, hybrid and EV

batteries always have separate battery thermal management, for example Nissan Leaf EV [40]. Hence, the effect of EV battery temperature variations is not discussed in this Chapter

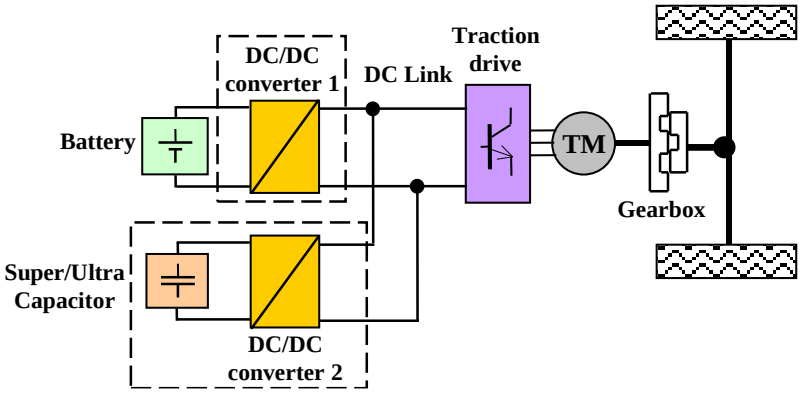

(a) Power-train concepts

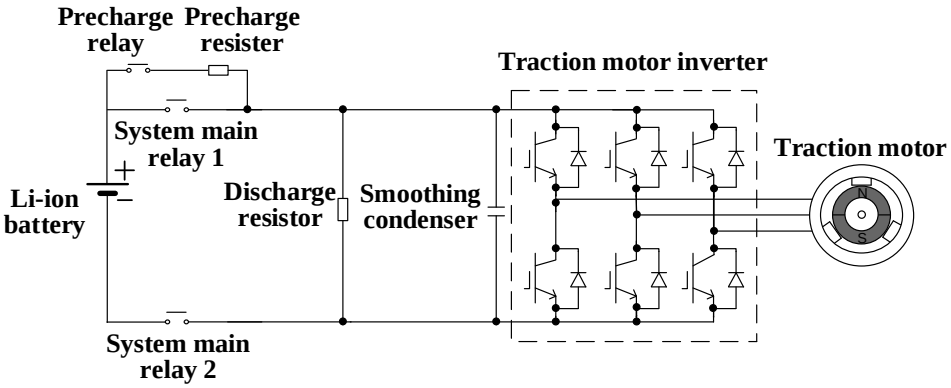

(b) Nissan Leaf benchmark system [106]

Fig. 5.1. Pure electric vehicle power-train

5.3 Electric Vehicle Modelling

As discussed, EV power-trains include energy and/or power sources, power electronic converters and electric machines, as shown in Fig.5.1. As a pure battery electric vehicle, the Nissan Leaf benchmark vehicle is powered entirely by electro-chemical batteries. The batteries form the DC-link and directly connect to the traction machine inverter that converts DC to AC to drive a three-phase IPM machine, i.e. no SC or DC/DC converter contribute to the power-train, as illustrated in Fig. 5.1 (b) showing the layout schematic. Results from a detailed model of the benchmark vehicle and its power-train are discussed in this section. This model is developed by using published vehicle parameters [140, 141] and Oak Ridge National Laboratory (ORNL) measurement data [142, 143]. The models and subsequent simulations presented herein are validated against the Argonne National Laboratory test data reported in [140, 144].

From a physical point of view, the EV is modeled by a backward-facing approach, as shown in Fig. 5.2 (a), with an imposed driving cycle. The model calculates the forces affecting the motion of the vehicle and processes them backwards through the power-train. By analyzing the vehicle dynamics, as shown in Fig. 5.2 (b), the resultant force required for vehicle propulsion is given by [145]:

$$F_d = F_r + mg\sin\theta + \frac{1}{2}\rho C_d A_f v^2 + m\frac{dv}{dt} \tag{5.1}$$

where F_r is the force to overcome the rolling resistance, m is the total vehicle and payload mass, θ is the road gradient, g the gravitational constant, ρ the density of air, C_d the drag force coefficient, A_f the vehicle equivalent frontal area and v the vehicle linear velocity. The model parameters for the benchmark vehicle are given in Table 5.2.

The road wheel torque can be calculated from the equation of motion, viz.:

$$T_w = J_w \frac{d\omega_w}{dt} + r_w F_d \tag{5.2}$$

where J_w, ω_w, and r_w are the wheel inertia, angular velocity and radius. Thus the torque and speed of the traction machine are converted by the transmission gear ratio and efficiency:

$$T_m = J_m \frac{d\omega_m}{dt} + \frac{T_w}{n_g \eta_g} \tag{5.3}$$

where ω_m and J_m are the traction machine rotor angular velocity and inertia respectively, n_g is the transmission gear ratio and the gearing efficiency, η_g, is estimated by considering the friction losses within the gearing [140].

The benchmark IPM machine model is built in a commercial FEA software and validated via the ORNL test data. Based on the machine torque and speed requirements, the machine phase current demand I_{ph}, voltage demand V_{ph}, and resulting efficiency are calculated. The machine voltage is constrained by the available DC-link voltage V_{dc} and the inverter space-vector modulation. The machine inverter losses are computed and show good comparison with the published ORNL experimental test data. As shown in Fig. 5.2 (a), the total electrical power P_T of the battery is the sum of the power demanded by the traction machine drive, P_{ele}, and the power consumed by the auxiliary components, P_{au}.

A representative lithium-ion battery pack having the same nominal voltage, rated pack energy and capacity, and similar characteristics is modelled to assess the battery voltage and current transients during representative vehicle driving or load cycles. The battery cell details are presented in Table 5.3. To obtain accurate parameters and open circuit EMF in the battery model, the battery cell is tested under the hybrid power pulse characterization test [146]. To satisfy the power-train target performance, 2112 such cells (a string of 96 cells in series and 22 such strings in parallel) form the complete battery package, Table 5.2. The benchmark vehicle power-train performance in terms of the efficiencies and power demands of each component are accurately calculated with this model. The model predictions for vehicle driving range and battery energy consumption rate show good agreement with the ANL experimental results for the same vehicle over a US06 driving cycle. From the model, the battery terminal voltage, i.e. the DC-link voltage, variation over repetitive US06 driving cycles, the battery open-circuit voltage and SoC versus range are illustrated in Fig. 5.3 (a). The corresponding battery current is shown in Fig. 5.3 (b). It can be noted that as the vehicle range increases, the vehicle DC-link voltage envelope reduces from 403V to 240V due to the battery SoC.

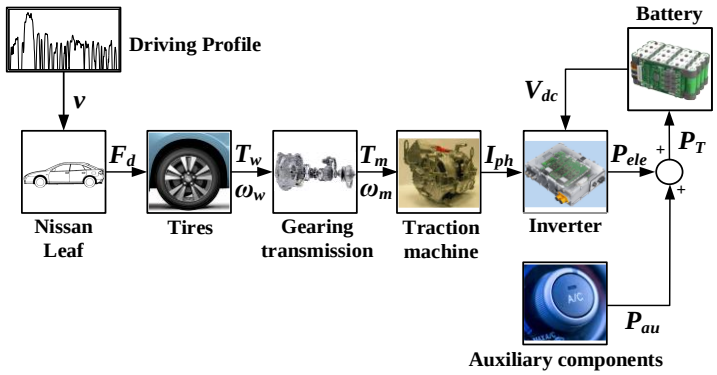

(a) Schematic showing backward-facing approach.

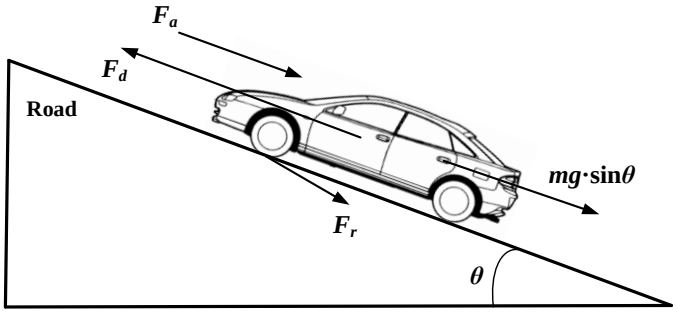

(b) Forces acting during the motion of the vehicle.

Fig. 5.2. EV simulation model.

Table 5.2. Bechmark vehicle model parameters.

Model parameter	Symbol	Value	Units
Curb weight	m	1521	kg
Gear ratio	n_g	7.9377	-
Density of air	ρ	1.225	$kg.m^{-3}$
Vehicle frontal area	A_f	2.27	m^2
Dag fore coefficinet	C_d	0.28	-
Wheel radius	r_w	0.315	m
Wheel inertia	J_w	0.164	$kg.m^2$
Machine rotor inertia	J_m	0.0347	$kg.m^2$
Gear efficiency	η_g	97	%

To minimize the DC-link voltage variation, the hybrid energy source combination of a SC system and batteries is investigated, as illustrated in Fig. 5.1 (a). Here, the SCs are installed in parallel with the batteries via converter 2 (converter 1 is not installed in this particular case study). Theoretically, the SC is sized to satisfy the vehicle maximum peak power demand and recapture all of the available regenerative braking energy. In this way, the number of SC modules, *N*, can be calculated based on the SC module specification:

$$N = Max\left(\frac{P_{\max}}{P_{sp}}, \frac{E_{\max}}{E_{sp}}\right) \tag{5.4}$$

where $P_{\max}$ and $E_{\max}$ are vehicle maximum peak power and maximum regenerative braking energy, P_{sp} and E_{sp} are the SC power and energy capacity per cell taken from SC module datasheet [147]. The SC bank design details are illustrated in Table 5.4.

To connect with a bidirectional boost converter, the maximum voltage of the SC terminal should be equal or less than the minimum DC-link voltage, which restricts the number of series-connected SC modules. In addition, battery and SC models, developed based on cell experimental dynamic assessments and validated by real road vehicle test data, are utilized to confirm the SC real-time performance within the physical limits:

$$i_{dis}(t) \le i_{dis\_\max} \tag{5.5}$$

$$i_{ch}(t) \le i_{ch\_\max} \tag{5.6}$$

$$V_{\min} \le V_b(t) \le V_{\max} \tag{5.7}$$

where $i_{ch}(t)$ and $i_{dis}(t)$ are the real-time SC charging and discharging currents, $i_{ch\_\max}$ and $i_{dis\_\max}$ are the maximum limits of SC charging and discharging currents, $V_b(t)$ is the real-time SC voltage, $V_{\max}$ and $V_{\min}$ are the upper and lower SC voltage limits.

The results for repetitive US06 driving cycles are shown in Fig. 5.4. Addition of the SCs extends the vehicle driving range by 15%, since SCs have higher charge and discharge efficiency than the lithium-ion batteries and the battery regulation is improved such that the minimum battery voltage is reached at a lower SoC. The SCs provide transient energy to the DC-link to compensate the peak power demand from the batteries, so that the battery

peak charging and discharging currents are significantly reduced, improving battery lifetime – the main reason for inclusion of SC systems.

From Fig. 5.4 it can be seen that the minimum DC-link voltage is still linked to that of the battery, i.e. 240 V, even with the SC system. Thus, the traction inverter and machine designs must take this into consideration. With this system, the DC-link voltage at 54 miles is 300V, Fig. 5. 4 (a). If the vehicle range of 54 miles was acceptable for repetitive US06 driving cycles, one could consider the addition of the SC to reduce the DC-link voltage variation from 403-240 V to 403-300 V. The trade-off then is the consideration of improved inverter and machine specifications versus the additional SC system. The 300 V point is not optimized, but simply taken as a design example.

Fig. 5.5 shows the benchmark vehicle power-speed requirements for the US06, UDDS and HFET driving cycles calculated via the vehicle model superimposed with the traction machine power-speed envelope as reported in [107] and via test data in [148]. The impact of these various driving cycles has been the source of many of the varied claims of vehicle range - typically quoted as anywhere between 92 miles, equivalent to UDDS driving, 78 miles, equivalent to HFFT driving, and 54 miles, equivalent to US06 driving [140, 141].

Published test data for the benchmark vehicle traction machine assumes a fixed DC-link voltage of 375 V [142] for which the machine can achieve the power-speed target performance of Fig. 5.5, although not continuously over the whole profile. Hence, some traction system performance is lost as the DC-link voltage reduces to the 240 V minimum. In this study it is assumed that the full machine power-speed target performance is required over the full battery SoC, as would be the case for repetitive US06 cycles, which is the most aggressive of the three cycles presented in terms of power, torque and speed. If this was the requirement, as is often presented by vehicle supplies, the power-train inverter power electronics and traction machine would have to be redesigned to ensure full performance at the minimum DC-link voltage.

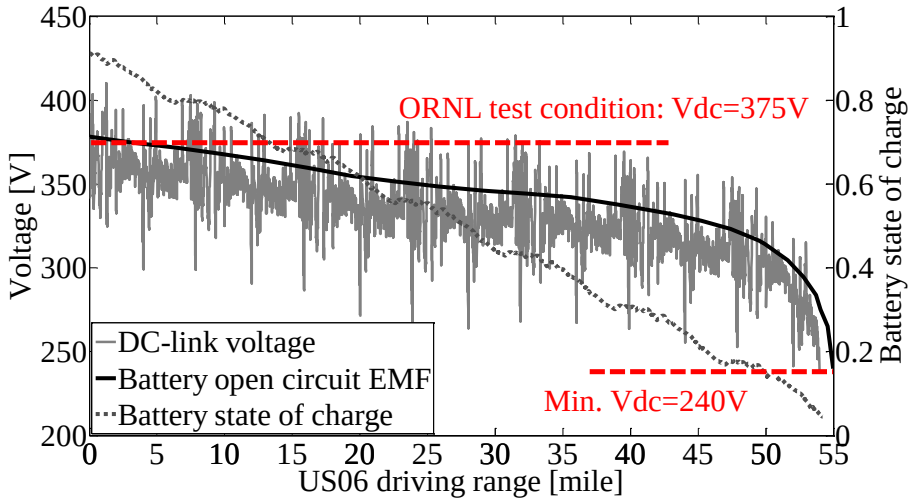

(a) Voltages and SoC

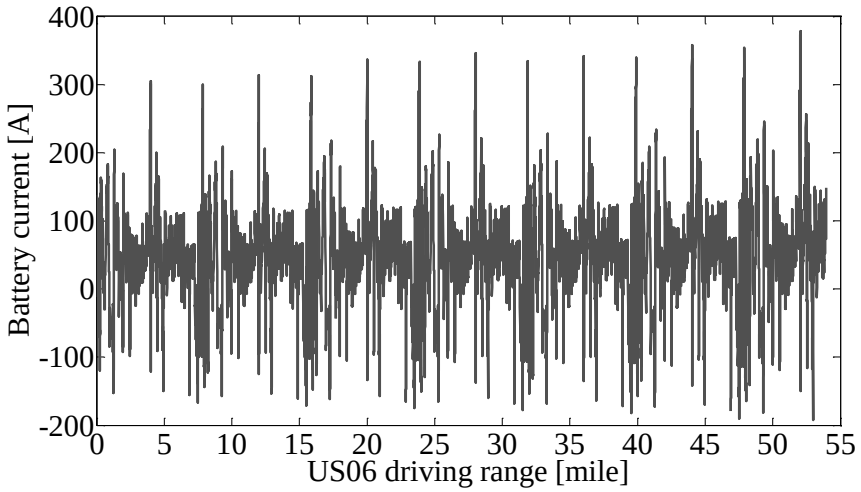

(b) Current

Fig. 5.3. Battery prediction for the benchmark vehicle

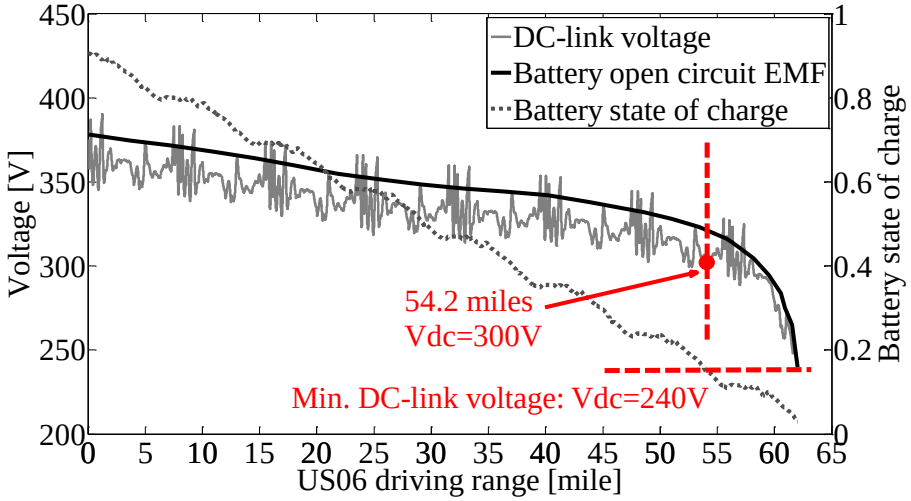

(a) Voltages and SoC

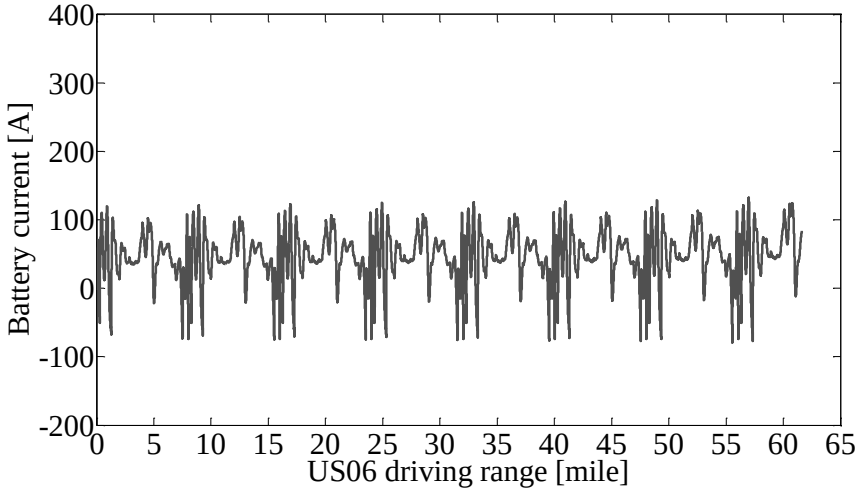

(b) Current

Fig. 5.4. Battery-SC combination

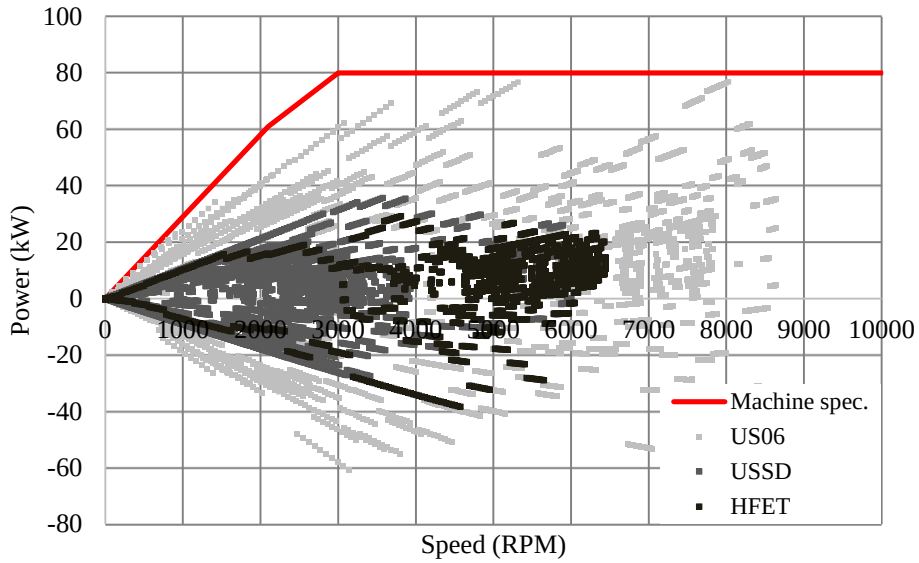

Fig. 5.5. Benchmark vehicle power-speed requirements for three driving cycles and published machine specification

Table 5.3. Battery Specification [146]

	Battery cell	Battery package
Max. voltage	4.2 V	403.2 V
Min. voltage	2.5 V	240 V
Energy	10.8 Wh	22.81 kWh
Peak power	45 W	95.04 kW
Mass*	47.5 g	100.32 kg
Volume*	17.55 ml	37.07 l

* Battery management system is not included.

Table 5.4. SC Design Details [147]

	SC bank
Size and connection	18 BCAP3000 cells in series as a module and 6 modules in series as a package
Max. voltage	288 V
Min. voltage	120 V
Max. current	430 A
Max. power	80 kW
Operating temp.	-40 to +65 ºC

5.4 Traction Machine Design Consideration

5.4.1 Impact of DC-Link Voltage Variation

The Nissan Leaf traction machine is studied as a benchmark machine in this chapter. This machine is modelled by FEA software and the FEA model validated by comparing the simulation results with the ORNL test results of [142], measured at a fixed DC-link voltage of 375V, as illustrated in Fig. 5.6 (a). The FEA and measured data show good correlation, hence the FEA analysis tool is used to investigate the IPM machine performance at lower DC-link voltage and temperature extremes.

From Fig. 5.3, it can be seen that there is a reduction in DC-link voltage of about 40% due to battery SoC and internal regulation, which will impact on the traction system performance. Fig. 5.6 (b) shows FEA simulation results illustrating the reduced torque-speed capability of the benchmark 8-turn IPM machine when operating at the minimum DC-link voltage of 240V. Here, the IPM machine capability above 3700 RPM is limited by the reduced supply voltage. Even an increase of the phase current magnitude does not resolve the problem and the machine is not capable of satisfying the torque and power target performance requirements, for example, at the machine high speed operation point of 10000 RPM, only 40% of the required torque can be realized. Essentially, the machine power is progressively inductively limited above 3700 RPM.

To analyze the brushless PM machine and assess the main design parameters impacting on the machine field-weakening capability, a linear electro-magnetic model coupled with a numerical direct search algorithm is developed. This model is implemented in a classical linear *d*-*q* two-axis approach, as presented by Equations (5.8) and (5.9) where R_s is the phase winding resistance, ω_e is the electrical angular speed, k_o is the back-EMF coefficient, γ and δ are the current excitation and load angles respectively, I_s is phase current, L is phase inductance, and the subscripts d and q represent d-axis and q-axis components. The example vector diagram is shown in Fig. 2.10 in Chapter 2. Although Equation (5.8) is the same as (2.35), it is repeated here for convenience and to aid the flow of discussion. From the linear model, the machine electro-magnetic torque can be expressed as [149]:

$$T_e = 3p\left(k_o I_s \cos\gamma + \frac{L_q - L_d}{2} I_s^2 \sin 2\gamma \right) \tag{5.8}$$

The machine torque consists of two contributions, the excitation torque due to the permanent magnets and reluctance torque due to the rotor magnetic geometry. For IPM machines, k_o, I_s and the saliency ratio (L_q-L_d) impact on the electro-magnetic torque performance below base speed. In the field-weakening region, the current excitation angle is increased towards 90 degrees with increasing speed. If the phase resistance is neglected, the machine maximum achievable speed is given by [149]:

$$\omega_{r\,(\max)} = \frac{V_s}{p\left|k_o - L_d I_s\right|} \tag{5.9}$$

From Equation (5.6), it can be noticed that if the machine k_o equals the product $L_d I_s$, the maximum achievable speed is theoretically infinite. Although the IPM magnetic circuit has a high degree of rotor saturation, this linear analysis is informative in illustrating design and operational trends, as was discussed previously in Chapter 2.

According to the FEA results, the benchmark IPM machine has been designed such that the base-speed (imposed by maximum phase voltage) is just below 7000 RPM. Hence, the machine requires high phase current to duty rated torque below base speed. The machine thermal continuous rating is specified as 80 kW at 7000 RPM. However, when operation of the traction machine at the minimum DC-link voltage of 240 V is considered, the reduced supply voltage impacts the field-weakening performance of the benchmark IPM machine. In this region, increasing phase current enlarges the difference between k_o and the $L_d I_s$ product, resulting in a fall-off in high speed torque, as observed in Fig. 5. 6 (b), i.e.: the traction system is progressively inductively limited, viz:

$$k_o < L_d I_s \tag{5.7}$$

and the target performance is not realized.

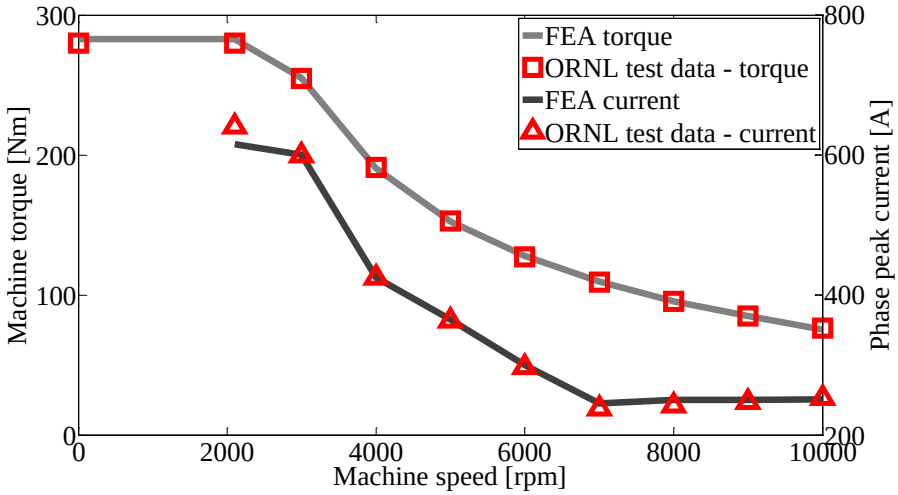

(a) Results for FEA model validation.

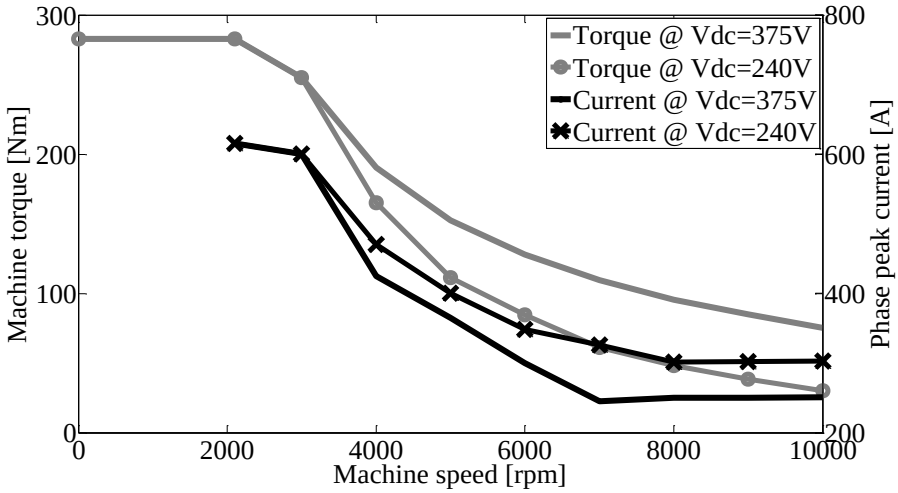

(b) Results of reference and minimum DC-link voltage.

Fig. 5.6. Performance results of benchmark IPM machine.

5.4.2 Machine Design Suitable for Nominal and Low Voltage

If the target performance is to be achieved, the benchmark machine has to be redesigned to satisfy the target performance at nominal and minimum voltage levels, thus the impact of a variable DC supply on machine and power electronics can be assessed.

In order to improve the machine high speed torque, the most straight forward way, based on Equation (5.8), is to increase the phase current. However, as previously discussed in Chapter 2, simply increasing the phase current may constrain the machine high speed performance. According to Equation (5.9), increasing the value of k_o or reducing the value of L_d will be required. Adding more magnet material (active length) enlarges the value of k_o but leads to an increase of back-EMF, which would results in a higher DC-link voltage requirement. Therefore, within the low voltage constraint, the machine can be designed with lower turns to achieve the output power of 80 kW during high speed operation. As an example design, and keeping the machine geometry and materials equitable, the number of winding turns per phase of the 8-turn benchmark machine is reduced until the target performance is realized. A 5-turn IPM machine achieves the target performance at the minimum DC-link voltage of 240 V, but a higher peak phase current of 960 A is required to satisfy the low speed torque.

When SCs are introduced in the energy storage system, the minimum allowable DC-link voltage can be increased to 300 V to keep the same driving range, as discussed in last section. In this case, the benchmark machine is redesigned with 7 turns and the peak phase current requirement is 685 A. Fig. 5.7 illustrates the phase current required to satisfy the target torque-speed characteristic for the (a) 5-turn machine and (b) 7-turn machine. Although the maximum peak current of the redesigned machines is higher than the benchmark machine, the Ampere-turns are approximately same. Therefore, both of the two redesigned machines are below the benchmark machine demagnetization limit. Further, the winding copper loss is similar for the 5, 7 and 8-turn designs (since the phase resistance is proportional to turns-squared), thus the thermal conditions are essentially equitable.

5.4.3 Investigation on SPM Topology

For the SPM machine, the direct and quadrature axis inductances are regarded as the same, which allows a full utilization of permanent magnet excitation torque component below base speed. In addition, since the PMs are mounted on the rotor surface, the PM flux can be weakened more directly by the armature flux in the field-weakening region, which may result in lower peak voltage requirement, comparing to IPM machines. Therefore, an SPM machine design is investigated as an alternative BLPM machine topology in this section.

In order to make it comparable, an example SPM machine designed in [104] is employed in this case study. Its performance is explored in terms of its field-weakening capability including DC-link voltage and temperature variations. Based on that, the machine is redesigned to satisfy the worst case of the DC-link voltage and temperature variations. The SPM machine is designed within the benchmark IPM machine dimensional constraints and power-train specifications and shares the same magnet volume, active axial stack length, airgap length and nearly identical stator lamination and machine mass with the benchmark IPM machine. Table 5.5 illustrates the mass comparison between the IPM and SPM machine.

For the SPM machine, the mechanical stress on rotor is an issue for high speed machines. Hence, a nonconductive sleeve is applied to protect the permanent magnet. However, the add-on sleeve increases the distance between magnets and stator winding, which requires additional turns to increase the back-EMF coefficient. In this study, the number of winding turns per phase is increased to 12- instead of the 8-turns of the benchmark IPM machine, which also allows the value of k_o close to the product of L_d and I_s for the SPM machine. The SPM machine torque and current versus speed characteristics, at the nominal and minimum DC-link voltage of 375V and 240V, are illustrated in Fig. 5.8, where it can be observed that the 12-turn SPM machine realizes the power and extended speed capabilities at the nominal DC-link voltage of 375 V. Additionally, with the increase of the number of winding turns, the requirement of machine peak current is reduced to 480A (compared to the IPM peak current value of 615A). However, because this SPM machine design only considered a fixed DC-link voltage of 375 V, the SPM machine design does not fully satisfy the vehicle

specification once the DC-link voltage drops to 240V, although it has a much better high speed operating performance than the benchmark IPM machine, Fig. 5.8.

As with the same redesign methodology with the IPM machine, in order to satisfy the target performance at nominal and minimum voltage levels, the example SPM machine is redesigned with a lower number of winding turns. Keeping machine geometry and materials the same, the number of winding turns per phase of the 12-turn example machine is reduced until the target performance is realized. An 8-turn SPM machine achieves the target performance at the minimum DC-link voltage of 240 V, but a higher peak phase current of 720 A is required to satisfy the low speed torque. When the minimum allowable DC-link voltage is increased to 300 V due to the implementation of SCs, the original SPM machine is redesigned with 10 turns and the peak phase current requirement is 585 A, which is closer to the benchmark IPM current rating. Although the maximum peak current of the redesigned machines are higher than the original 12-turn SPM machine, the Ampere-turns are approximately same. Therefore, both of the two redesigned machines are below the benchmark machine demagnetization limit. Further, the winding copper loss is similar for the 8, 10 and 12-turn SPM machines and the total loss is within the constraint of the benchmark IPM machine, thus the thermal conditions are essentially equitable.

Table 5.5. IPM and SPM Machine Mass Comparison.

	IPM machine	SPM machine
Iron (kg)	26.9	24.9
Copper (kg)	5.62	8.15
PM (kg)	1.895	1.895
Total (kg)	34.42	34.95

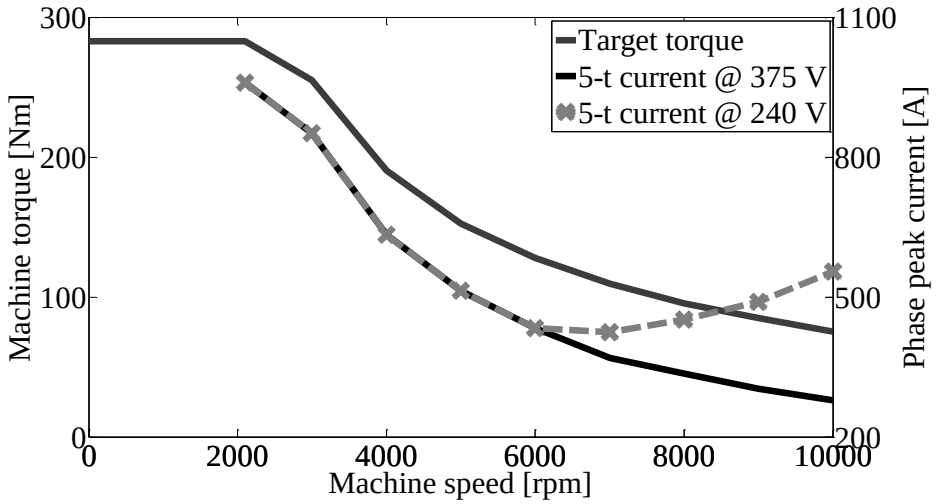

(a) Torque and current versus speed for 5-turn IPM machine.

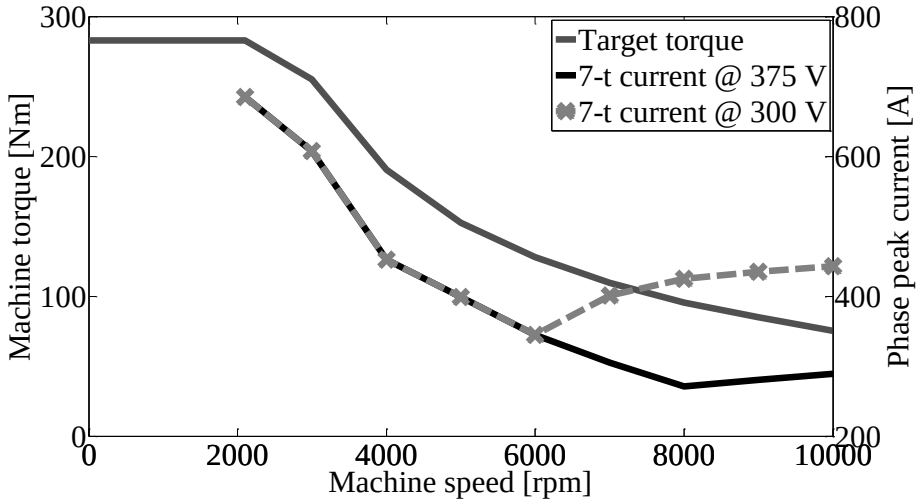

(b) Torque and current versus speed for 7-turn IPM machine.

Fig. 5.7. Results from machine design procedure.

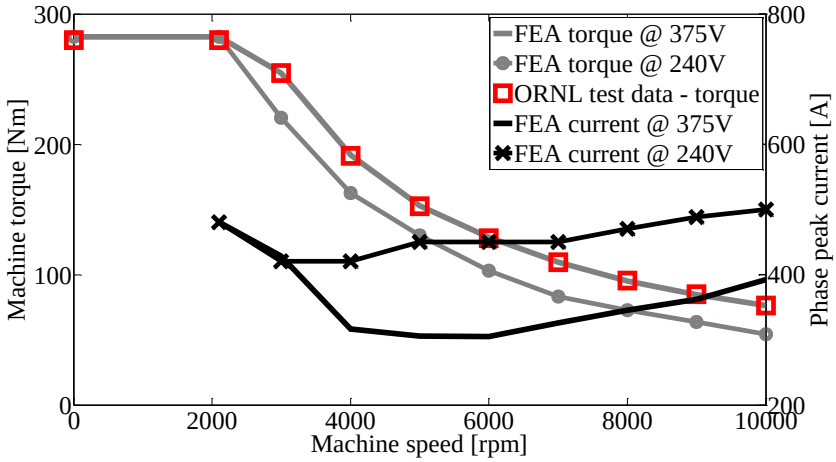

Fig. 5.8. Torque and current versus speed for 12-turn SPM machine.

5.4.4 Impact of Temperature Variation

Temperature variation is another issue impacting on the traction machine performance. Analysis of typical PM material B-H characteristics [138] shows that the magnet remanent flux-density for a sintered NdFeB grade, B_r, varies by typically 0.12% per degree C, which directly relates to a variation of k_o. According to Equation (5.8) and (5.9), lower magnet temperature (and hence higher k_o) improves torque-per-Ampere at low speed. However, a high value of k_o may impact on the machine field-weakening capability, which then requires some necessary adjustment (increase) of phase current magnitude, as illustrated by the results detailed in Tables 5.6 and 5.7 where it can be observed that the 8-turn benchmark IPM and 12-turn example SPM machine can satisfy the peak torque at 2100 RPM at both the voltage and temperature extremes. However, higher (than benchmark) current is required at the top speed operating point when the DC-link is 375 V and the temperature is -40 ^{o}C. The 10 kRPM operating point cannot be realized within the 240 V DC-link voltage constraint as discussed previously. Currents for the 5-turn and 7-turn IPM machine designs and 8-turn and 10 turn SPM machine designs at the temperature extremes are also given in Tables 5.6 and 5.7.

Table 5.6. IPM Machine Peak Current (A) Requirement at 2100 RPM and 10 kRPM for Voltage and Temperature Extremes

		2100 RPM			10000 RPM		
IPM machine		375V	300V	240V	375	300V	240V
8-turn	-40 ºC	535	-	535	393	-	177*
	120 ºC	615	-	615	354	-	303*
5-turn	-40 ºC	835	-	835	309	-	616
	120 ºC	960	-	960	278	-	555
7-turn	-40 ºC	596	596	-	321	492	-
	120 ºC	685	685	-	289	443	-

* Cannot realise torque target performance, quoted current is at maximum achievable torque.

Table 5.7. SPM Machine Peak Current (A) Requirement at 2100 RPM and 10 kRPM for Voltage and Temperature Extremes

		2100 RPM			10000 RPM		
SPM machine		375V	300V	240V	375	300V	240V
12-turn	-40 ºC	390	-	390	481	-	600*
	120 ºC	480	-	480	392	-	500*
8-turn	-40 ºC	590	-	590	435	-	747
	120 ºC	720	-	720	335	-	600
10-turn	-40 ºC	476	476	-	451	546	-
	120 ºC	585	585	-	360	440	-

* Cannot realise torque target performance, quoted current is at maximum achievable torque.

5.5 System Redesign

5.5.1 Basic Sizing Exercise

The 5-turn IPM design satisfies the torque and speed target performance at the nominal voltage of 375 V and minimum voltage of 240 V. However, a higher current rating inverter is required. The existing power-train system could be redesigned to ensure that the vehicle target performance is realized by inclusion of a DC/DC converter to maintain the DC-link voltage at 375V above the system base speed of operation. The benchmark system power-train of Fig. 5.1 (b) is therefore extended to incorporate a bi-directional step-up DC/DC converter, as illustrated in Fig. 5. 9.

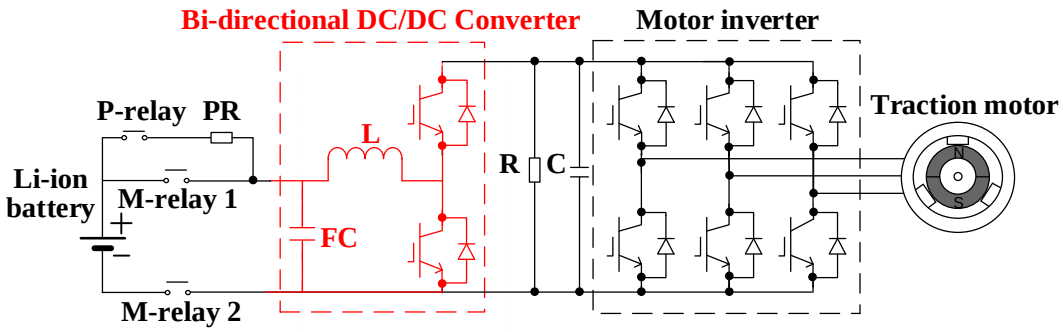

Fig. 5.9. Benchmark power-train [106] with additional bi-directional DC/DC converter. (P-relay: precharge relay, M-relay: system main relay, PR: precharge resistor, L: inductor, FC: filter capacitor, R: discharge resistor, C: smoothing capacitor)

The DC/DC converter rating is determined by the maximum battery voltage and maximum conversion current. The DC/DC converter and machine inverter requirements, considering worst case voltage and temperatures are summarized in Table 5.8 part (A), from which it is observed that a higher current rating inverter is necessary for the 5-turn and 7-turn designs. The benchmark inverter has 3x300 A IGBT dies per switch [143]. Hence, additional IGBT and diode dies will be paralleled to each switch to maintain the design margin. With the increase of device area, the driving board and the cooling infrastructure

will be scaled. In addition, the DC-link capacitors contribute substantially to the volume of the inverters. According to [150], the size of a capacitor is approximately proportional to the stored energy, the mass and volume of the benchmark inverter capacitors are hence scaled for a suitable design. Thus, to satisfy the system target performance at 240 V and 300 V, the inverter mass and volume will be increased as summarized in Table 5.8 (B). The inverter requirements and design estimation for the SPM machines are illustrated in Table 5.9 (A) and (B). It can be noted that for the same case of minimum voltage of 240V or 300V, the inverter for SPM machine requires less maximum current and hence less IGBTs than the IPM machine. However, since the back-EMF of SPM machine is higher than the IPM machine, it requires a DC-link capacitor with higher voltage rating.

The 2010 Prius DC/DC converter has a half bridge topology as required for this study, and it can be used as a reference. Considering the different current and voltage ratings, the main size difference will come from the inductor and cooling infrastructure. The Prius converter parameters are normalized into per unit form. Keeping the same maximum current ripple and switching frequency, the inductance can be specified. Since the benchmark system power rating is 3 times that of the Prius boost DC/DC converter, the cooling infrastructure size will be scaled approximately by 3 times. Therefore, based on the above estimation, the DC/DC converter design will be 8.14 kg and 6.41L, as detailed in Table 5.8 (C).

The case study in Section 5.3 indicates that introducing SCs could increase the minimum allowable DC-link voltage. For example, to keep the same driving range for repetitive US06 cycles, SCs are sized to satisfy vehicle maximum peak power and maximum regenerative braking energy. Hence, the 80 kW DC/DC converter is suitable for both 7-turn IPM machine and 10-turn SPM machine system. The SC, DC/DC converter and inverter mass and volume are summarized in Table 5.8 (D) for 7- turn IPM machine and 5.9 (C) for 10-turn SPM machine.

The trade-off in different system designs are explored here. For the benchmark 8-turn IPM machine and an example 12-turn SPM machine, reduction of the DC-link voltage significantly impacts on the high speed torque performance. To overcome the issues of voltage and temperature variations, three solutions are presented and compared for both

machine topologies. A 5-turn IPM and 8-turn SPM machine are designed to achieve the torque and speed target performance at both nominal voltage and minimum voltage of 240 V but it requires a traction inverter with higher current rating. Implementing a DC/DC converter ensures a controllable DC-link voltage but introduces an additional converter device and system complexity. Adding SCs increases the minimum allowable DC-link voltage to 300 V so that the benchmark traction drive does not have to be changed as drastically. However, it makes the traction system far more complicated, although the SCs are beneficial for battery lifetime. Further, the inverter for SPM machine requires less maximum current and hence less IGBTs than the IPM machine. However, since the back-EMF of SPM machine is higher than the IPM machine, it requires a DC-link capacitor with higher voltage rating, which increases the inverter mass and volume.

5.5.2 System Fault Considerations

Consideration must be given to fault scenarios, and their impact on the power-train design. If the traction machine inverter IGBT controls fail, the inverter will resort to an uncontrolled rectifier. In this case, if the vehicle is operating above base speed, the traction machine rectified back-EMFs would be higher than the battery terminal voltage, resulting in uncontrolled regenerative currents fed-back to the system. The worst case occurs when the machine is running at maximum speed and battery voltage is at minimum. Although mechanical relays are installed in the system, it is difficult for them to immediately switch off during fault, DC contactors also have the potential to weld close under such faults. In this circumstance, the vehicle could experience uncontrollable braking, leading to safety issues. In addition, the large transient currents could result in further damage to the power-train system in terms of battery, DC-link capacitor and traction inverter. Therefore, along with the system benefits discussed, an intermediate DC/DC converter between the battery and DC-link provides a blocking feature should there be a loss of inverter control when at high speed, field weakening operation. This allows the design of traction machines with higher maximum-to-base speed than would otherwise be the case.

Table 5.8. IPM Machine System Comparisons

(A) DC/DC Converter and Inverter Requirements		
IPM machine	DC/DC converter	Inverter
8-turn	403V; 333A	508V; 615A
5-turn	Not applicable	403V; 960A
7-turn	403V; 425A	445V; 685A
(B) Inverter Comparison for Different Machines		
	8-turn IPM	5-turn IPM	7-turn IPM
Voltage (V)	508	403	445
Current (A)	615	960	685
Number of IGBTs	18	30	24
Inverter capacitor			
Voltage (V)	600	500	550
Mass (kg)	1.96	1.36	1.65
Volume (L)	1.45	1.01	1.22
Complete inverter			
Mass (kg)	16.2	18.85	17.52
Volume (L)	14.04	16.47	15.25
(C) DC/DC Converter Design		
	2010 Prius [151]	System estimation
Power rating (kW)	27	80
Maximum voltage (V)	650	403
Maximum current (A)	243	333
Inductor (μH)	225	139
Mass (kg)	5.1	8.14
Volume (L)	4.8	6.41
(D) An Example Bat-SC Hybrid System		
	SC	DC/DC	Inverter
Mass (kg)	85.2	8.14	17.52
Volume (L)	0.08	6.41	15.25

Table 5.9. SPM Machine System Comparisons

(A) DC/DC Converter and Inverter Requirements			
IPM machine	DC/DC converter	Inverter	
12-turn	403V; 333A	890V; 480A	
8-turn	Not applicable	593V; 747A	
10-turn	403V; 425A	742V; 585A	
(B) Inverter Comparison for Different Machines			
	12-turn SPM	8-turn SPM	10-turn SPM
Voltage (V)	890	593	742
Current (A)	480	747	585
Number of IGBTs	18	24	18
Inverter capacitor			
Voltage (V)	1100	700	900
Mass (kg)	6.59	2.67	4.41
Volume (L)	4.87	1.97	3.26
Complete inverter			
Mass (kg)	20.83	18.84	18.65
Volume (L)	17.46	16.01	15.85
(C) An Example Bat-SC Hybrid System			
	SC	DC/DC	Inverter
Mass (kg)	85.2	8.14	18.65
Volume (L)	0.08	6.41	15.85

5.6 Conclusions

DC-link voltage and temperature variations are critical issues when designing an electric vehicle (EV) traction system. However, systems are generally reported at fixed voltage and temperature and may not therefore be fully specified when considering the variation of these parameters over full vehicle operating extremes. The Chapter presents an assessment of electric vehicle power-train options based on a commercial benchmark vehicle system. Results from a vehicle power-train model, including the benchmark IPM traction machine, are presented to illustrate the power-train traction torque- and power- speed requirements. Since the vehicle DC-link is directly connected to the battery, the DC-link voltage varies with the battery terminal voltage during driving load cycles. When the benchmark IPM machine operates at the minimum DC-link voltage, the machine torque can only reach 40% of the required value during high speed operation at 10 kRPM. The vehicle power-train is then modified with the inclusion of a DC/DC converter between the vehicle battery and DC-link to maintain the traction system DC-link voltage near constant. A SC system is also considered for improved system voltage management. As an alternative machine topology, 5-turn and 7-turn IPM designs are assessed against the target performance requirements, and under the variable DC-link voltage conditions. In addition, temperature variation impacts the traction machine, which results in higher back-EMF and current during high speed operation. Based on the voltage and temperature variation, the DC/DC converter and inverter requirements are presented. An example SPM machine, as an alternative traction machine topology, is investigated to satisfy the target performance. Although the SPM machine requires less maximum current and hence less IGBTs than the IPM machine, the back-EMF of SPM machine is higher than the IPM machine, which requires a DC-link capacitor with higher voltage rating and the inverter mass and volume. Finally, the faulted operation of electric machine drive is discussed. The most appropriate solution is the 8-turn IPM design with a DC/DC converter providing fault protection and stabilizing the DC-link to 375 V, thus allowing full performance from a lower current rated traction inverter.

Chapter 6

Brushless Permanent Magnet Machine Design for Electric Vehicles

6.1 Introduction

With the implementation of power electronic converters and modern controls, AC machines have dominated the EV traction machine market [152]. So far, induction machines and brushless permanent magnet (BLPM) machines are employed by the majority of EV manufactures [153]. Compared to induction machines, BLPM machines have inherent advantages of high power density and high efficiency due to the PM excitation.

As discussed previously, BLPM machines can be classified as two types of rotor topologies:

(i) the interior permanent magnet (IPM) rotor, where magnets are buried within the rotor body, and

(ii) the surface-mounted PM (SPM) rotor , where magnets are mounted on the rotor surface.

Generally, both of the two topologies can achieve vehicle traction characteristics and both have merits and weaknesses. However, currently, IPM machines are considered to be the more favored choice by the HEV and EV manufactures, such as Honda Accord, Hyundai Sonata, Toyota Prius and Nissan Leaf [154]. In addition, most of the existing literature deem that IPM machines are more appropriate for field-weakening operation, because the IPM rotor is more robust with the magnets embedded in the rotor lamination [152, 155] and the salient rotor structure provides additional reluctance torque [156, 157] and higher equivalent *d*-axis inductance [158, 159], compared with SPM topologies.

Corresponding to the weaknesses of SPM topologies, solutions have been introduced to improve the SPM machine field-weakening capability and achieve wide speed ranges of constant power operation. For SPM machines, mounting of the rotor magnets leads to issues with mechanical integrity, since the magnet material yield strength cannot be guarented, leading to premature failure at speed. To overcome such mechanical issues, high-strength retaining sleeves can be used to retain the rotor magnets [160, 161], although this may induce additional eddy-current losses and manufacturing complexity. Although there is essentially no reluctance torque contributed by SPM machines due to the same inductance on the direct- and quadrature-axes, SPM machines have higher PM utilization in the constant torque region, which may compensate for some of the loss of saliency torque production [162]. According to [158, 159, 163], the low inductance value is the principal reason that SPM machines are generally considered to have poor field-weakening capability. However, the work presented in [163] proposes a SPM machine design with fractional slot concentrated windings, the results from which indicate that for the same magnet flux-linkage, replacing distributed windings with fractional slot concentrated windings (FSCW) will significantly increases the *d*-axis inductance. In addition, the authors in [164] also proved that the FSCW SPM machine is a suitable candidate for EV applications. Alternatively, distributed windings in deeper slots can also increase the machine inductance and hence achieve wide ranges of constant power operation, because the deeper slots allow an increase of number of winding turns while maintaining winding resistance. With this idea, an example SPM is designed with the same constraints of a benchmark IPM traction machine [162], which shows that brushless PM machines do not have to be salient to achieve traction characteristics.

The discussion above indicates that properly designed SPM machines can be as suitable as IPM machines for traction applications, so a number of authors have compared the performance between IPM and SPM traction machines. A comparison between a SPM machine with concentrated windings and an IPM machine with distributed windings is carried out in [165]. The two machines in this study can reach same rated power within a given inverter rating, but the IPM machine has better overload capability. Additionally, the

loss behaviors of the two machines at low and high speed are different. However, although the two machines have the same volume, the winding configuration and the quantity of PM material used between the two machines are different, with a higher magnet volume for the IPM machine, which results in conclusions that cannot be deemed general. In [166], IPM and SPM machines with comparable mass and volume are designed to meet the same traction specifications and both the machines use FSCW configurations. The comparison of the two machines indicate that the IPM machine design requires lower magnet mass but needs higher phase current for the same peak power. The efficiency values of the two machines are close, but the components of each machine are different. In addition, authors in [162] compared distributed winding IPM and SPM machines for the same EV specifications and drew similar conclusions. Moreover, weight and cost comparisons between high speed IPM and SPM machines are investigated in [167], indicating that the two machines have similar torque and power density but the SPM machine cost more than the IPM machine due to the rotor sleeve and higher PM volume required. Performance, in terms of losses and temperature rise, are compared for a SPM machine and an IPM machine in [168], showing that the total loss of the IPM machine is higher than the SPM machine but the rotor temperature rise of the SPM machine is higher than the IPM machine due to eddy-current loss and heat dissipation in the SPM rotor sleeve. Further, demagnetization comparison between IPM and SPM traction machines is reported in [169], showing that PMs with higher coercive force have to be chosen for SPM machines to ensure the same demagnetization withstand as IPM machines. However, the literature reviewed above mainly focus on the comparison of machine output performance, in terms of torque, power, overload, loss, thermal and demagnetization, which is not comprehensive. Since both IPM and SPM machines have some degree of nonlinearity and are affected by magnetic saturation and armature reaction, the machine on-load terminal voltages are usually distorted. Such voltage distortion may lead to a significant difference between peak and fundamental values of phase voltage and give rise to torque ripple [170]. The voltage and torque distortion comparison between IPM and SPM machines have not previously been reported.

For both IPM and SPM traction machines, sinusoidal phase current is desired to enhance machine torque performance, hence power electronic inverters with vector control methods are commonly employed. In this case, converter nonlinearity from PWM dead-time and DC-link voltage disturbance may induce phase voltage distortion, as summarized in [171]. However, the main voltage distortion should be from the machine side. Zhu and Wu et al [171-173] have published a series of papers to explain the voltage distortion mechanism and the influence on the machine torque speed characteristic. The studies in [171, 172] attributed the IPM machine voltage distortion to local magnetic saturation caused by machine geometry. The study in [173] ascribed the SPM machine voltage distortion to the local magnetic saturation in the stator tooth-tips. However, at different rotor positions, the PM flux direction is either the same or different to the armature flux direction. Hence, interaction of the PM flux and armature flux will distort the global machine magnetic field, which is one reason for PM machine voltage distortion, but this issue has not been previously studied. In this Chapter, IPM and SPM machines, with same design constraints and equal active parts, are compared and analyzed, with particular emphasis on the comparison of phase voltage distortion. Based on the trade-off of the IPM and SPM topologies, a BLPM machine topology with pole shoe rotor is proposed. This rotor topology is common in industry for machines designed for constant torque-speed characteristics, but has not been previously considered for machines designed for traction torque-speed characteristics. The Nissan Leaf IPM traction machine is employed as the reference benchmark machine.

6.2 Nissan Leaf IPM Machine

6.2.1 Machine overview

The Nissan Leaf electric vehicle utilizes an 8-poleIPM traction machine, the cross section of which is illustrated in Fig. 6.1. Each pole of the rotor is comprised of three magnets with a delta-shaped arrangement. The Nissan Leaf machine design adopts a full pitched, integer slot, single layer, distributed winding with two neutral points joined via an interconnecting link to ease manufacture as opposed to any electrical additionality. There are 2 coils per pole connected in series and then the 4 are branches connected in parallel to form each phase. The machine parameters are detailed in Table 6.1. Note that the nominal DC-link voltage of 375 V and the maximum peak phase current of 615 A are used as the design constraints, since they impact on the machine power electronic converter size and rating.
The target torque speed performance and efficiency map of the Nissan Leaf Machine are shown in Fig. 6.2. Four key operating points of the torque-speed characteristic are highlighted and used for subsequent machine assessment. The first operating point is 280Nm at 2100 RPM and 280 Nm, which is the maximum speed point to achieve maximum torque. The second operating point of 254.65 Nm at 3000 RPM, is when the machine reaches the specified peak nameplate power of 80kW. The third operating point of 109 Nm at 7000 RPM is the continuous thermal rating point. According to the Oak Ridge National Laboratory experimental tests, the machine is capable to continuously operating at this point with the stator reaching an upper temperature of 135 ^{o}C. The fourth operating point of interest is 76.4 Nm, 80kW, at 10000 RPM, which is the maximum speed specification.

6.2.2 Machine model and validation

The authors in [175] have created an electromagnetic model of the Nissan Leaf machine in a commercial FEA software JMAG based on the published machine details. In this Chapter, the Nissan Leaf machine model is rebuilt in another commercial FEA software, ANSYS MAXWELL and the simulation results of [175] confirmed. Since the Nissan Leaf machine

magnet material is not published, different types of neodymium-iron-boron (NdFeB) are selected to fit in the published machine performance. In this case study, N28AH from Arnold Magnetics [138] is used as the PM material in the model, since this comfirms the back-EMF test data and measured phase currents.

To further validate the FEA model, the static DC phase current excitation results from the FEA model are compared with the locked rotor test results from Oakridge and show good agreement. Further, the comparison of FEA and measured torque and phase current over the specified torque-speed characteristic show good agreement, as illustrated in Fig. 6.3.

The maximum error between the Oakridge published experimental results and FEA simulation results is within 5%, which is acceptable considering the inevitable experimental and computational uncertainties.

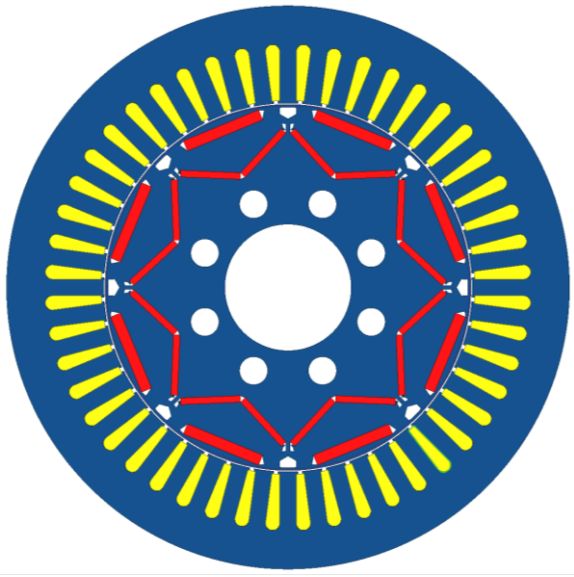

Fig. 6.1. Nissan Leaf IPM machine cross section.

Table 6.1. Details of Nissan Leaf IPM Machine [154].

Description	Quantity
Outer diameter of stator (mm)	200
Inner diameter of stator (mm)	131
Stator stack length (mm)	151
Number of stator slots	48
Winding distribution	Full pitch, single layer
No. of turns per phase	8
Outer diameter of rotor (mm)	130
Inner diameter of rotor (mm)	45
No. of poles	8
Large magnet dimensions (mm)	3.79 × 28.85 × 8.36
Small magnet dimensions (mm)	2.29 × 21.3 × 8.34
Skew angle (degrees mech.)	3.75
Maximum torque (Nm)	280
Rated power (kW)	80
Top speed (RPM)	10000
DC-link voltage (V)	375

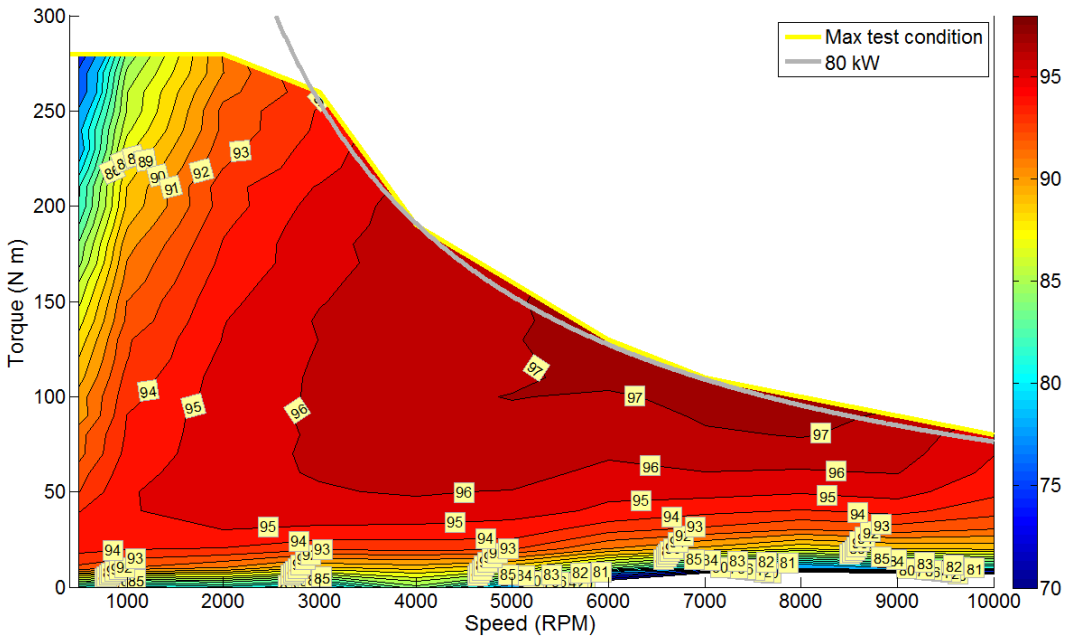

Fig. 6.2. Efficiency map of Nissan Leaf Machine [174].

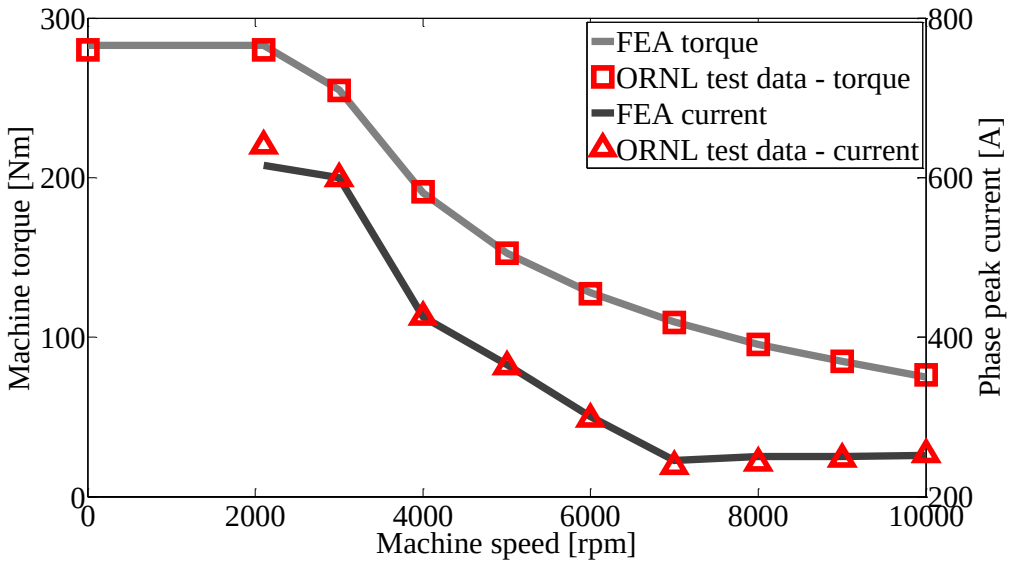

Fig. 6.3. Results for FEA model validation.

6.3 Example SPM Machine

Most of the existing literature deems that machines must be salient if they have to realize a traction torque-speed characteristic, but this is theoretically incorrect, as discussed in Chapter 2. The authors in [162] presented an example SPM machine which is designed within the design constraints of Nissan Leaf IPM machine, showing that machine saliency is not necessary for traction torque-speed characteristic. However, the authors in [162] mainly focused on the machine design and torque-speed comparison and no attention was paid to the voltage distortion issues. This section compares the difference of on-load voltage distortion and torque ripple between IPM and SPM machines and investigates the mechanism.

6.3.1 SPM Machine details

To make the two designs comparable, the SPM machine keeps the same active axial length, mechanical air-gap length, air-gap mean diameter, magnet volume and stator winding scheme. Compared to the IPM machine, a non-conductive sleeve is required to maintain mechanical strength at high speed operation for the SPM machine, hence the mechanical distance between the rotor surface and the stator has to be increased for the SPM machine design. To achieve the target torque-speed performance, the SPM machine is designed with higher winding turns than the IPM machine. This feature, in addition to the larger magnetic airgap, tunes the k_o/L_dI_s ratio required for field weakening operation, as discussed in Chapter 2. The example SPM machine has 12 turns per coil instead of 8 turns for the IPM machine. To maintain equitable thermal performance, deeper stator slots are applied to the SPM machine, which leads to a 7% increase of the stator outer diameter compared to the IPM machine stator. Again, the machine model is rebuilt in ANSYS MAXWELL and it confirms the simulation results reported in [162]. Fig. 6.4 shows the cross section of the SPM machine and Table 6.2 details the design parameters.

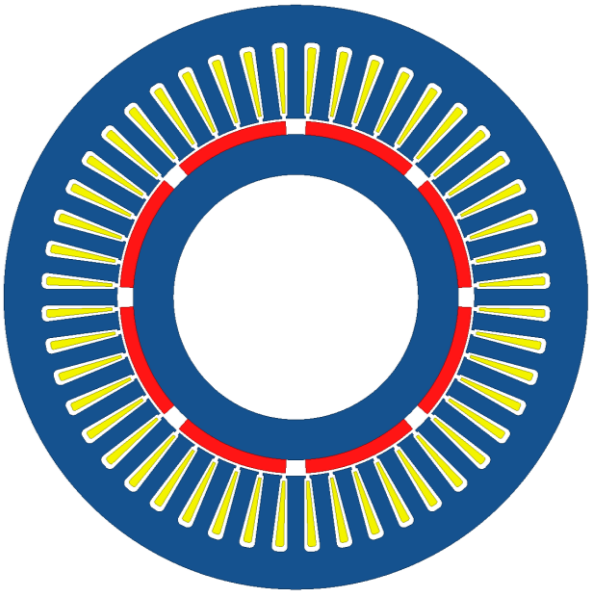

Fig. 6.4. Example SPM machine cross section.

Table 6.2. Details of the Example SPM Machine [162].

Description	Quantity
Outer diameter of stator (mm)	214
Inner diameter of stator (mm)	131
Stator stack length (mm)	151
Number of stator slots	48
Winding distribution	Full pitch, single layer
No. of turns per phase	8
Outer diameter of rotor (mm)	130
Inner diameter of rotor (mm)	93
No. of poles	8
Magnet dimensions (mm)	3.79 × 28.85 × 8.36
Skew angle (degrees mech.)	3.75
Maximum torque (Nm)	280
Rated power (kW)	80
Top speed (RPM)	10000
DC-link voltage (V)	375

6.3.2 Comparison Study of IPM and SPM Machine

The FEA simulation results of the SPM machine are illustrated in Fig. 6.5. It can be seen that the SPM machine achieves the same torque-speed characteristic of the benchmark IPM machine. However, to satisfy the maximum torque, a peak phase current of 615 A required for the IPM machine while the SPM machine only requires 495A, which is beneficial in terms of the machine and power electronic converter design. Note, at this operating point, the SPM machine fully utilized the permanent magnet torque while the IPM machine only has a utilization of about 64 %. At high speeds, the SPM machine requires a larger current magnitude than the IPM machine to reach the target performance, which results in higher copper loss. However, SPM machine has less iron loss than the IPM machine, leading to approximately the same total loss and hence efficiency.

Therefore, it is not necessary for PM machines to be salient in order to achieve traction torque-speed characteristics. The machine field-weakening capability is determined by the ratio of the back-EMF coefficient, *d*-axis inductance and stator phase current. The saliency ratio does not contribute to extended speed capability. Although the machine saliency brings about additional salient torque, it loses utilization rate of the permanent magnet due to the current excitation angle.

For traction applications, sinusoidal phase current is desired to enhance machine torque performance and power electronic converters employing vector control method are commonly used for traction machine supply. However, due to the machine nonlinearity and field distortion, the machine terminal phase voltage is distorted, which may introduce additional difficulties for vector control. In addition, the voltage distortion harmonics also cause torque ripple [170]. Fig. 6.6 compares the voltage distortion level and torque ripple of the IPM and SPM over the speed range from 2100 to 10000 RPM. It can be seen that the IPM machine has more significant torque ripple than the SPM machine and the voltage distortion and torque ripple level of both machines increase with the current excitation angle, i.e. as the machine progresses into the field weakening region. Compared to the IPM machine, the SPM machine has lower voltage distortion in the low speed region, but higher distortion in the high speed region. Here, voltage distortion is defined as peak fundamental

phase voltage divided by peak terminal phase voltage; torque ripple is defined as peak-peak torque divided by average torque and expressed as a percentage of average torque.

To explain the voltage distortion phenomenon, the maximum torque point at 2100 RPM and the top speed point at 10000 rpm are analyzed in detail for both machines. For the IPM machine, Fig. 6.7 compares the phase voltage with open circuit back-EMF at 2100 RPM and 10000 RPM. It can be noticed that both the two phase voltage waveforms are distorted, but obviously the distortion at 10000 RPM is more severe than at 2100 RPM. The voltage distortion causes the peak voltage to be higher than the fundamental value. Note, the peak voltage at 10000 RPM exceeds the DC-link voltage limit, which may introduce difficulty for vector control, leading to some overmodulation of the power electronic converter.

SPM machine has similar issue as IPM machine, i.e. phase voltage at 10000 RPM suffers more significant distortion than it at 2100 RPM, as illustrated in Fig 6.8. At 2100 RPM, SPM machine voltage is only slightly distorted from the fundamental waveform. However, at 10000 RPM, although the SPM keeps the peak phase voltage with the DC-link voltage limit, the voltage distortion ratio is twice that of the IPM machine.

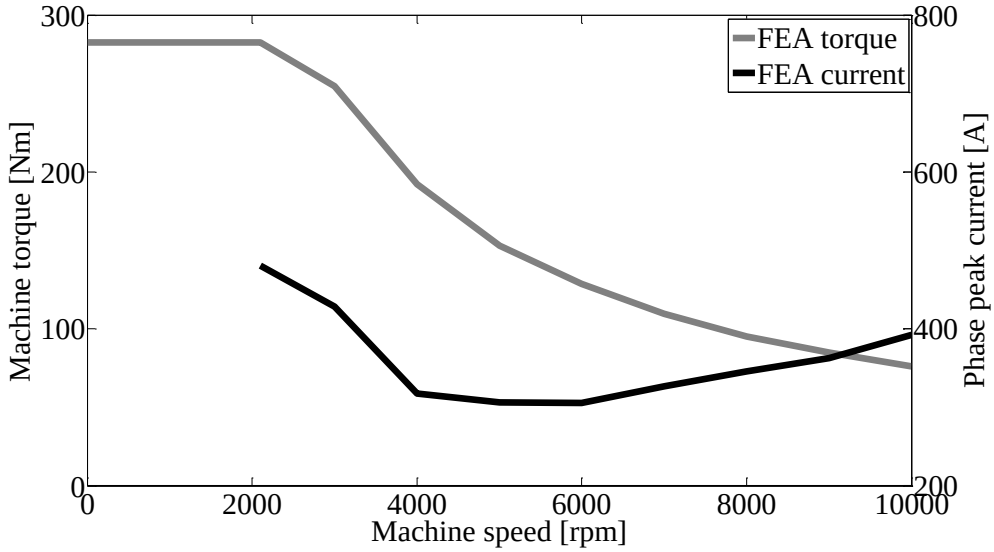

Fig. 6.5. Torque and current versus speed for the example SPM machine.

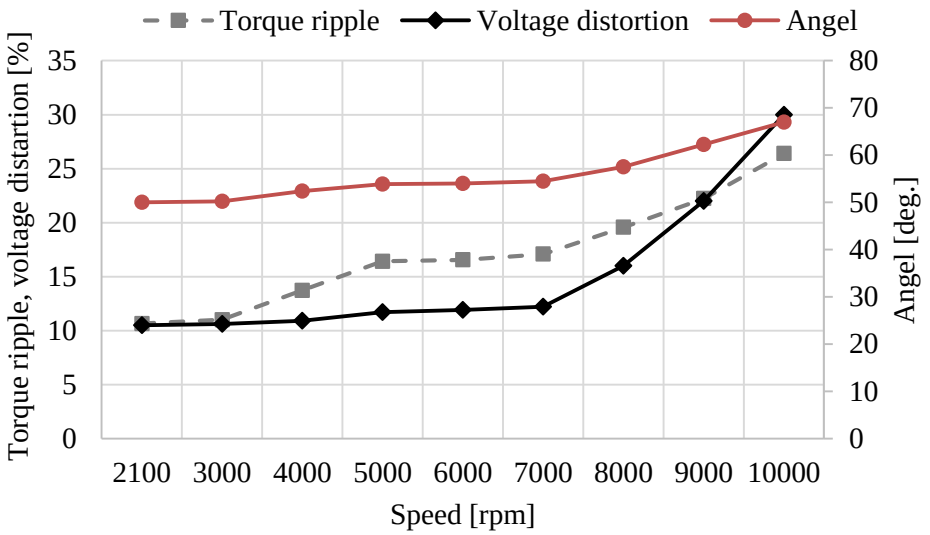

(a) IPM machine.

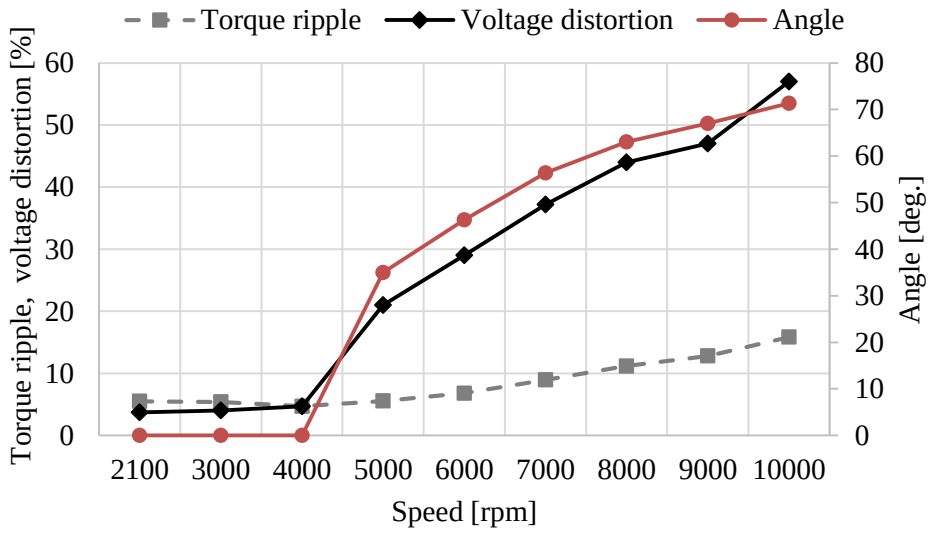

(b) SPM machine.

Fig. 6.6. Voltage distortion and torque ripple of the IPM and SPM machine designs.

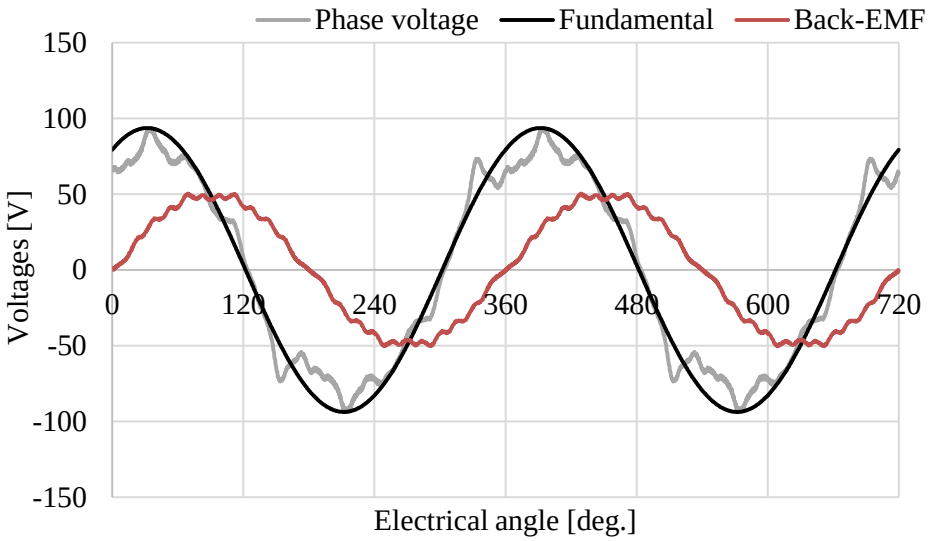

(a) 2100 RPM.

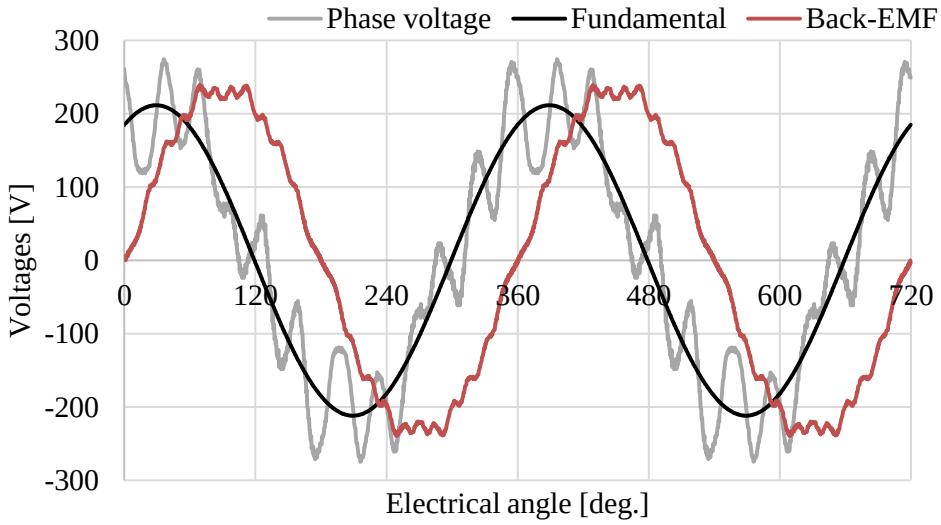

(b) 10000 RPM.

Fig. 6.7. IPM machine phase voltage and open circuit back-EMF.

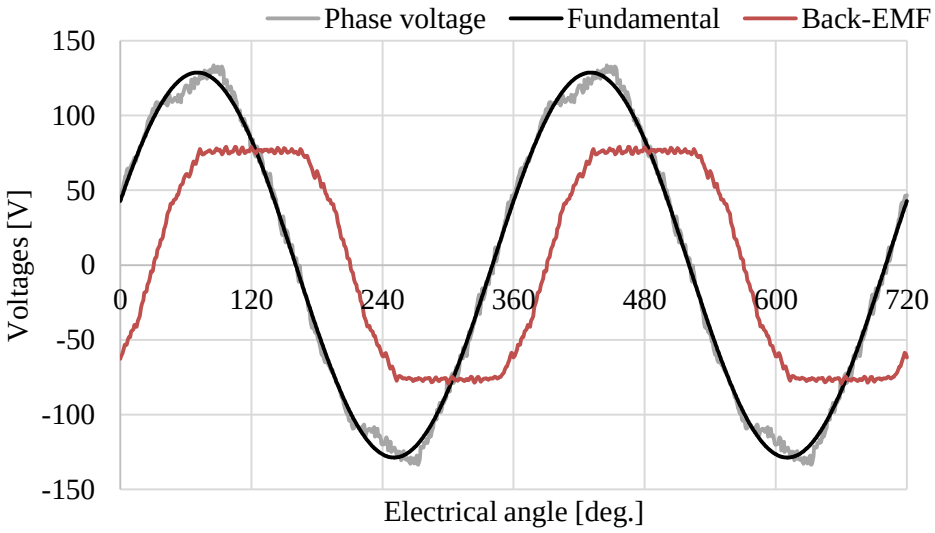

(a) 2100 RPM

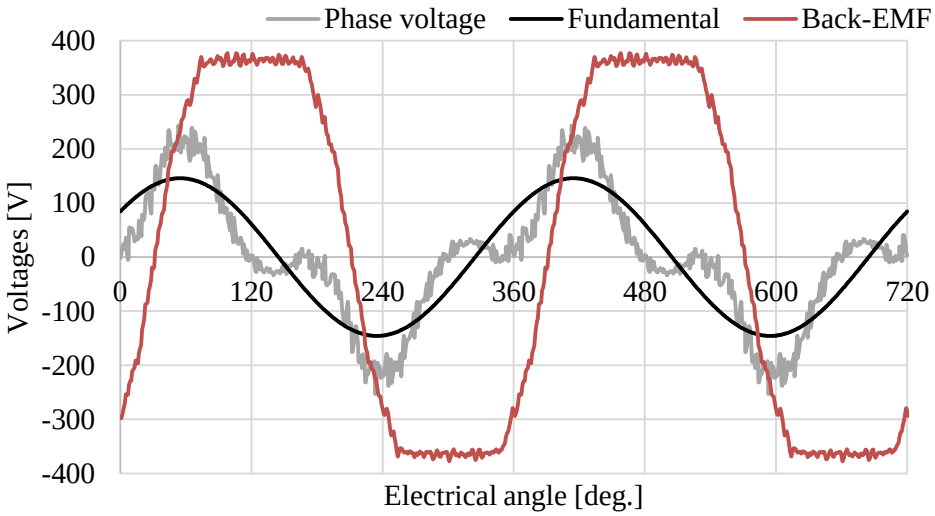

(b) 10000 RPM

Fig. 6.8. SPM machine phase voltage and open circuit back-EMF.

Zhu, Wu et al [171-173] attributed the FSCW IPM machine voltage distortion to the local magnetic saturation caused by machine geometry and FSCW SPM machine voltage

distortion to the local magnetic saturation in stator tooth-tips, which reveals one of the reasons for FSCW machines. However, the reasons behind the voltage distortion for distributed winding IPM and SPM machines are not studied and compared. The armature reaction caused by the interaction of the PM flux and armature flux should be another reason, but it was not considered by Zhu et al [171-173]. To explain the mechanism, the SPM machine with simple rotor structure is studied as an example. A simplified machine diagram under different current excitation angles γ, e.g. 0 and 71 deg., as illustrated in Fig. 6.9, where dashed lines represent the armature flux lines and arrows on the PM represent the PM pole direction of magnetization. When γ = 0 deg., the armature poles are totally unaligned with the PM poles and hence the armature field is perpendicular to the PM field, which minimizes the armature field impact on the PM field. The flux-linkage per phase can be nearly sinusoidal, as shown in Fig. 6.10 (a). However, some armature flux still passes through the two edges of the PM, which results in one side of the PM flux strengthened and the other side weakened. As shown in Fig. 6.10 (a), one side of the flux density is weakened and the other is strengthened, which causes the slight phase voltage distortion in Fig. 6.8 (a). When γ = 71 deg., the machine operates in field-weakening region, and the relative electrical position of armature pole and PM pole is shifted by 71 degrees. Hence most of the PM surface is faced to the armature pole. In this case, since the armature pole and PM pole have opposite directions, both the armature flux and PM flux are weakened. As illustrated in Fig. 6.10 (b), most part of the PM flux density is reduced, compared to the no-load or open circuit case. The machine phase flux-linkage curve follows a similar pattern of increasing and decreasing of PM flux density, which causes the phase voltage to be significantly distorted, as illustrated in Fig. 6.8 (b). The FEA simulation results tie up with the armature reaction mechanism, indicating that the SPM machine phase voltage distortion is mainly cause by the armature reaction and the interaction of the PM and armature flux.

Besides the reason discussed above, as the studies in [171, 172] have presented, the local magnetic saturation caused by the geometric feature of IPM rotor is another reason for IPM machine phase voltage distortion. When γ = 67 deg., as is the case of the IPM machine operating at 10000 RPM, then, due to the low permeance of PM material, a part of the flux

is forced to circulate through the rotor ribs, which enhances the PM flux. In addition, the leakage flux between adjacent magnets impacts the airgap flux direction and the interaction of the PM and armature flux tend to weaken the field, as illustrated in Fig. 6.11. Thus, all of the three reasons cited above cause machine flux-linkages distortion and hence lead to the phase voltage distortion in the field-weakening region, as shown in Fig. 6. 12.

Additionally, as the speed increases from 2100 to 10000 RPM, the current angle is raised from 44 to 67 deg., and hence more current is assigned for field-weakening, leading to a reduction of the *q*-axis flux-linkage. However, the magnetic saturation in the *d*-axis is also reduced, resulting in the increase of *d*-axis flux-linkage, as illustrated in Fig. 6.13. Further, with the increase of current angle, the reduction of *q*-axis flux-linkage leads to less magnetic saturation. Hence, the *q*-axis inductance is enlarged and the difference between the *d*- and *q*-axis inductance, i.e. the saliency ratio, is significantly increased, as shown in Fig. 6.14. Alternatively, the increase of machine saliency ratio further increases the current angle to achieve the torque requirement. With the increase of machine saliency ratio and hence the current angle, the saturation in the rotor rib is more severe, which leads to increased fluctuation of *q*-axis inductance, contributing more significant phase voltage distortion and torque ripple, as have been reported in [171]. Therefore, to improve the IPM machine voltage distortion and torque ripple, the machine saliency ratio has to be reduced, although it will decrease the reluctance torque contribution – a design conundrum.

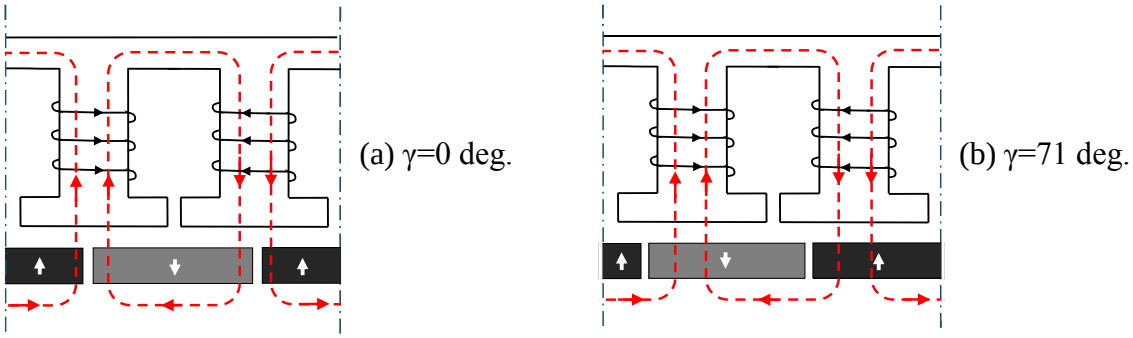

Fig. 6.9. Simplified brushless PM machine diagram.

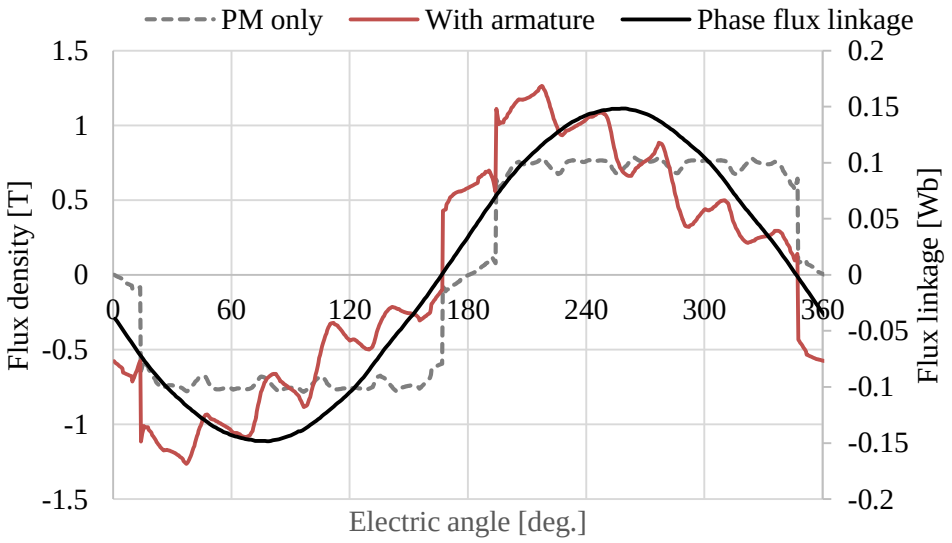

(a) 2100 RPM (angle = 0 deg.).

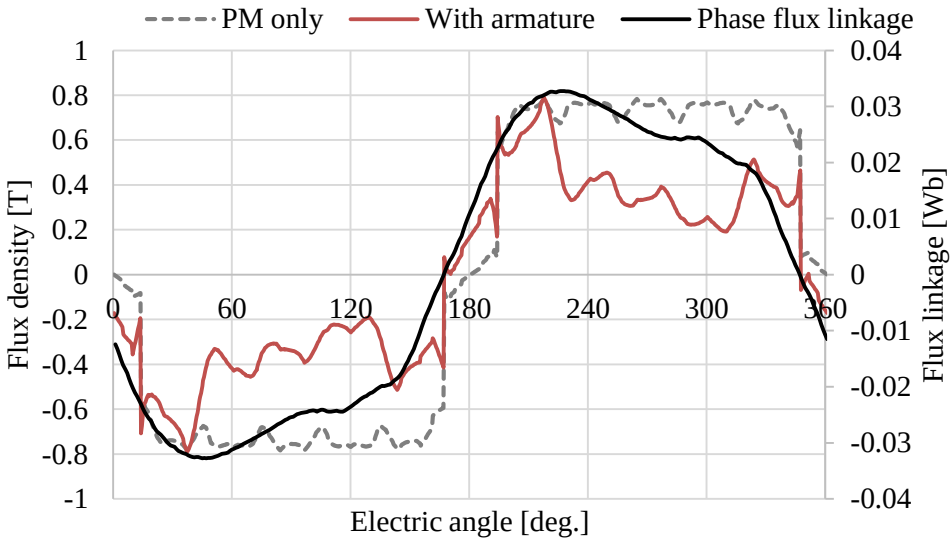

(b) 10000 RPM (angle = 71 deg.).

Fig. 6.10. Airgap flux density and phase flux linkage for SPM machine.

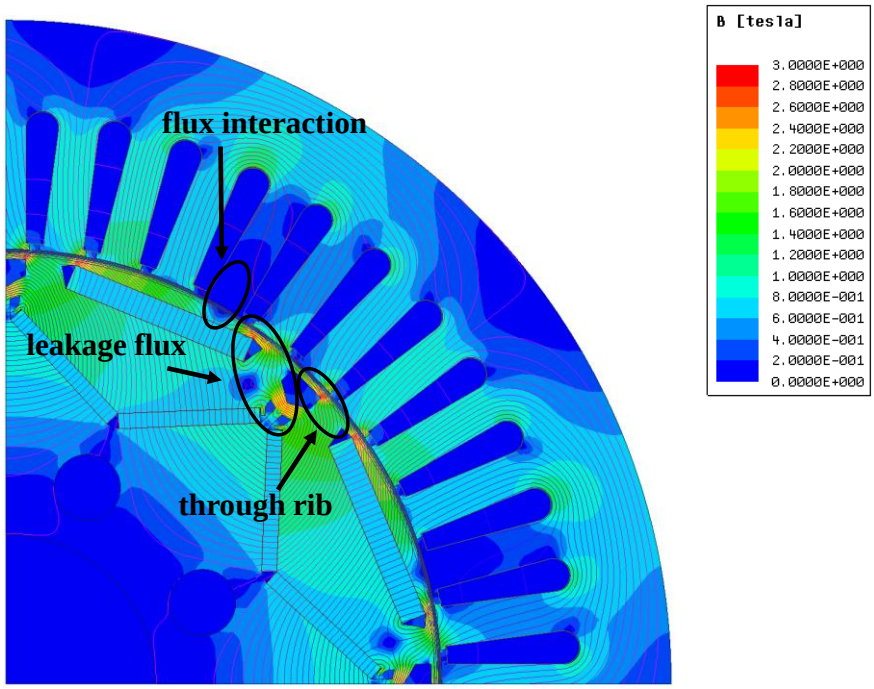

Fig. 6.11. IPM machine flux density at 10000 RPM.

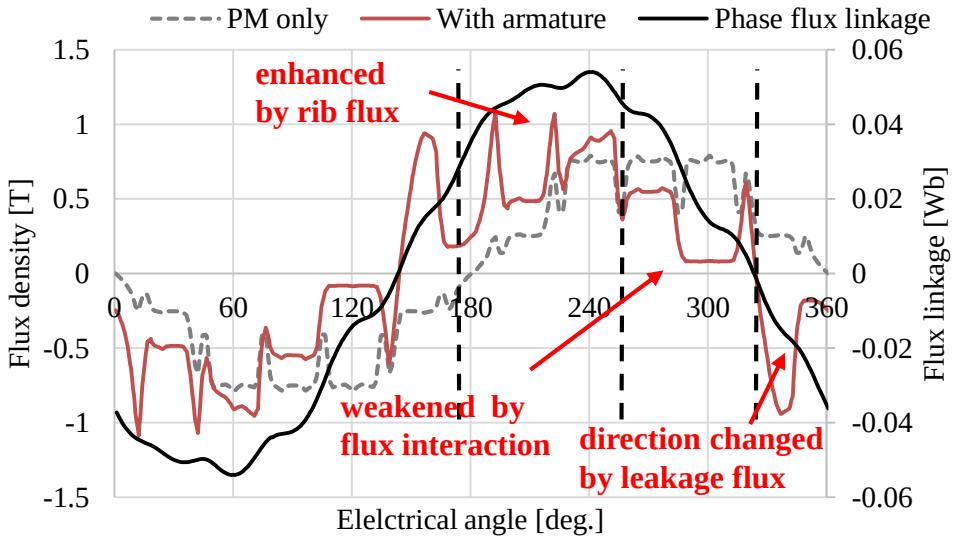

Fig. 6.12. Airgap flux density and phase flux linkage for IPM machine.

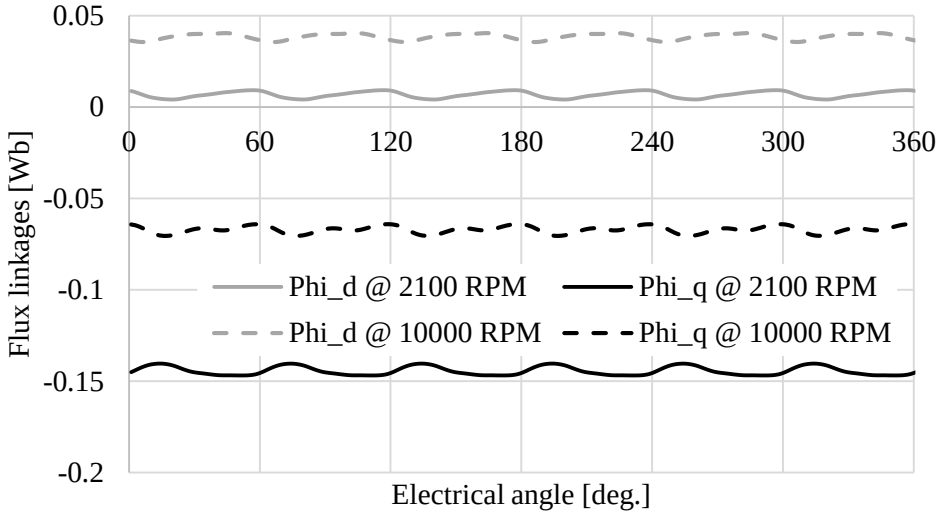

Fig. 6.13. IPM machine *dq* flux-linkage.

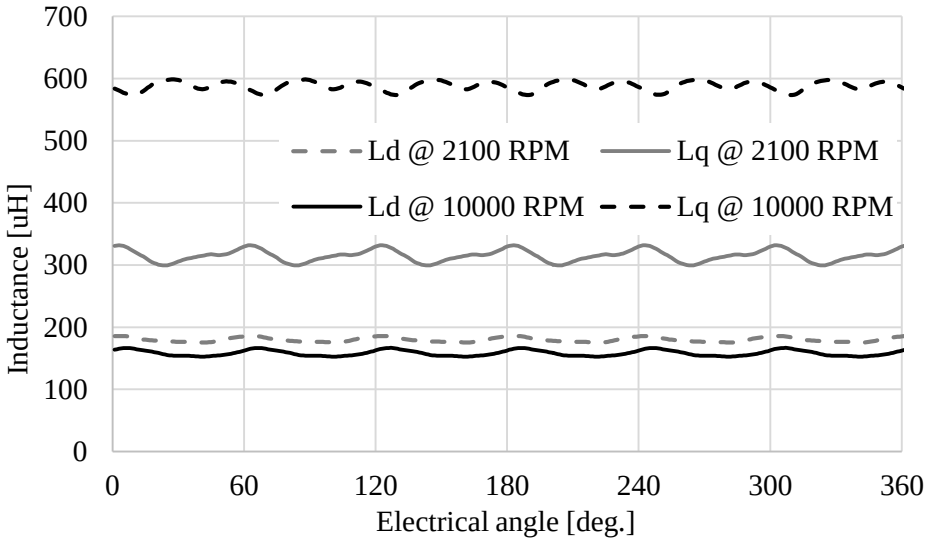

Fig. 6.14. IPM machine *dq* inductances.

According to the above comparison study, a few points of conclusion can be drawn as following:

(1) Brushless PM machines do not have to be salient to achieve a traction characteristics. Hence, the machine does not have to be designed with high saliency ratio.

(2) SPM machines can achieve the maximum torque with full utilization of the PM materials. With proper stator winding design, the example SPM machine has lower current rating than the benchmark IPM. In addition, the SPM machine achieves a more sinusoidal back-EMF waveform, hence so the torque ripple is lower than for the IPM machine.

(3) Both IPM and SPM machines have phase voltage distortion. The voltage distortion of SPM machines at low speed is slight, because the armature flux is unaligned with the PM flux. In deep field-weakening region, armature flux and PM flux are significantly conflicted, which leads to more severe voltage distortion. Since the PM material of IPM machine is embedded in the rotor lamination and flux confliction is less compared to the SPM machine, the phase voltage distortion is less severe for the SPM machine.

(4) For IPM machines, both the machine local magnetic saturation due to the rotor geometry and the armature reaction caused by the interaction of the PM flux and armature flux cause phase voltage distortion. The distortion effect increases with the rise of saliency ratio, which leads to a greater difference between the peak and fundamental voltage. In the high speed region, the machine peak voltage is higher than the DC-link voltage limit, which may introduce difficulty for vector control. To improve the IPM machine voltage distortion and torque ripple, the machine saliency ratio has to be reduced, although it will decrease the reluctance torque contribution.

6.4 Pole Shoe Machine

6.4.1 Design Concept

The comparison study of IPM and SPM machine shows that brushless PM machines do not have to be salient to achieve traction torque-speed characteristic and SPM machines could be candidates for traction machines. However, both of the two topologies suffer from high speed issues. Due to the armature reaction and local magnetic saturation of the IPM rotor, this machine has a high level of high speed torque ripple and the machine peak phase voltage is significantly higher than the DC-link voltage limit. For the SPM machine, although it improves the torque ripple and allows the peak phase voltage within the DC-link voltage limit, it has a high level of voltage distortion due to the armature reaction. In addition, and probably a more important feature for high volume automotive manufacture, SPM machines have to rely on a retaining sleeve to protect the surface magnets for high speed operation, which may induce additional manufacturing complexity.

In order to make full use of the respective advantages of the IPM and SPM machines, a pole shoe machine concept, is introduced in this section. As shown in Fig. 6.15, the magnets are embedded in the rotor pole shoes so that the magnets can be protected during high speed operation. The pole shoe machine has same stator and similar rotor structure with the SPM machine rotor, except the magnets are covered by an "iron case". Hence, this pole shoe topology is expected to have the advantages of SPM machine. In addition, the pole shoe arc can be adjusted to minimize cogging torque and to design a more sinusoidal open circuit back-EMF so that the machine excitation torque ripple can be improved. Comparing to the IPM machine, since the q-axis iron on the airgap side is removed, the machine is expected to have a lower salient ratio which improves the phase voltage distortion.

The pole shoe topology is common in industrial variable speed drives employing constant torque regimes, but not for traction. Here, the machine with a pole shoe rotor is designed to achieve traction performance. The pole shoe concept for vehicle traction is significantly different from existing practice in the electric and hybrid electric automotive industry and thus this departure in standard design is a contribution of this thesis.

6.4.2 Machine Design Procedure

It has been proved that the FEA model is accurate enough to analyze the machine performance in this case study. However, FEA requires high computational effort to solve the machine electro-magnetic field. On the other hand, the linear model provides much more efficient and faster computation though with its limitations due to the simplified nature of analysis. However, the linear model is sufficiently detailed to provide a first design iteration, hence, it is initially used to design the machine and suggest the best choice of machine target equivalent circuit parameters that enables the final design satisfy the machine specification. Then, the FEA model is applied to validate the machine design by checking the electro-magnetic and mechanical performance. The SPM machine design and validation procedure is illustrated in Fig. 6.16. This pole shoe machine is also designed with the same volumetric design constraints and equal active parts as the benchmark IPM machine.

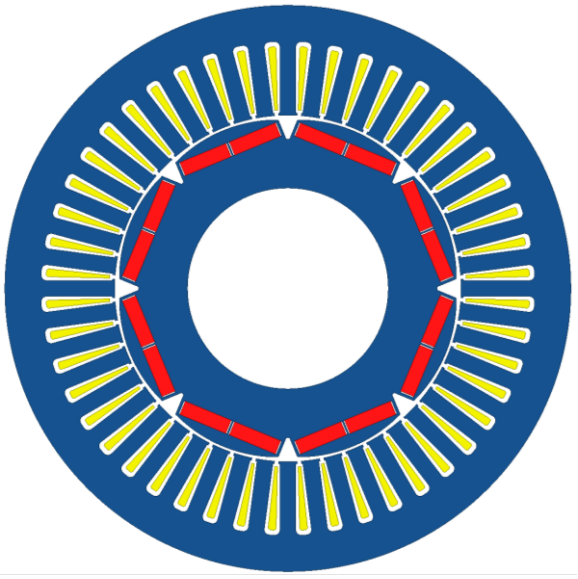

Fig. 6.15. Cross section of the example pole shoe machine.

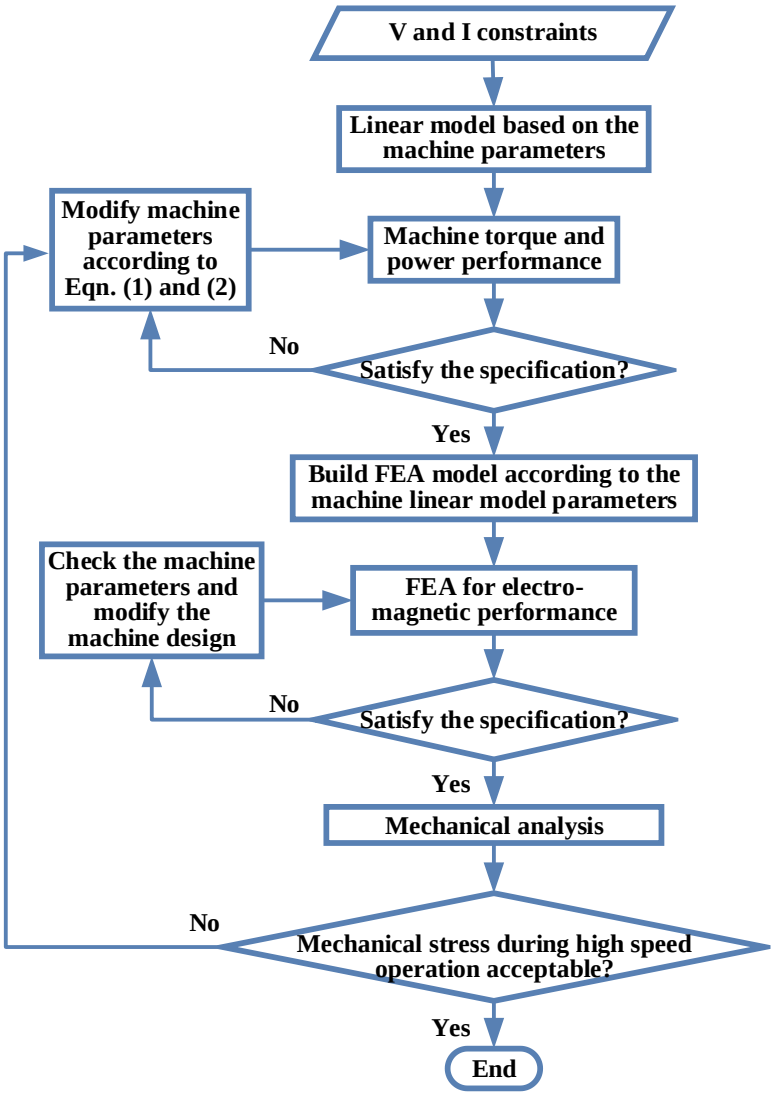

Fig. 6.16. Machine design procedure.

6.4.3 Concept Pole Shoe Machine Analysis

As discussed in the previous sections, the arc-shape PMs of the SPM machine are reshaped into rectangular blocks and then embedded into the rotor pole. The stator and magnet volume are maintained the same as the SPM machine. The pole shoe surface is adjusted so that the airgap length increases from the middle of the pole shoe to the pole edge, as illustrated in Fig.6.17. This is a classical design method to reduce cogging torque and voltage harmonics in moved field synchronous machines and is therefore used here to achieve the same goals. In order to keep the mechanical rigidity for high speed operation, the width of the upper bridge between the magnet pocket and rotor surface should be sufficient.

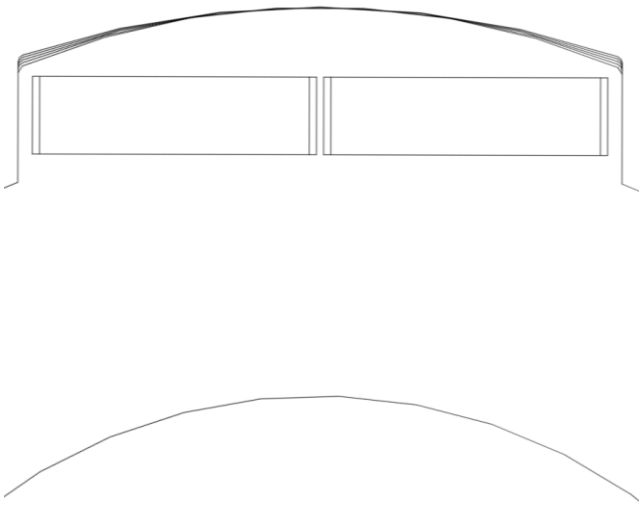

Fig. 6.17. Adjusting the pole shoe surface.

Therefore, the magnet pocket will have to be moved toward the machine shaft compared with the SPM machine. Thus, at low speed (2100 RPM as example), a peak phase current of 535 A is required to satisfy the maximum torque of 280 Nm. In addition, although the back-EMF is close to sinusoidal, the phase voltages at both 2100 RPM and 10000 RPM are distorted, severely so at 10000 RPM, as shown in Fig. 6.18. Hence a peak phase voltage of

350 V is required to reach the target torque of 76 Nm at 10000 RPM, which is significantly over the DC-link voltage limit. To explore the reason, the machine flux distribution is illustrated in Fig. 6.19. from which it can be noticed that the width of the bridge between the magnet and airgap is so large that it allows the flux to go through, and then across the airgap, which results in a reverse direction of the flux-linkage. In addition, due to the low permeance of the PM material, some armature fluxes are forced to circulate through the tooth-tips. Therefore, this machine has to be improved for better field-weakening capability, although it has been designed with sinusoidal back-EMF and a pole shoe shape beneficial for cogging torque reduction.

6.4.4 Improved Pole Shoe Machine Design

In order to shorten the bridge between the magnet and airgap, the large magnet pieces can be divided into smaller ones. As an example, the delta shape magnet, which has already been used by Nissan Leaf IPM, can be used to improve the pole shoe machine design, as shown in Fig. 6.20. For the delta shaped arrangement, the large magnet on the outer rim is smaller comparing to the magnet of I-shaped arrangement, which allows it to be positioned closer to the rotor surface than the one in the I-shaped magnet arrangement. In this way, the width of the bridge between the magnet and airgap can be smaller to improve the field distortion and it is beneficial for torque production, compared with the I-shaped magnet design. According to the flux vector distribution, illustrated in Fig. 6.21, the stator leakage flux stops going through the bridge and across the airgap, which significantly improves the phase voltage, as shown in fig. 6.22. With this design, the machine achieves a voltage distortion of 5.3 % at 2100 RPM (10.5 % for IPM machine), and 21 % at 10000 (30 % for IPM machine). The performance comparison of the benchmark IPM machine, example SPM machine and the proposed PS machine is illustrated in Table 6.3.

In Table 6.3, two points, i.e. 2100 and 10000 RPM are indicated as the key point performance indicators, because the machine maximum torque is at 2100 RPM and top speed is at 10000 RPM. These three machines are designed to have equitable active

dimension. The proposed pole shoe machine makes full use of the respective advantages of the IPM and SPM machines. The pole shoe machine achieves the target torque-speed performance of the benchmark IPM machine, with almost same efficiency. (The SPM machine has higher efficiency at low speed but lower efficiency at high speed). Similar to the SPM machine, the proposed pole shoe machine have a current rating reduction of 17% compared to the benchmark machine. In addition, the pole shoe machine decreases the peak voltage demand due to the reduction of voltage distortion. As previously discussed, IPM machine voltage distortion is directly related to the saliency ratio. Comparing to the benchmark IPM machine, the proposed pole shoe machine has a lower salient ratio, as shown in Fig. 6.23, which contributes not only higher PM utilization rate for maximum torque but also lower voltage distortion. Further, the pole shoe machine does not rely on the nonconductive sleeve to protect the PM for high speed operation. Comparing to SPM machines, the pole shoe rotor also keeps enough distance between the stator and PM to reduce flux linkage distortion caused by interaction of armature flux and PM flux.

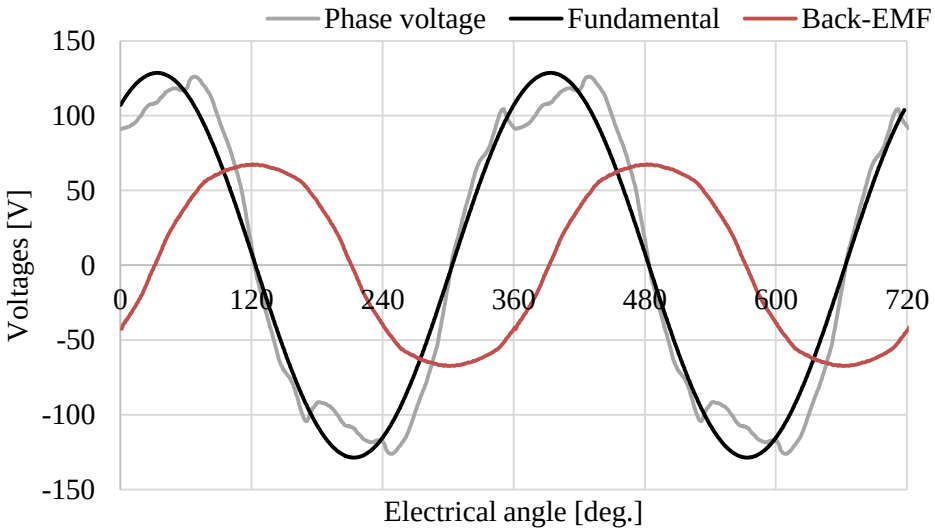

(a) 2100 RPM

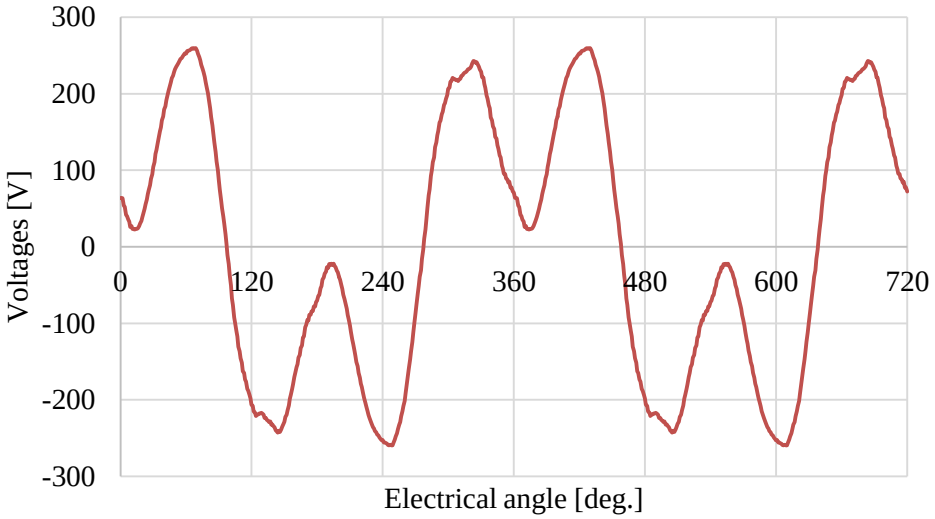

(b) 10000 RPM

Fig. 6.18. Example pole shoe machine phase voltage.

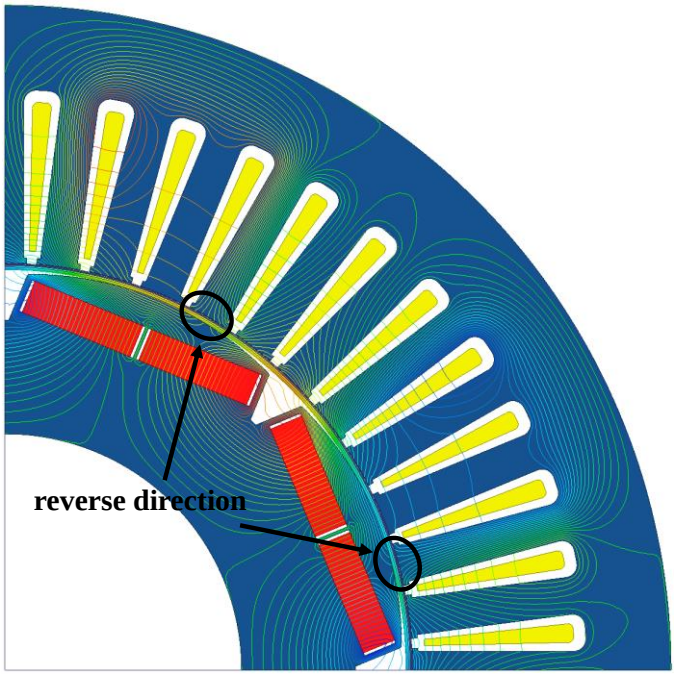

(a) Flux distribution

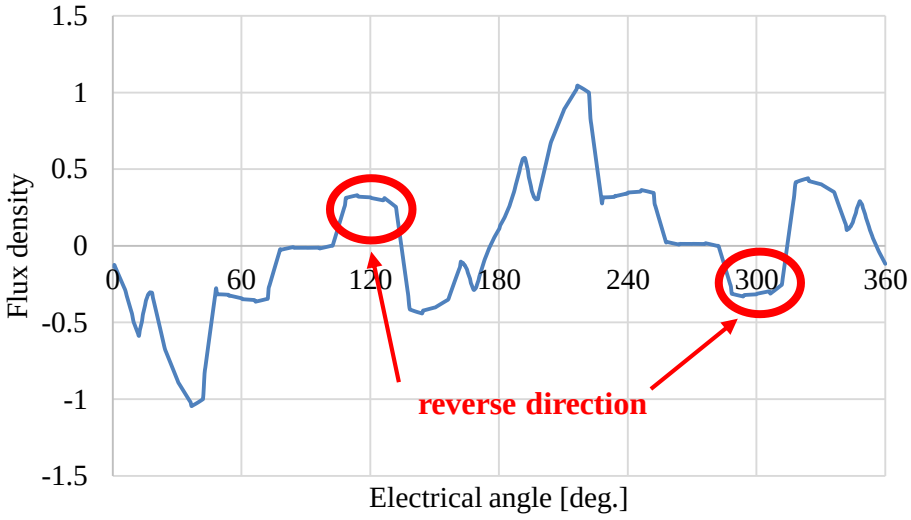

(b) Airgap flux density

Fig. 6.19. FEA results of the example pole shoe machine.

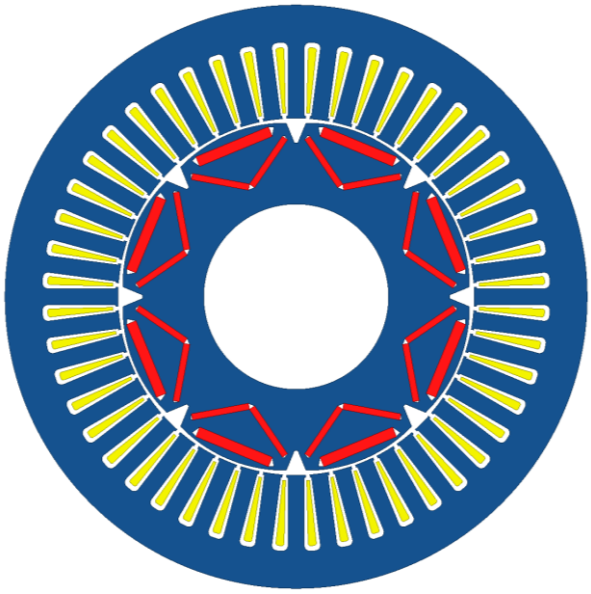

Fig. 6.20. Cross section of the proposed pole shoe machine.

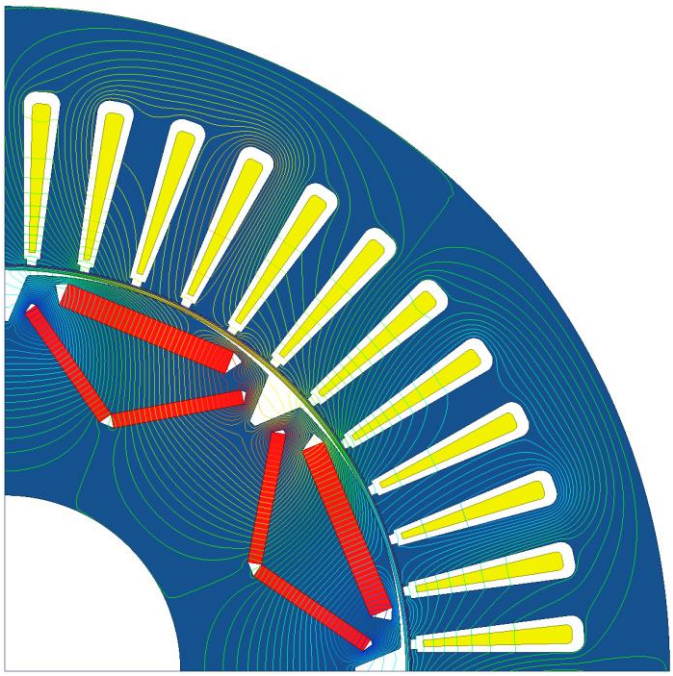

Fig. 6.21. Flux distribution of the proposed pole shoe machine.

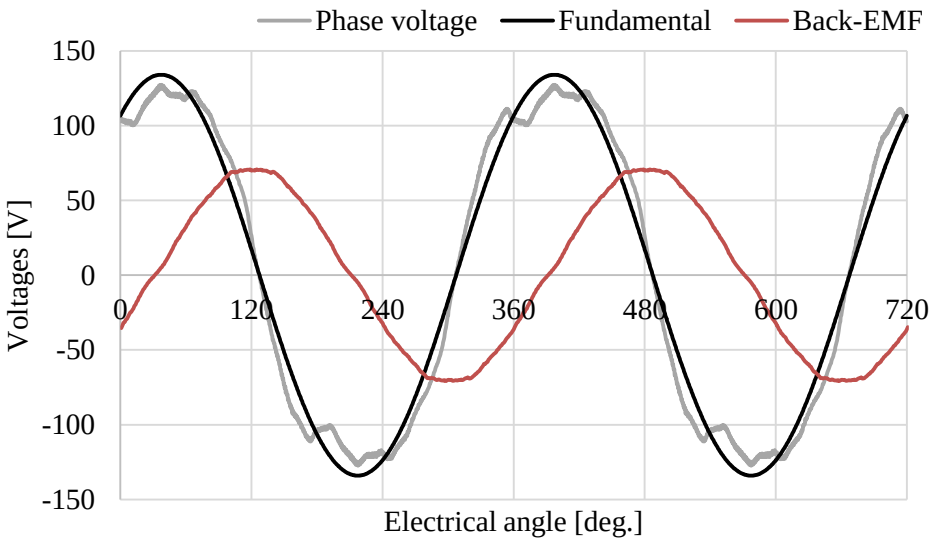

(a) 2100 RPM.

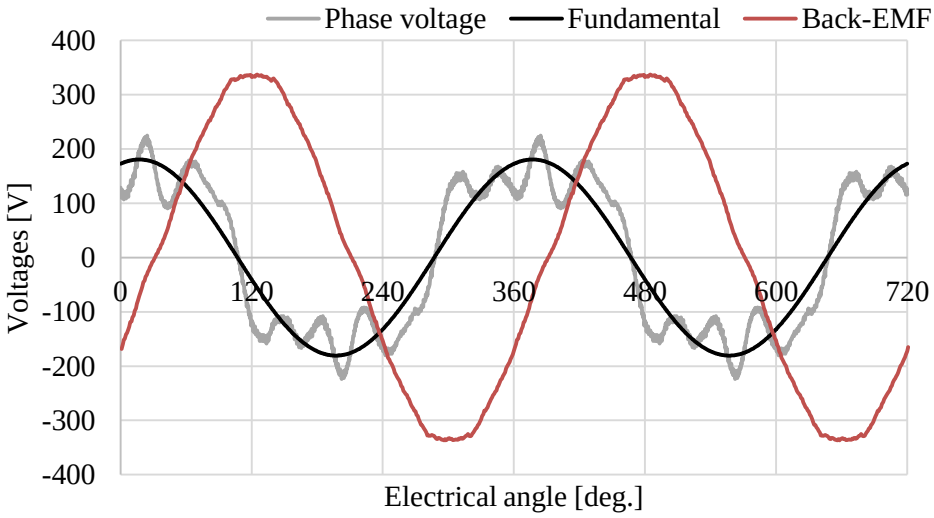

(b) 10000 RPM.

Fig. 6.22. Phase voltage and open circuit back-EMF of the proposed pole shoe machine.

Table 6.3. Comparison of Machine Key Operating Points.

	IPM machine		SPM machine		PS machine	
Speed (RPM)	2100	10000	2100	10000	2100	10000
Power (kW)	61.86	80.27	61.70	80.45	61.59	80.18
Torque (Nm)	281.3	76.65	280.59	76.82	280.08	76.56
Torque ripple (%)	9.30	23.87	5.51	15.85	4.13	26.29
Iphase_peak (A)	610	255	490	370	503	326
Angle (deg)	44	67.5	0	70	30	75
Vphase_peak (V)	92.63	271.81	133.51	218.93	127.27	211.14
V_distortion (%)	10.5	30	3.7	57	5.3	21
Iron loss (W)	171.29	1850.63	245.44	771.35	283.54	983.45
Copper loss (W)	4582.37	800.78	4251.54	2424.13	4480.12	1881.86
Mechanical loss (W)	17.15	388.89	17.15	388.89	17.15	388.89
Total loss	4770.81	3040.30	4514.13	3584.57	4780.81	3254.20
Efficiency (%)	92.84	96.35	93.19	95.74	92.80	96.10

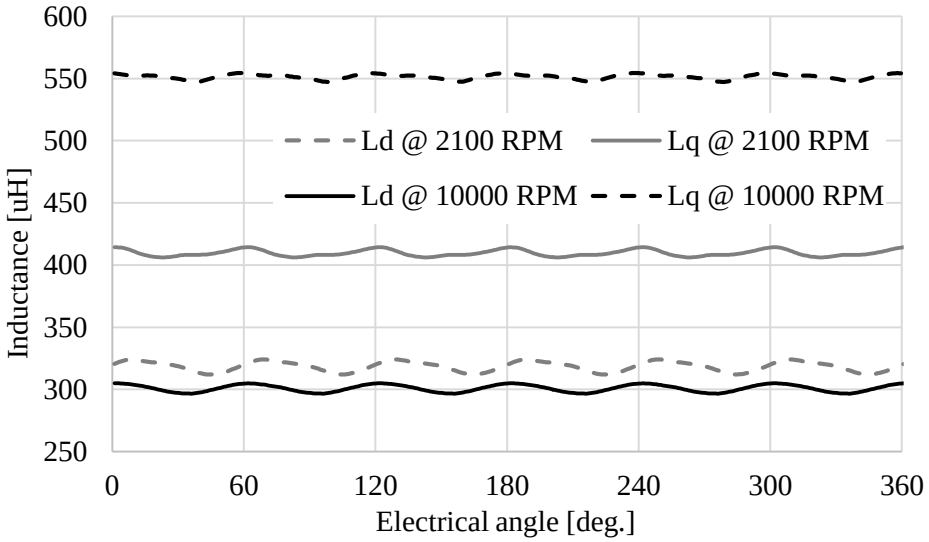

Fig. 6.23. *dq* inductance of the proposed pole shoe machine.

6.5 Conclusions

The study in this Chapter shows that IPM machines with high saliency ratio are not a necessary requirement to achieve traction torque-speed characteristics. Also, a higher saliency ratio will cause higher voltage distortion. The mechanisms of the on-load voltage distortion for both IPM and SPM machines are investigated. It reveals that the armature reaction caused by the interaction of armature and PM flux is the main reason for SPM machine phase voltage distortion. Therefore, higher value of excitation current angle leads to more severe voltage distortion. IPM machines have the same problem as SPM machines, but additionally the local magnetic saturation caused by the geometric feature of the IPM rotor is another contributor to voltage distortion. To make full use of the respective advantages of the IPM and SPM machine designs, a pole shoe machine design is proposed. The pole shoe machine achieves the target torque-speed performance of the benchmark IPM machine, with almost same efficiency but 17% peak current rating reduction compares with the IPM machine. In addition, the pole shoe machine satisfies the top speed performance, with the peak phase voltage within the DC-link voltage limit. The pole shoe machine has much lower saliency ratio, which results in a reduction of voltage distortion and hence decreases the peak voltage demand from the DC-link. Comparing with the SPM, the retaining sleeve can be eliminated, which facilitates easier high volume and hence manufacturing and cost.

Chapter 7

Conclusions, Future Research Work and Publications

7.1 Contributions

7.1.1 Feasibility of all-electric energy storage system design is explored for a port crane power-train.

Chapter 3 investigates the feasibility of energy storage systems for implementation in the hybrid energy source system (HESS) providing the power-train of an electrified port crane - RTGC. Based on the dynamic analysis of a typical RTGC, the energy requirement and power rating of the crane power-train system are specified. Compared with the traditional diesel ICE crane application, the electric crane, especially the battery-supercapacitor hybrid crane, shows great potential for regenerative energy recovery, which is associated to a reduction in fuel costs and emissions. For system analysis, a complete RTGC power-train Matlab/Simulink model is established. Both the battery and supercapacitor model are developed based on cell experimental dynamic assessments and validated by test data from the DESERVE project. A filter-based control strategy, which is simple to implement and numerically efficient, is proposed to allow the battery to operate as the main energy source with constant or low fluctuation of current and the supercapacitor to capture and release peak charge and discharge currents. The battery-supercapacitor hybrid energy storage systems are designed for both short and long period operation, which results in effective

energy conversion, and hence lower emissions, together with a compact construction solution. The procedures for design of battery alone and battery-supercapacitor hybrid energy source systems are shown to be different and independent of the optimization method chosen. These procedures are developed in this thesis. Further, the HESS systems are graphically optimized and proposed for RTGC applications. The improvement in system transient response afforded by the HESS thus results in a significant reduction in energy source mass and volume.

7.1.2 Key design parameters for induction machines to realize a traction characteristic are identified, and hence the machine design procedure is proposed.

Chapter 4 proposes a new modelling scheme for variable speed IMs that identifies the key design parameters influencing the traction torque-speed characteristic. At base speed the magnetizing reactance, X_m, is the dominant parameter that impacts on machine torque. However, in the field weakening region, the stator phase current vector angle, θ, becomes the main design parameter. The IM extended-speed operation can be achieved by reducing the magnetizing reactance, X_m, (by reducing the number of turns per phase). In this case, the low speed torque will be decreased due to the reduction of Ampere-turns. Then, the rotor resistance, R_r, and leakage inductance, L_{lr}, will be decreased (using wide, shallow and open mouth slots instead of narrow, deep and close mouth slots) to compensate the torque loss. Thus, the design concept for field-weakening is similar to that of PM machine design, where the back-EMF coefficient, k_o, is adjusted and the d-axis inductance–phase current product, $L_d I_s$, is increased to improve the extended field weakening region. Based on these points, an IM design procedure for traction applications is proposed. An FVFF DOL IM is studied as a benchmark machine which is subsequently redesigned using the proposed design procedure to illustrate the procedure and show improvements of machine performance in terms of efficiency, power factor and field weakening capability.

7.1.3 A commercialized battery EV traction system is assessed by considering DC-link voltage and temperature variations, and hence system redesign methods are proposed.

In Chapter 5, the thesis presents an assessment of electric vehicle power-train options based on a commercial benchmark vehicle system. Results from a vehicle power-train model, including the benchmark IPM traction machine, are presented to illustrate the power-train traction torque- and power-speed requirements. Since the vehicle DC-link is directly connected to the battery, the DC-link voltage varies with the battery terminal voltage during driving load cycles. When the benchmark IPM machine operates at the minimum DC-link voltage, the machine torque can only reach 40% of the required value during high speed operation at 10 kRPM. The vehicle power-train is then modified with the inclusion of a DC/DC converter between the vehicle battery and DC-link to maintain the traction system DC-link voltage near constant. A SC system is also considered for improved system voltage management. As an alternative machine topology, 5-turn and 7-turn IPM designs and an example SPM are assessed against the target performance requirements, and under the variable DC-link voltage conditions. In addition, temperature variation impacts on the traction machine, which results in variation of the back-EMF and current during high speed operation. Based on the voltage and temperature variation extremes, the DC/DC converter and machine power electronic converter requirements are assessed and presented. Finally, faulted operation of the electric machine/drive system is discussed. The most appropriate solution is the 8-turn IPM design with a DC/DC converter providing fault protection and stabilizing the DC-link to 375 V, thus allowing full performance from a lower current rated traction power electronic converter.

7.1.4 A brushless permanent magnet machine with pole shoe topology is proposed to achieve better field-weakening performance.

The study in Chapter 6 shows that IPM machines with high saliency ratio are not necessary to achieve traction torque-speed characteristics. The mechanisms of the on-load voltage

distortion for both IPM and SPM machines are investigated. It reveals that the armature reaction caused by the armature and PM flux are the main reason for SPM and IPM machine voltage distortion. Additionally, for IPM machines, local magnetic saturation caused by the geometric feature of IPM rotor is another reason. To makes full use of the respective advantages of the IPM and SPM machines, a pole shoe machine design is proposed. This machine achieves the maximum torque with the same peak phase current of the SPM machine, which is a 17% reduction compared to the benchmark IPM machine design. In addition, the pole shoe machine satisfies the top speed performance, with the peak phase voltage within the DC-link voltage limit. By adjusting the arc shape of the rotor pole shoe surface, a more sinusoidal back-EMF is achieved and results in the torque ripple reduction. Further, the voltage distortion of the pole shoe machine over the whole speed range is less than that of the benchmark IPM machine.

7.2 Future Work

(1) Chapter 3 only studies the port crane energy storage system, hence the whole power-train system, including hoist machine and machine drive, needs further study.

(2) The proposed induction machine design procedure in Chapter 4 is only implemented on a 2.2 kW induction machine, hence it needs to be implemented on a larger power rating machine to confirm validity

(3) Chapter 5 proposes power-train modifications to meet the target torque and power performance by considering voltage and temperature variation issues. The whole power-train efficiency, including the power converter efficiency, is not considered. A further design and investigation of the power converters will be studied.

(4) Chapter 6 only presents the pole shoe machine concept for traction application, hence a prototype machine needs to be built for validation.

7.3 Publications arising from this thesis

7.3.1 Journal publication

The following is a journal publication that resulted from this study:

[1] Nan Zhao, Nigel Schofield and Wangqiang Niu, "Energy storage system for a port crane hybrid power-Train," IEEE Transactions on Transportation Electrification, Vol. 2, No. 4, pp. 480-492, 2016.

[2] Nan Zhao, Rong Yang, Nigel Schofield and Ran Gu, "An investigation of DC-link voltage and temperature variations on EV traction system design," IEEE Transactions on Industry Applications, Vol. PP, No. 99, 2017.

7.3.2 Conference publications

The following is a list of conference publications that resulted from this study:

[1] Nan Zhao, Nigel Schofield, Wangqiang Niu, Piranavan Suntharalingam and Yaozhou Zhang, "Hybrid power-train for port crane energy recovery," 2014 IEEE Conference and Expo Transportation Electrification Asia-Pacific (ITEC Asia-Pacific), Beijing, China, Aug.31st - Sept. 3rd, pp. 1-6, 2014.

[2] Nan Zhao and Nigel Schofield, "An improved induction machine design procedure for electric vehicle traction," 8th IET International Conference on Power Electronics, Machines and Drives (PEMD 2016), Glasgow, Scotland, UK, April 19-21, pp. 1-6, 2016.

[3] Nan Zhao, Nigel Schofield, Rong Yang and Ran Gu, "An investigation of DC-link voltage and temperature variations on EV traction system design," 2016 IEEE Energy Conversion Congress and Exposition (ECCE), Milwaukee, MI, September 18-22, pp. 1-8, 2016.

[4] Nan Zhao and Nigel Schofield, "Field-weakening capability of interior permanent magnet machines with salient pole shoe rotors," 2017 IEEE International magnetics Conference (Intermag Europe 2017), Dublin, Ireland, April 24-28, 2017. (Accepted)

[5] Nan Zhao and Nigel Schofield, "Dual three-phase permanent magnet synchronous machine investigation for battery electric vehicle power-train," 2017 IEEE International magnetics Conference (Intermag Europe 2017), Dublin, Ireland, April 24-28, 2017. (Accepted)

Reference

[1] Government of Canada, Greenhouse Gas Emissions by Economic Sector. [Online]. Available: https://www.ec.gc.ca/indicateurs- indicators/default.asp?lang=en&n=F60DB708-1; last accessed: 4th, March, 2017.

[2] International Energy Agency, Rocky Mountain Institute, the Implementing Agreement for Cooperation on Hybrid and Electric Vehicle Technologies and Programs, the Electric Vehicles Initiative of the Clean Energy Ministerial and C40 Cities. (2012). EV City Case Book: A Look at the Global Electric Vehicle Movement. [Online]. Available: http://www.iea.org/publications/freepublications/publication/EVCityCasebook.pdf; last accessed: 4th, March, 2017.

[3] International Energy Agency and Electric Vehicles Initiative of Clean Energy Ministerial. (2015, Mar.). Global EV Outlook 2015. [Online]. Available: http://www.iea.org/evi/Global-EV-Outlook-2015-Update_1page.pdf; last accessed: 4th, March, 2017.

[4] A. Emadi, Y. J. Lee and K. Rajashekara. "Power electronics and motor drives in electric, hybrid electric, and plug-in hybrid electric vehicles," *IEEE Trans. Industrial Electronics*, vol. 55, no. 6, pp. 2237–2245, 2008.

[5] A. Emadi, *Advanced Electric Drive Vehicles*, Boca Raton, FL: CRC Press, Oct. 2014.

[6] International Energy Agency and Electric Vehicles Initiative of Clean Energy Ministerial. Global EV Outlook 2016. [Online]. Available: http://www.iea.org/publications/freepublications/publication/Global_EV_Outlook_2016.pdf; last accessed: 4th, March, 2017.

[7] C. C. Chan, A, Bouscayrol, and K. Chen, "Electric, hybrid, and fuel-cell vehicles: architectures and modeling," *IEEE Trans. Industrial Electronics*, vol. 59, no. 2, pp. 589–598, 2010.

[8] M. Ehsani, K. M. Rahman and H. A. Toliyat. "Propulsion system design of electric and hybrid vehicles," *IEEE Trans. Industrial Electronics*, vol. 44, no. 1, pp. 19–27, 1997.

[9] M. Ehsani, Y. Gao and S. Gay. "Characterization of electric motor drives for traction applications," in *Proc. 29th Annual Conference of IEEE Industrial Electronics Society*, Roanoke, Virginia, USA, pp. 891–895, 2003.

[10] N. Schofield, Lecture notes of course ECE 787, "Electric machines", department of Electrical and Computer Engineering, McMaster University, 2014.

[11] K. Yamamoto, K. Shinohara and T. Nagahama. "Characteristics of permanent-magnet synchronous motor driven by PWM inverter with voltage booster," *IEEE Trans. Industry Applications*, vol. 40, no. 4, pp. 1145–1152, 2004.

[12] N. Schofield and C. Giraud-Audine. "Design procedure for brushless PM traction machines for electric vehicle applications," in *Proc. 2005 IEEE International Electric Machines and Drives Conference*, San Antonio, TX, USA, pp. 1788–1792, 2005.

[13] G. Pellegrino, A. Vagati, P. Guglielmi and B. Boazzo. "Performance comparison between surface-mounted and interior PM motor drives for electric vehicle application," IEEE *Trans. Industrial Electronics*, vol. 59, no. 2, pp. 803–811, 2012.

[14] W. L. Soong and T. J. E. Miller. "Field-weakening performance of brushless synchronous AC motor drives," in *Proc. IEE Electric Power Applications*, vol. 141, no.6, pp. 331–340, 1994.

[15] K. T. Kim, K. S. Kim, S. M. Hwang, T. J. Kim and Y. H. Jung, "Comparison of performances between IPM and SPM motors with rotor eccentricity," IEEE *Trans. Magnetics*, vol. 37, no. 5, pp. 3448–3451, 2001.

[16] J. Dong, Y. Huang, L. Jin and H. Lin. "Comparative Study of Surface-Mounted and Interior Permanent-Magnet Motors for High-Speed Applications," IEEE *Trans. Applied Superconductivity*, vol. 26, no. 4, 5200304, 2016.

[17] R. Schiferl, T. A. Lipo, "Power capability of salient pole permanent magnet synchronous motors in variable speed drive applications," *IEEE Trans. Industry Applications*, vol. 26, no. 1, pp. 115–123, 1990.

[18] M. Ehsani, Y. Gao and J. M. Miller. "Hybrid electric vehicles: architecture and motor drives," in *Proc. IEEE*, vol. 95, no. 4, pp. 719–728, (2007).

[19] X. Luo and T. A. Lipo. "A synchronous/permanent magnet hybrid AC machine," *IEEE Trans. Energy Conversion*, vol. 15, no. 2, pp. 203–210, 2000.

[20] Y. Amara, L. Vido, M. Gabsi, E. Hoang, A. H. Ben Ahmed and M. Lecrivain. "Hybrid excitation synchronous machines: energy-efficient solution for vehicles propulsion," IEEE *Trans. Vehicular Technology*, vol. 58, no. 5, pp. 2137–2149, 2009.

[21] C. C. Chan. "The state of the art of electric, hybrid, and fuel cell vehicles," in *Proc. IEEE*, vol. 95, no. 4, pp. 704–718, 2007.

[22] National Bureau of Statistics of China, "Volume of freight handled in main coastal ports above designated size," in *China Statistical Yearbook-2014*. Beijing: China Statistics Press, 2014.

[23] Z. Li, G. Wang, K. Shen, T. Zhao and X. Ni, "Research of the crane system based on technology of storing-energy with super-capacitor," in *Proc. IEEE Conf. 2010 International Conference on Electrical and Control Engineering*, Wuhan, China, pp. 4046–4049, 2010.

[24] C. Chang, J. Yang, P. Cao, Q. Niu and Z. Zhu, "Study on supercapacitor energy saving system for rubber-tyred gantry crane," in *Proc. IEEE Conf. 2010 Asia-Pacific Power and Energy Engineering Conference*, Chengdu, China, pp. 1–6, 2010.

[25] Ministry of Communications of PRC. (2003, Aug.). Evaluation of design comprehensive unit energy consumption in port capital construction (technical innovation) projects. Beijing. [Online]. Available: http://wenku.baidu.com/view/78f82ded0975f46527d3e16a.html (In Chinese); last accessed 4th, March, 2015.

[26] S. M. Kim and S.K. Sul, "Control of rubber tyred gantry crane with energy storage based on supercapacitor bank," *IEEE Trans. Power Electron*, vol. 21, no. 5, pp. 1420–1427, 2006.

[27] D. Bayasgalan, J. S. Ryu, S. H. Lee, D. H. Han, Y. J. Lee, H. R. Choi and G. H. Choe, "Improved RTGC system with voltage compensation converter to reduce fuel consumption," in *Proc. IEEE Conf. 2012 IEEE Energy Conversion Congress and Exposition*, Raleigh, NC, USA, pp. 34–40, 2012.

[28] X. Zhou, M. Dong and D. Zhou, "Study on hybrid power system of wheeled crane," in *Proc. IEEE Conf. 3rd International Conference on Biomedical Engineering and Informatics*, Yantai, China, pp. 2667–2672, 2010.

[29] K. Obata, T. Sakamoto, N. Yoshioka, N. Fujisawa, H. Yoshikawa and T. Monzen, "Grid-Powered Electric Transfer Crane," *Mitsubishi Heavy Industries Technical Review*, vol. 47, no. 2, pp. 15–18, 2010.

[30] A. Vujicic, N. Zrnic and B. Jerman, "Ports sustainability: A life cycle assessment of zero emission cargo handling equipment," *Strojniski Vestnik - Journal of Mechanical Engineering*, vol. 59, no. 9, pp. 547–555, 2013.

[31] Ministry of Transport of the PRC. (2012, Aug.). Promotional materials of the fifth energy conservation demonstration projects (Part 15): rubber-tyred gantry cranes lithium battery-powered energy-saving projects. [Online]. Available: http://jtjnw.mot.gov.cn/shifangdx/201208/t20120827_1291448.html (In Chinese); last accessed on 4th, March, 2015.

[32] M. M. Flynn, P. McMullen and O. Solis, "High-speed flywheel and motor drive operation for energy recovery in a mobile gantry crane," in *Proc. IEEE Conf. APEC 07 - Twenty-Second Annual IEEE Applied Power Electronics Conference and Exposition*, Anaheim, California, USA, pp. 1151–1157, 2007.

[33] E. Ovrum and T. F. Bergh, "Modell lithium-ion battery hybrid ship crane operation," *Appl. Energy*, 152, pp. 162–172, 2015.

[34] International Energy Agency. (2015, Mar.). Global EV Outlook 2015. Presented at Electric Vehicles Initiative of the Clean Energy Ministerial. [Online]. Available: http://www.iea.org/evi/Global-EV-Outlook-2015-Update_1page.pdf; last accessed on 4th, March, 2015.

[35] J. Cao and A. Emadi, "A new battery/ultracapacitor hybrid energy storage system for electric, hybrid, and plug-in hybrid electric vehicles," *IEEE Trans. Power Electronics*, vol. 27, no. 1, pp. 122–132, 2012.

[36] J. Dixon, I. Nakashima, E. F. Arcos and M. Ortuzar, "Electric vehicle using a combination of ultracapacitors and ZEBRA battery," *IEEE Trans. Industrial Electronics*, vol. 57, no. 3, pp. 943–949, 2010.

[37] R. A. Dougal, S. Liu and R. E. White, "Power and life extension of battery-ultracapacitor hybrids," *IEEE Trans. Components and Packaging Technologies*, vol. 25, no. 1, pp. 120–131, 2002.

[38] R. Sadoun, N. Rizoug, P. Bartholomeus, B. Barbedette and P. Le Moigne, "Influence of the drive cycles on the sizing of hybrid storage system battery-supercapacitor supplying an electric vehicle," in *Proc. IEEE Conf. IECON 2011 - 37th Annual Conference of the IEEE Industrial Electronics Society*, Melbourne, Australia ,pp. 4106–4112, 2011.

[39] R. Sadoun, N. Rizoug, P. Bartholomeus, B. Barbedette and P. Le Moigne, "Optimal sizing of hybrid supply for electric vehicle using Li-ion battery and supercapacitor," in *Proc. 2011 IEEE Vehicle Power and Propulsion Conference*, Chicago, IL, USA, 2011, pp. 1–8.

[40] R. de Castro, C. Pinto, R. Esteves Araujo, P. Melo and D. Freitas, "Optimal sizing and energy management of hybrid storage system," *in Proc. 2011 IEEE Vehicle Power and Propulsion Conference*, Chicago, IL, USA, pp. 321–326, 2012.

[41] J. Shen, A. Hasanzadeh and A. Khaligh, "Optimal power split and sizing of hybrid energy storage system for electric vehicles," in *Proc. Conf. 2014 IEEE Transportation Electrification Conference and Expo*, Dearborn, MI, USA, pp. 1–6, 2014.

[42] J. Shen, S. Dusmez and A. Khaligh, "Optimization of sizing and battery cycle life in battery/ultracapacitor hybrid energy storage systems for Electric Vehicle Applications," *IEEE Trans. Industry Informatics*, vol. 10, no. 4, pp. 2112–2121, 2014.

[43] C. Pinto, J. V. Barreras, R. de Castro, E. Schaltz, S. J. Andreasen and R. Esteves Araujo, "Influence of Li-Ion Battery Models in the Sizing of Hybrid Storage

Systems with Supercapacitors," in *Proc. 2014 IEEE Vehicle Power and Propulsion Conference*, Coimbra, Portugal, pp. 1–6, 2014.

[44] L. Wang, E. G. Collins, Jr. and H. Li, "Optimal design and real-time control for energy management in electric vehicles," *IEEE Trans. Vehicular Technology*, vol. 60, no. 4, pp. 1419–1429, 2011.

[45] A. Ostadi and M. Kazerani, "A comparative analysis of optimal sizing of battery-only, ultracapacitor-only, and battery–ultracapacitor hybrid energy storage systems for a city bus," *IEEE Trans. Vehicular Technology*, vol. 64, no. 10, pp. 4449–4460, 2015.

[46] UK Technology Strategy Board (TSB), Low Carbon Vehicles Innovation Platform: "Develop high Energy battery and high power Supercaps for all Electric Range Van Evaluation (DESERVE)", Project number TP/9/LCV/6/I/S0037C, 2008-11.

[47] N. Bianchi and S. Bolognani, "Design procedure of a vector controlled induction motor for flux-weakening operations," in *Proc. 32nd IEEE Industry Applications Conf. IAS Annu. Meeting*, Portland, OR, USA, pp. 104–111, 1997.

[48] L. Alberti, N. Bianchi and S. Bolognani, "Variable-speed induction machine performance computed using finite-element," *IEEE Trans. Industry Applications*, vol. 47, no. 2, pp. 789–797, 2005.

[49] X. Lu, K. Iyer, K. Mukherjee and N. Kar, "Study of permanent magnet machine based flywheel energy storage system for peaking power series hybrid vehicle control strategy," in *Proc. 2013 IEEE Transportation Electrification Conference and Expo*, Metro Detroit, MI, USA, pp. 1–7, 2013.

[50] P. H. Mellor, N. Schofield, A. J. Brown, and D. Howe, "Assessment of supercapacitor/flywheel and battery EV traction systems," in *Proc. 33rd ISATA*, Dublin, Ireland, 2000, pp. 235–242.

[51] J. Sudworth, "The sodium/nickel chloride (ZEBRA) battery," *Journal of Power Sources*, vol. 100, pp. 149–163, 2001.

[52] A. M. Jarushi, "Analysis and modelling of energy source combinations for electric vehicles," Ph.D. thesis, school of Elect. and Electron. Eng., Univ. of Manchester, Manchester, 2010.

[53] KOHLER power system, 700 kW Diesel Generators/700REOZDE, [Online]. Available: http://www.kohlerpower.com/onlinecatalog/pdf/g5385.pdf; last accessed on 4th, Match, 2017.

[54] C. Chang, R. Wang, Z. Zhu and H. Xu, "Research of supercapacitor voltage equalization strategy on rubber-tyred gantry crane energy saving system," in *Proc. IEEE 2009 Asia-Pacific Power and Energy Engineering Conference*, Wuhan, China, pp. 1–4, 2009.

[55] Maxwell Technologies, "NEW" 48 Volt Modules - With New, DuraBlue™ Technology Documents, [Online]. Available: http://www.maxwell.com/images/documents/48V_ds_DuraBlue_3000685_2.pdf; last accessed on 4th, March, 2015.

[56] L. Spyker, R. M. Nelms, "Classical Equivalent Circuit Parameters for a double layer capacitor," *IEEE Trans. aerospace and electronic systems*, vol. 36, no. 3, pp. 829–836, 2000.

[57] J. J. Awerbuch and C. R. Sullivan, "Filter-based power splitting in ultracapacitor-battery hybrids for vehicular applications," in *Proc. 2010 IEEE 12th Workshop on Control and Modeling for Power Electronics*, Boulder, CO, USA, pp. 1–8, 2010.

[58] Liebherr Rubber Tyre Gantry Crane (RTG) technical description (May. 2010), [Online]. Available: https://www.liebherr.com/shared/media/maritime-cranes/downloads-and-brochures/brochures/lcc/liebherr-rtg-cranes-technical-description.pdf; last accessed on 4th, March, 2017.

[59] T. Wang, P. Zheng, Q. zhang and S. Cheng, "Design characteristics of the induction motor used for hybrid electric vehicle," *IEEE Trans. Magnetics*, vol. 41, no. 1, pp. 505 - 508, 2005.

[60] P. M. Matthew and T. K. Philip, "Examination of design strategies for inverter-driven induction machines," in *Proc. IEEE Conf. 2012 IEEE Power and Energy Conference at Illinois*, pp. 1 - 6, 2012.

[61] N, Zhao, N. Schofield, and W. Niu, P. Suntharalingam, and Y. Zhang, "Hybrid power-train for port crane energy recovery," in *Proc. IEEE Transportation Electrification Conf. Expo. Asia-Pacific*, Beijing, China, pp. 1–6, 2014.

[62] D. G. Kokalj, "Variable frequency drives for commercial laundry machines," *IEEE Industry Applications Magazine*, vol. 3, n. 3, pp. 27-30, 1997.

[63] O. I. Avram and P. Xirouchakis, "Evaluating the use phase energy requirements of a machine tool system", *Journal of Cleaner Production*, vol. 19, no. 6-7, pp. 699-711, 2011.

[64] M. Olszewski, "Evaluation of the 2010 Toyota Prius hybrid synergy drive system," Oak Ridge Nat. Lab., Oak Ridge, ORNL/TM-2010/253, Mar. 2011.

[65] D. Zorbas, "Electric Machines: principles, applications, and control schematics," Stamford, CT, USA: Cengage Learning, 2nd edn. 2014.

[66] M. Ehsani, Y. Gao, and S. Gay, "Characterization of electric motor drives for traction applications," in *Proc. IEEE Industrial Electronics Society the 29th Annual Conf.*, Roanoke, USA, pp. 891-895, 2003.

[67] M. Ehsani, K. M. Rahman, and H. A. Toliyat, "Propulsion system design of electric and hybrid vehicles," *IEEE Trans. Industrial Electronics*, vol. 44, no. 1, pp. 19-27, 1997.

[68] N. Zhao, R. Yang, N. Schofield, and R. Gu, "An investigation of DC-link voltage and temperature variations on EV traction system design," in *Proc. IEEE Energy Conversion Congress and Exposition*, Milwaukee, WI, USA,pp. 1-8, 2016

[69] N. Schofield, S. A. Long, D. Howe, M. McClelland, "Design of a Switched Reluctance Machine for Extended Speed Operation," *IEEE Trans. Industry Applications*, vol. 45, no. 1, pp. 116 – 122, 2009.

[70] E. B. Agamloh, A. Cavagnino, "High efficiency design of induction machines for industrial applications," in *Proc. IEEE Workshop on Electrical Machines Design Control and Diagnosis*, Paris, France, pp. 33-46, 2013.

[71] Q. Hecker, J. A. B. Ccoa, W. Meyer, H. G. Herzog, "Automated design of squirrel-cage induction machines by predefined torque-speed-characteristic," in *Proc. Int. IEEE Conf. Electric Machines and Drives*, pp. 1160-1165, 2013.

[72] J. H. Lee, S. S. Ramamurthy, and T. W. Yun, "Optimum design for premium 250 kW efficiency of traction induction motor using response surface methodology & FEM," Incheon, South Korea, in *Proc. IEEE Int. Conf. Electrical Machines and Systems*, pp. 1844-1847, 2010.

[73] E. Hall, B. D. Lee, and J. C. Balda, "Optimum speed ratio of induction motor drives for electrical vehicle propulsion," in *Proc. IEEE Applied Power Electronics Conf.*, Anaheim, USA,pp. 371-377, 2001.

[74] S. Williamson, C. I. McClay, "Optimization of the geometry of closed rotor slots for cage induction motors," *IEEE Trans. Industry Applications*, vol. 32, no. 3, pp. 560-568, 1996.

[75] M. Amrhein and P. T. Krein, "Rotor designs for small inverter-dedicated induction machines," in *Proc. IEEE Int. Conf. Electric Machines and Drives*, Madison, USA, pp. 1279-1285, 2003.

[76] Z. Zhang, F. Profumo, A. Tenconi, "Improved design for electric vehicle induction motors using an optimization procedure," in *Proc. IEE Electric Power Applications*, vol. 143, no. 6, pp. 410-416, 1996.

[77] Z. M. Zhao, S. Meng, C. C. Chan, and E. W. C. Lo, "A novel induction machine design suitable for inverter-driven variable speed systems," *IEEE Trans. Energy Conversion*, vol. 15,no. 4, pp. 413-420, 2000.

[78] T. Wang, P. Zheng, Q. Zhang, S. Cheng, "Design characteristics of the induction motor used for hybrid electric vehicle," *IEEE Trans. on Magnetics*, vol. 41, no. 1, pp. 505-508, 2005.

[79] W. L. Soong and T. J. E. Miller, "Field-weakening performance of brushless synchronous AC motor drives", in *Proc. IEE Electric Power Applications*, vol. 141, no. 6, pp. 331-340, 1994.

[80] P. Lindh, J. Montonen, M. G. Tehrani, and J. Pyrhönen, "Design process of a traction motor for a hybrid bus application," in *Proc. IEEE Electric Power Quality and Supply Reliability Conf.*, Rakvere, Estonia, pp. 255-258, 1994.

[81] Y. Gao and M. Ehsani, "Parametric design of the traction motor and energy storage for series hybrid off-road and military vehicles," *IEEE Trans. Power Electronics*, vol. 21, no. 3, pp. 749-755, 2006.

[82] J. L. Oldenkamp and S. C. Peak, "Selection and design of an inverter-driven induction motor for a traction drive system," *IEEE Trans. Industry Applications*, vol. IA-21, no. 1, pp. 259-265, 1985.

[83] M. P. Magill and P. T. Krein, "Examination of design strategies for inverter-driven induction machines," in *Proc. Power and Energy Conf.*, Illinois, Champaign, USA, pp. 1-6, 2012.

[84] F. G. G. de Buck, "Design adaptation of inverter-supplied induction motors," *IEE Journal Electric Power Applications*, vol. 1, no. 2, pp. 54-60, 1978.

[85] S. Cui, Y. Bai, and L. Song, "Rotor slots design of induction machine for hybrid electric vehicle drives," in *Proc. IEEE Conf. Vehicle Power and Propulsion*, Windsor, United Kingdom, pp. 1-3, 2006.

[86] S. S. Murthy, B. Singh, and G. Bhuvaneswari, K. Naidu and U. Siva, "Design of squirrel cage induction motors for traction applications," in *Proc. IEEE Conf. Power Electronics, Drives and Energy Systems*, New Delhi, India, pp. 1-7, 2006.

[87] A. Harson, P. H. Mellor, and D. Howe, "Design considerations for induction machines for electric vehicle drives," in *Proc. IET Conf. Electrical Machines and Drives*, Durham, United Kingdom, pp. 16-20, 1995.

[88] H. Liu, Y. Zhang, Q. Zheng, D. Wang, and S. Guo "Design and simulation of an inverter-fed induction motor for electric vehicles," in *Proc. IEEE Conf. Vehicle Power and Propulsion*, Arlington, USA, pp. 112–115, 2007.

[89] S. Duan and L. Zhou, "Influence of parameters on field weakening performance of induction motor," in *Proc. Conf. Int. Electrical machines and systems*, Beijing, China, pp. 1–5, 2011.

[90] N. Bianchi and S. Bolognani, "Design procedure of a vector controlled induction motor for flux-weakening operations," in *Proc. Industry Applications Conf. Thirty-Second IAS Annual Meeting*, New Orleans, USA, pp. 104–111, 1997.

[91] L. Alberti, N. Bianchi, and S. Bolognani, "Variable-speed induction machine performance computed using finite-element," *IEEE Trans. Industry Applications*, vol. 47, no. 2, pp. 789-797, 2005.

[92] J. Puranen, "Induction motor versus permanent magnet synchronous motor in motion control applications: a comparative study," PhD thesis, Lappeenranta University of Technology, 2006.

[93] P. Vas, "Vector Control of AC Machines", Oxford, U.K.: Clarendon Press, 1990.

[94] P. Krause, O. Wasynczuk, S. Sudhoff, and S. Pekarek, "Analysis of Electric Machinery and Drive Systems, Piscataway," NJ, USA: Wiley-IEEE Press, 2nd edn. 2013.

[95] O. Wasynczuk, S. D. Sudhoff, K. A. Corzine, J. L. Tichenor, P. C. Krause, I. G. Hansen, and L. M. Taylor, "A maximum torque per ampere control strategy for induction motor drives," *IEEE Trans. Energy Conversion*, vol. 13, no. 2, pp. 163-169, 1988.

[96] J. Soltani, M. Hajian, G. Arab, "Maximum torque per ampere control of induction motor drive without mechanical sensor," in *IEEE Proc. Int. Conf. Control, Automation and Systems*, Seoul, South Korea, pp. 2685–2690, 2008.

[97] R. Yang, N. Schofield, and A. Emadi, "Comparative study between interior and surface permanent magnet traction machine designs," in *Proc. IEEE Transportation Electrification Conf. Expo.*, Dearborn, MI, USA, pp. 1-6, 2016.

[98] G. A. Putrus, P. Suwanapingkarl, D. Johnston, E.C. Bentley, and M. Narayana, "Impact of electric vehicles on power distribution networks," in *Proc. 2009 IEEE Vehicle Power and Propulsion Conference*, Dearborn, MI, USA, pp. 827–831, 2009.

[99] B. G. Pollet, I. Staffell and J. Shang, "Current status of hybrid, battery and fuel cell electric vehicles: From electrochemistry to market prospects," *Electrochim. Acta*, vol. 84, pp. 235-249, 2012.

[100] K. Yamamoto, K. Shinohara and T. Nagahama, "Characteristics of permanent-magnet synchronous motor driven by PWM inverter with voltage booster," *IEEE Trans. Industry Applications*, vol. 40, no. 4, pp. 1145–1152, 2004.

[101] K. T. Kim, K. S. Kim, S. M. Hwang, T. J. Kim and Y. H. Jung, "Comparison of performances between IPM and SPM motors with rotor eccentricity," *IEEE Trans. Magnetics*, vol. 37, no. 5, pp. 3448-3451, 2002.

[102] D. G. Dorrell, A. M. Knight, L. Evans and M. Popescu, "Analysis and design techniques applied to hybrid vehicle drive machines—assessment of alternative IPM and induction motor topologies," *IEEE Trans. Industrial Electronics*, vol. 59, no. 10, pp. 3690-3699, 2012.

[103] B. Ozpineci, "Oak Ridge National Laboratory annual progress report for the power electronics and electric machinery program," Oak Ridge Nat. Lab., Oak Ridge, TN, ORNL/SPR-2014/532, Nov. 2014.

[104] R. Yang, N. Schofield and A. Emadi, "Comparative study between interior and surface permanent magnet traction machine designs," in *Proc. IEEE Transportation Electrification Conference and Expo*, Dearborn, MI, USA, 2016.

[105] J. Shen, S. Dusmez and A. Khaligh, "Optimization of sizing and battery cycle life in battery/ultracapacitor hybrid energy storage systems for electric vehicle applications," *IEEE Trans. Industry Informatics*, vol. 10, no. 4, pp. 2112–2121, 2014.

[106] 2011 Nissan LEAF - Traction Motor System (TMS), [Online]. Available: https://carmanuals2.com/get/nissan-leaf-2011-traction-motor-system-tms-47803; last accessed: 4th, March, 2017.

[107] Y. Sato, S. Ishikawa, T. Okubo, M. Abe, and K. Tamai, "Development of high response motor and inverter system for the Nissan LEAF electric vehicle," presented at the SAE World Congr. Exhibit., Tech. Paper 2011-01-0350, 2011.

[108] N. Zhao, N. Schofield and W. Niu, "Energy storage system for a port crane hybrid power-train," *IEEE Trans. transportation electrification*, vol. 2, no. 4, pp. 480–492, 2016.

[109] J. H. Lee, C. Y. Won, B. K. Lee, and H. B. Kim, "IPMSM torque control method considering DC-link voltage variation and friction torque for EV/HEV applications," in *Proc. 2012 IEEE Vehicle Power and Propulsion Conference*, Seoul, South Korea, pp. 1063–1069, 2012.

[110] J. H. Lee, J. H Lee, J. H. Park, and C. Y Won, "Field-weakening strategy in condition of DC-link voltage variation using on electric vehicle of IPMSM," in *Proc. IEEE 2011 International Conference on Electrical Machines and Systems*, Beijing, China, pp. 1–6, 2011.

[111] Toyota Hybrid System THS II, [Online]. Available: http://www.evworld.com/library/toyotahs2.pdf; last accessed: 4th, March, 2017.

[112] M. Kamiya, "Development of traction drive motors for the Toyota hybrid system," *IEEJ Trans. Industry Applications*, vol. 126, no. 4, pp. 473–479, 2006.

[113] T. Schoenen, M. S. Kunter, M. D. Hennen, and R. W. De Doncker, "Advantages of a variable DC-link voltage by using a DC-DC converter in hybrid-electric vehicles," in *Proc. 2010 IEEE Vehicle Power and Propulsion Conference*, Lille, France, pp. 1–5, 2010.

[114] K. Yamamoto, K. Shinohara and T. Nagahama, "Characteristics of permanent-magnet synchronous motor driven by PWM inverter with voltage booster," *IEEE Trans. Industry Applications*, vol. 40, no. 4, pp. 1145–1152, 2004.

[115] A. Najmabadi, K. Humphries, and B. Boulet, "Implementation of a bidirectional DC-DC in electric powertrains for drive cycles used by medium duty delivery trucks," in Proc. IEEE Conf. ECCE., pp. 1338–1345, 2015.

[116] J. Lemmens, J. Driesen and P. Vanassche, "Dynamic DC-link voltage adaptation for thermal management of traction drives," in *Proc. 2015 IEEE Energy Conversion Congress and Exposition*, Montreal, QC, Canada, pp. 180–187, 2013.

[117] C. Yu, J. Tamura and R. D. Lorenz, "Control method for calculating optimum DC bus voltage to improve drive system efficiency in variable DC bus drive systems," in *Proc. 2012 IEEE Energy Conversion Congress and Exposition*, Raleigh, NC, USA, pp. 2992–2999, 2012.

[118] J. O. Estima and A. J. M. Cardoso, "Efficiency analysis of drive train topologies applied to electric/hybrid vehicles," *IEEE Trans. Vehicular Technology*, vol. 61, no. 3, pp. 1021–1031, 2012.

[119] S. Tenner, S. Gimther and W. Hofmann "Loss minimization of electric drive systems using a DC/DC converter and an optimized battery voltage in automotive applications," in *Proc. 2011 IEEE Vehicle Power and Propulsion Conference*, Chicago, IL, USA, pp. 1–7, 2011.

[120] S. Dusmez, A. Khaligh, "A Compact and Integrated Multifunctional Power Electronic Interface for Plug-in Electric Vehicles," *IEEE Trans. Power Electronics*, vol.28, no.12, pp.5690–5701, 2013.

[121] X. Zhang, X. Wen, Q. Guo and F. Zhao, "A new control scheme for DC-DC converter feeding constant power load in electric vehicle," in *Proc. IEEE Electrical Machines and Systems 2011 International Conference*, Beijing, China, pp. 1–4, 2011.

[122] F. Zhao, X. Zhang, X. Wen, L. Zhao, Q. Guo and G. Zhang, "A novel control scheme for bi-directional Buck Boost converter", in *Proc. IEEE Electrical Machines and Systems 2013 International Conference*, Busan, South Korea, pp. 1431–1436, 2013.

[123] X. Jia, C. Hu; S. Du, M. Chen; P.Lin and D. Xu, "DC-link voltage control strategy of a bi-directional DC/DC converter for electric vehicles," in *Proc. 2015 IEEE Energy Conversion Congress and Exposition*, Montreal, QC, Canada, pp. 92–99, 2015.

[124] T. Lahlou, D. Wittmann, M. Abdelrahem and H. Herzog, "Stabilization of the DC-link voltage in a two stage cascaded H-Bridge multilevel converter for battery

energy storage systems," in *Proc. IEEE International Energy Conference,* Leuven, Belgium, pp. 1–6, 2016.

[125] H. Shi, K. Wang, X. Xiao and K. Sun, "Capacitor voltage balancing of a three-level bi-directional buck-boost converter for battery energy storage system," in *Proc. IEEE 17th International Conference on Electrical Machines and Systems*, Hangzhou, China, pp. 325–329, 2014.

[126] S. B. Monge, J. Bordonau, D. Boroyevich, and S. Somavilla, "The nearest three virtual space vector PWM—A modulation for the comprehensive neutral point balancing in the three-level NPC inverter," *IEEE Power Electron. Lett.*, vol. 2, no. 1, pp. 11–15, 2004.

[127] H. Zhang, S. J. Finney, A. Massoud, and B. W. Williams, "An SVM algorithm to balance the capacitor voltages of the three-level NPC active power filter," *IEEE Trans. Power Electron.*, vol. 23, no. 6, pp. 2694–2702, 2008.

[128] A. Choudhury, P. Pillay, S. S. Williamson, "DC-link voltage balancing for a 3-level electric vehicle traction inverter using an innovative switching sequence control scheme", *IEEE J. Emerg. Sel. Topics Power Electron.*, vol. 2, no. 2, pp. 296–307, 2014.

[129] A. Choudhury, P. Pillay, S. S. Williamson, "Comparative analysis between two-level and three-level DC/AC electric vehicle traction inverters using a novel DC-link voltage balancing algorithm", IEEE J. Emerg. Sel. Topics Power Electron., vol. 2, no. 3, pp. 529–540, 2014.

[130] A. Choudhury, P. Pillay, S. S. Williamson, "A hybrid PWM-based DC-link voltage balancing algorithm for a three-level NPC DC/AC traction inverter drive", *IEEE J. Emerg. Sel. Topics Power Electron.*, vol. 3, no. 3, pp. 806–816, 2015.

[131] A. M. Jarushi and N. Schofield, "Battery and supercapacitor combination for a series hybrid electric vehicle," in *Proc. 5th IET International Conference on Power Electronics, Machines and Drives*, Brighton, United Kingdom, pp. 1-6, 2010.

[132] R. Carter, A. Cruden, and P. J. Hall, "Optimizing for efficiency or battery life in a battery/supercapacitor electric vehicle," *IEEE Trans. Vehicular Technology*, vol. 61, no. 4, pp. 1526–1533, 2012.

[133] B. Hredzak, V. G. Agelidis, and M. S. Jang, "A model predictive control for a hybrid battery–ultracapacitor power source," *IEEE Trans. Power Electronics*, vol. 29, no. 3, pp. 1469–1479, 2014.

[134] M. Choi, J. Lee and S. Seo, "Real-time optimization for power management systems of a battery/supercapacitor hybrid energy storage system in electric vehicles," *IEEE Trans. on Vehicular Technology*, vol. 63, no. 8, pp. 3600–3611, 2014.

[135] H. Samani and X. Fernando, "Battery current's fluctuations removal in hybrid energy storage system based on optimized control of supercapacitor voltage," *IEEE Embedded Systems Lett.*, vol. 8, no. 3, pp. 53–56, 2016.

[136] S. Dusmez and A. Khaligh, "A supervisory power-splitting approach for a new ultracapacitor–battery vehicle deploying two propulsion machines," *IEEE Trans. on Industrial Informatics*, vol. 10, no. 3, pp. 1960–1971, 2014.

[137] J. Shen and A. Khaligh, "Design and real-time controller implementation for a battery-ultracapacitor hybrid energy storage system," *IEEE Trans. on Industrial Informatics*, vol. 12, no. 5, pp. 1910–1918, 2016.

[138] N28AH Sintered Neodymium-Iron-Boron Magnets, Arnold Megnetic Technology, accessed on Jan. 2017. [Online]. Available: http://www.arnoldmagnetics.com/Portals/0/Files/Catalogs%20and%20Lit/Neo/151021/N28AH%20-%20151021.pdf?ver=2015-12-07-103803-743; last accessed: 4th, March, 2017.

[139] 2016 LEAF OWNER'S MANUAL, [Online]. Available: https://owners.nissanusa.com/content/techpub/ManualsAndGuides/LEAF/2016/2016-LEAF-owner-manual.pdf; last accessed: 4th, March, 2017.

[140] J. G. Hayes and K. Davis, "Simplified electric vehicle powertrain model for range and energy consumption based on EPA coast-down parameters and test validation by argonne national lab data on the nissan leaf," in *Proc. 2014 IEEE Transportation Electrification Conference and Expo*, Dearborn, MI, USA, pp. 1–6, 2014.

[141] U.S. Department of Energy, "2011 Nissan Leaf – VIN 0356 Advanced Vehicle Testing – Baseline Testing Results," [Online]. Available: http://energy.gov/sites/prod/files/2014/02/f8/2011_nissan_leaf_fs.pdf; last accessed: 4th, March, 2017.

[142] T. Burress, "Benchmarking State-of-the-Art Technologies", presentation at the 2013 U.S. Department of Energy Hydrogen and Fuel Cells Program and Vehicle Technologies Program Annual Merit Review and Peer Evaluation Meeting, 2013.

[143] T. Burress, "Benchmarking competitive technologies", presentation at the 2012 U.S. Department of Energy Hydrogen and Fuel Cells Program and Vehicle Technologies Program Annual Merit Review and Peer Evaluation Meeting, 2012.

[144] H. Lowse-Busch, M. Duoba, E. Rask, M. Meyer, "Advanced Powertrain Research Facility AVTA Nissan Leaf Testing and Analysis," Argonne National Laboratory, October, 2012.

[145] N. Schofield, "Fundamentals of power-train design for all- and hybrid-electric road vehicles", *IEEE Transportation Electrification Conference and Expo*, 2014, Tutorial, June 2014, pp. 1 - 198, DOI: 10.1109/ITEC.2014.6861819.

[146] R. Gu, *Physics-Based Modeling of Direct Coupled Hybrid Energy Storage Modules in Electrified Vehicles*, Ph.D. thesis, McMaster University, Hamilton, ON, Canada 2016.

[147] Maxwell Technologies. 'NEW' 48 Volt Modules—With New, DuraBlue Technology Documents, accessed on Nov. 2015. [Online]. Available: http://www.maxwell.com/images/documents/48V_ds_DuraBlue_3000685_2.pdf

[148] T. Burress, "Benchmarking of Competitive Technologies 2012 Nissan LEAF," EETT Presentation, USCAR, 2012.

[149] R. Schiferl, T. A. Lipo, "Power capability of salient pole permanent magnet synchronous motors in variable speed drive applications," *IEEE Trans. Industry Applications*, vol. 26, no. 1, pp. 115–123, 1990.

[150] T. Friedli, J. W. Kolar, "Comparative evaluation of three-phase AC–AC matrix converter and voltage DC-link back-to-back converter systems," *IEEE Trans. Industrial Electronics*, vol. 59, no. 12, pp. 4487–4510, 2012.

[151] M. Olszewski, "Evaluation of the 2010 Toyota Prius hybrid synergy drive system," Oak Ridge Nat. Lab., Oak Ridge, ORNL/TM-2010/253, Mar. 2011.

[152] Y. Yang, S. Castano, R. Yang, M. Kasprzak, B. Bilgin, A. Sathyan, H. Dadkhah, and A. Emadi, "Design and comparison of interior permanent magnet motor topologies for traction applications," *IEEE Trans. Transportation Electrification*, vol. PP, no. 99, 2016.

[153] J. de Santiago, H. Bernhoff, B. Ekergård, S. Eriksson, S. Ferhatovic, R. Waters, and M. Leijon, "Electrical motor drivelines in commercial all-electric vehicles: a review," *IEEE Trans. Vehicular Technology*, vol. 61, no. 2, pp. 475–484, 2012.

[154] B. Ozpineci, "Oak Ridge National Laboratory annual progress report for the power electronics and electric machinery program," Oak Ridge Nat. Lab., Oak Ridge, TN, ORNL/SPR-2014/532, Nov. 2014.

[155] M. Cirani, S. Eriksson, and J. Thunberg, "Innovative design for flux leakage reduction in IPM machines," *IEEE Trans. Industry Applications*, vol. 50, no. 3, pp. 1847–1853, 2014.

[156] D. G. Dorrell, M. Hsieh, M. Popescu, L. Evans, D. A. Staton, and V. Grout, "A review of the design issues and techniques for radial-flux brushless surface and internal rare-earth permanent-magnet motors," *IEEE Trans. Industrial Electronics*, vol. 58, no. 9, pp. 3741–3757, 2011.

[157] M. N. Uddin, T. S. Radwan, and M. A. Rahman, "Performance of interior permanent magnet motor drive over wide speed range," *IEEE Trans. Energy Conversion*, vol. 7, no. 1, pp. 79–84, 2002.

[158] Z. Q. Zhu and D. Howe, "Electrical machines and drives for electric, hybrid, and fuel cell vehicles," *Proceedings of the IEEE*, vol. 95, no. 4, pp. 746–765, 2007.

[159] W. L. Soong and T. J. E. Miller, "Field-weakening performance of brushless synchronous AC motor drives", in *Proc. IEE Electric Power Applications*, vol. 141, pp. 331–340,1994.

[160] A. M. EL-Refaie, M. R. Shah, R. Qu, and J. M. Kern "Effect of number of phases on losses in conducting sleeves of high speed surface PM machine rotors," IEEE *Trans. Industry Applications*, vol. 44, no. 5, pp. 1522–1529, 2008.

[161] L. Wu, R. Qu, and D. Li, "Reduction of rotor eddy-current losses for surface PM machines with fractional slot concentrated windings and retaining sleeve," *IEEE Trans. Magnetics*, vol. 50, no. 11, 8205704, 2014.

[162] R. Yang, N. Schofield, and A. Emadi, "Comparative study between interior and surface permanent magnet traction machine designs," in *Proc. IEEE Transportation Electrification Conference and Expo*, Dearborn, MI, USA, 2016.

[163] A. M. EL-Refaie and T. M. Jahns, "Optimal flux weakening in surface PM machines using fractional-slot concentrated windings," *IEEE Trans. Industry Applications*, vol. 41, no. 3, pp. 790–800, 2005.

[164] J. Wang, X. Yuan, and K. Atallah, "Design optimization of a surface-mounted permanent-magnet motor with concentrated windings for electric vehicle applications," *IEEE Trans. Vehicular Technology*, vol. 62, no. 3, pp. 1053–1064, 2013.

[165] G. Pellegrino, A. Vagati, P. Guglielmi and B. Boazzo. "Performance comparison between surface-mounted and interior PM motor drives for electric vehicle application", *IEEE Trans. Industrial Electronics*, vol. 59, no. 2, pp. 803–811, 2011.

[166] P. B. Reddy, A. M. El-Refaie, K. Huh, J. K. Tangudu, and T. M. Jahns, "Comparison of interior and surface PM machines equipped with fractional-slot concentrated windings for hybrid traction applications," *IEEE Trans. Energy Conversion*, vol. 27, no. 3, pp. 593–602, 2012.

[167] J. Dong, Y. Huang, L. Jin and H. Lin, "Comparative study of surface-mounted and interior permanent-magnet motors for high-speed applications," *IEEE Trans. Applied Superconductivity*, vol. 26, no. 4, 5200304, 2016.

[168] N. Zhao and W. Liu, "Loss calculation and thermal analysis of surface-mounted PM motor and interior PM motor," *IEEE Trans. Magnetics*, vol. 51, no. 11, 8112604, 2015.

[169] W. Chlebosz and G. Ombach, "Demagnetization properties of IPM and SPM motors used in the high demanding automotive application", *The international journal for computation and mathematics in electrical and electronic engineering*, vol. 32, no. 1 pp. 72 – 85, 2012.

[170] M. Chowdhury, A. Gebregergis, M. Islam, and T. Sebastian, "Analysis of harmonic contents in induced voltage and electromagnetic torque in interior permanent magnet synchronous machines under loaded condition," in *Proc. IEEE 2013 International Electric Machines & Drives Conference*, Chicago, IL, USA, pp. 260–267, 2013.

[171] Z. Q. Zhu and D. Wu, "On-load voltage distortion in fractional-slot interior permanent magnet machines," *IEEE Trans. Magnetics*, vol. 51, no. 10, 8107809, 2015.

[172] Z. Q. Zhu, D. Wu, M. C. Wu and I. W. Lan, "Influence of on-load voltage distortion on torque-speed characteristic of interior permanent magnet machines," in *Proc. 2015 IEEE Energy Conversion Congress and Exposition*, Montreal, QC, Canada, pp. 760–767, 2015.

[173] D. Wu and Z. Q. Zhu, "On-Load Voltage Distortion in Fractional Slot Surface-Mounted Permanent Magnet Machines Considering Local Magnetic Saturation," *IEEE Trans. Magnetics*, vol. 51, no. 8, 8106410, 2015.

[174] T. Burress, "Benchmarking of Competitive Technologies," Oak Ridge National Laboratory, 2012, [Online]. Available: http://www1.eere.energy.gov/vehicle sandfuels/pdfs/merit_review_2012/adv_power_electronics/ape006_burress_2012_p.pdf; last accessed 4th March, 2017.

[175] R. Yang, *Electrified vehicle traction machine design with manufacturing considerations*, Ph.D. thesis, McMaster University, Hamilton, ON, Canada 2016.